Development of Piezoresistive Tactile Sensors and a Graphical Display System for Minimally Invasive Surgery and Robotics

Masoud Kalantari

A Thesis
In the Department of
Mechanical and Industrial Engineering

Presented in Partial Fulfillment of the Requirements
For the Degree of
Doctor of Philosophy(Mechanical and Industrial Engineering) at
Concordia University
Montreal, Quebec
October 2012

Concordia University
School of Graduate Studies

This is to certify that the thesis prepared

By: Masoud Kalantari

Entitled: Development of Piezoresistive Tactile Sensors and a Graphical Display System for Minimally Invasive Surgery and Robotics

and submitted in partial fulfillment of the requirements for the degree of

Doctor of Philosophy

complies with the regulations of the University and meets the accepted standards with respect to originality and quality.

Signed by the final Examining Committee:

Dr. Ahmed A. Kishk Chair

Dr. William L. Cleghorn External Examiner

Dr. Ramin Sedaghati Internal Examiner

Dr. Wen-Fang Xie, Internal Examiner

Dr. Amir G. Aghdam Internal Examiner

Dr. Javad Dargahi Co-Supervisor

Dr. József Kövecses Co-Supervisor

Approved by:

Dr. Martin D. Pugh Chair of Department

Dr. Robin Drew Dean of Faculty

October 2012

Abstract

Development of Piezoresistive Tactile Sensors and a Graphical Display System for Minimally Invasive Surgery and Robotics

Masoud Kalantari, PhD
Concordia University, 2013

This PhD work presents a new tactile and feedback systems for minimally invasive surgery (MIS)and robotics. The thesis is divided into two major sections: the tactile sensing system, and the graphical display system.

In the tactile sensing system, piezoresistive materials are used as measuring elements. The first part of the thesis is focused on the theoretical modeling of piezoresistive sensing elements, which are semiconductive polymer composites. The model predicts the piezoresistive behavior in semiconductive polymer composites, including their creep effect and contact resistance. A single force sensing resistor (FSR) is, then, developed by using the semiconductive polymer composite materials. The developed FSR is used in the structure of a novel tactile sensor as the transduction element. The developed tactile sensor is designed to measure the difference in the hardness degree of soft tissues. This capability of the sensor helps surgeons to distinguish different types of tissues involved in the surgery. The tactile sensor is integrated on the extremity of a surgical tool to provide tactile feedback from the interaction between surgical instruments and the tissue during MIS. Mitral valve annuloplasty repair by MIS is of our particular interest to be considered as a potential target for the use of the developed tactile sensor. In the next step, the contact interaction of the tactile sensor with soft tissues is modelled, parametrically. Viscoelastic interaction is considered between the tactile sensor and atrial tissue in annuloplasty mitral valve repair; and a parametric solution for the viscoelastic contact is achieved.

In addition to the developed sensor, a novel idea regarding measuring the indentation rate, in addition to measuring force and displacement is implemented in a new design of an array tactile sensor. It is shown that the indentation-rate measurement is

an important factor in distinguishing the hardness degree of tissues with viscoelastic behaviour.

The second part of the thesis is focused on the development of a three-dimensional graphical display that provides visual palpation display to any surgeon performing robotic assisted MIS. Two matrices of the developed piezoresistive force sensor are used to palpate the tissue and collect the tactile information. The collected data are processed with a new algorithm and graphically rendered in three dimensions. Consequently, the surgeon can determine the presence, location, and the size of any hidden superficial tumor/artery by grasping the target tissue in a quasi-dynamic way.

Acknowledgements

I would like to take the opportunity and greatly and deeply thank my advisors, Professor Javad Dargahi from Concordia University and Professor József Kövecses from McGill University, for their nonstop supports, suggestions, and direction. I will always count on them to provide direction and support whenever I feel lost or stressed. I would like to thank them from the bottom of my heart for all their contributions, guidance, remarkable/practical ideas, and encouragement. Moreover, I would like to thank Professor Angeles at the Department of Mechanical Engineering, McGill University, and Dr. Renzo Cecere at the Division of Cardiothoracic Surgery, McGill University, for his thoughtful and useful advice. I would also like to thank the members of my defence committee, Professor Muthukumaran Packirisamy, Professor Ramin Sedaghati, and Professor Amir G. Aghdam, who have helped me throughout my PhD program.

Very special thanks go to all my friends and lab-mates in the Tactile Sensing and Medical Robotics Laboratory at Concordia University and Centre for Intelligent Machines at McGill University: Roozbeh Ahmadi, Jing Jin Shen, Toufic Azar, Mohammad Reza Ramezanifard, Ahmad Atieh, Siamak Arbatani, Mahmood Ghanbari, Shahrzad Nouri, and Ali Fellah Jahromi. Definitely, I could not have had better friends and colleagues.

I also want to thank the administrative staff at Concordia University: Leslie Hossien, Arlene Zimmerman, Sophie Mrineau, and Maureen Thuringer.

My deepest heartfelt gratitude goes out to my wife, Farnoush Farnia. She supported and encouraged me from the very beginning step of my PhD study until I finish it; I am really grateful for having her in my life. I would also like to express my profound gratitude to my father Ebrahim, my mother Mahin, my sisters, and brother. Words simply can not express my love for my family. They have been with me every step of the way and I could not have achieved it without them.

The last, but not least, I would like to thank Concordia University and its staff for preparing such an environment and opportunity for me to carry on my studies to the doctoral level.

To Farnoush Farnia,
Ebrahim Kalantari, and Mahin Rezaie.

Table of Contents

List of Tables

List of Figures

Chapter 1

Introduction

The invasive form of surgery is being gradually replaced by laparoscopic surgery—also referred to as Minimally Invasive Surgery (MIS)—which is rapidly becoming the more preferred method of surgery for almost any possible surgical operations. MIS is a special surgical procedure that employs non-invasive techniques. During this form of surgery, small incisions are made in which plastic tubes, or ports are inserted. Slender incising instruments and a miniature camera, that provides images of organs inside the body, are then inserted through these tubes to conduct surgery.

Since the past three decades, MIS has offered several advantages for both surgeons and patients [1, 2]. Benefits of MIS procedures include: less post operative discomfort, quicker recovery time, shorter hospital stay, earlier return to full activities, much smaller scars, and less internal trauma. However, despite the progress of MIS techniques during these three decades, there are still various unsolved inadequacies involved with such techniques. In fact, one of these unsolved problems is the

lack of providing tactile feedback to surgeons [3]. As an example, surgeons who use the da Vinci surgical system, developed by Intuitive Surgical Inc., do not feel tactile information while surgical tools interact with the internal organs of patients [4]. As another example, during Catheter-based Techniques (CBT), cardiac surgeons also do not feel such tactile information while catheters interact with blood vessel walls or cardiac tissues. Due to this inadequacy, numerous surgical operations cannot still be performed with available MIS techniques or CBT. The focus of the current PhD thesis is to provide surgeons with artificial tactile sensing and feedback during MIS or CBT. In the literature, force and pressure sensors are the objects of a majority of research projects in tactile applications [5]. However, some tactile sensors that can sense hardness or detect lumps have also been introduced by researchers [6]. In the first part of this work, two tactile sensors are designed and developed. They can measure the relative hardness degree of soft tissues by using piezoresistive sensing principle.

Semiconductive polymer composites are used in the structure of the tactile sensors as piezoresistive sensing elements. The electrical resistivity of piezoresistive elements changes as the result of the application of force to their structure. To the best of author's knowledge, the available models in the literature are not accurate enough to show the piezoresistive behaviour of semiconductive polymer composites inside the structure of a force/pressure sensor. Therefore, in this thesis the piezoresistive

behaviour of these sensing elements are fully tested, analyzed, and modelled parametrically. By using the piezoresistive sensing elements in the structure of the tactile sensor, the behaviour of the sensor is predicted for any type of force applied to its structure. Section 1.0.1 discusses the latest literature on the modeling of polymer composites and their shortcomings. Further, the advantages of the developed model over other available models are discussed and elaborated.

As stated, a novel tactile sensor is developed, which includes two piezoresistive force sensors as sensing elements. The modelled semiconductive materials are used in the structure of the tactile sensor. The developed piezoresistive tactile sensor has significant advantages over currently available sensors, which makes it unique for both MIS and CBT. The state of the art tactile sensors are discussed in Section 1.0.2. In addition, the drawbacks and inadequacies of the available sensors are stated.

The tactile sensor is placed on the extremity of a surgical tool to provide tactile feedback from the interaction between surgical instruments and the tissue during surgery. The interaction feedback allows surgeons to gain information similar to what they gain with their finger during the touch.

The developed tactile sensor can be used in MIS and CBT. Further, The developed sensors can be used in robotics area for the purpose of human-robot interaction. However, it is of particular interest to use the tactile sensor in percutaneous mitral valve regurgitation repair. The left atrioventricular valve of the heart, the mitral

valve, controls the blood flow between the left atrium and the left ventricle as a one-way valve. The opening and closing dynamics of the mitral valve is governed by the blood pressure gradient and the complex force balance between the annulus, leaflet, atrium, and chordae tendineae [7]. Any malfunction of the mitral valve can lead to a cardiac trauma and can affect the heart ability to pump properly. *Mitral regurgitation* (MR) is a disorder in which blood flows back into the left atrium instead of being pumped into the body. Conventionally, open-heart surgery is the choice of treatment of MR, in which the surgeon uses tactile perception in the patient's body.

Following multiple meetings and brainstorming sessions, a novel concept for the repair of mitral valve regurgitation was reached by an expert team from McGill and Concordia Universities. This team included a leading heart surgeon from McGill University (Dr. Renzo Cecere), three members of the faculty of engineering at McGill University, and a faculty member from the department of mechanical and industrial engineering at Concordia University. The proposed idea was to install interrelated anchors around the mitral annulus by using a computer-controlled catheter; and then to tighten the connecting element of the anchors to reduce the size of annulus [8, 9]. Although the computer-controlled catheter is equipped with different mapping systems such as 3D ultrasound imaging systems, the exact recognition of the mitral valve annulus from surrounding tissues is nearly impossible without having tactile feedback from inside the heart [10]. Consequently, to localize the mitral annulus, it

would be advantageous to have resources to intelligent tactile sensing with a display during the operation. Mitral annulus is differentiable from the surrounding tissues, the leaflet and the atrium, because of its differences in geometry and hardness. The mitral annulus has a hinge point situation between the atrium at the top and the leaflet at the bottom. Both the leaflet and the atrium are softer than the annulus. The position of the mitral valve in a veal heart is shown in Fig. 1.1. The mitral valve of a veal heart is quite similar to the mitral valve of a human heart.

The annulus can be distinguished from the adjacent tissues, which are relatively softer, if an appropriate tactile sensor existed. Figure 1.2 shows a schematic view of the proposed MR surgery using a computer-controlled catheter. Several experiments have been conducted to prove the proposed technique, manually on ex-vivo veal and porcine hearts. Experiments have shown the validity of the overall idea. Figure 1.3 shows the experiment results, which indicate that the size of the mitral valve is reduced by installing anchors and tightening the connecting wire.

As shown in Fig. 1.2, the surgical catheter touches the heart tissue to perform surgery. Furthermore, the tactile sensor can differentiate different kinds of tissue by touching them. Understanding tool-tissue interaction is required to provide tactile and haptic feedback to the surgeon [11]; Hence, the contact mechanic between the tactile sensor and the tissue needs to be studied and modelled, appropriately. In the thesis, the contact interaction between the sensor and heart tissue is discussed and

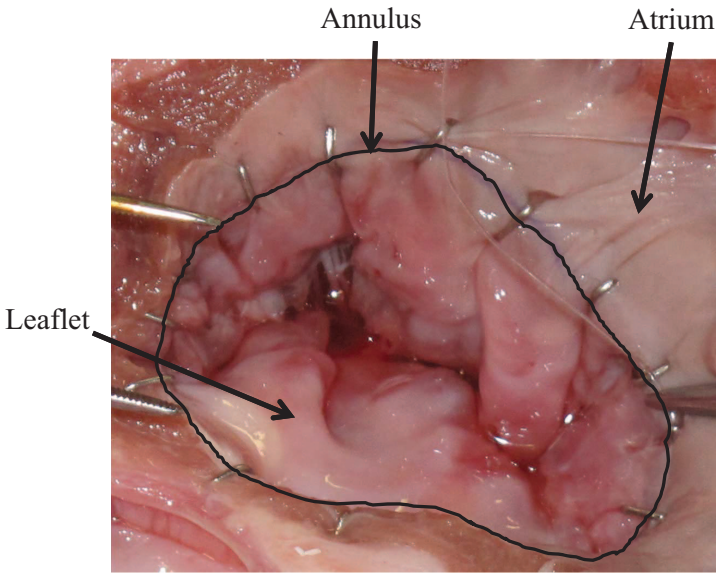

(a)

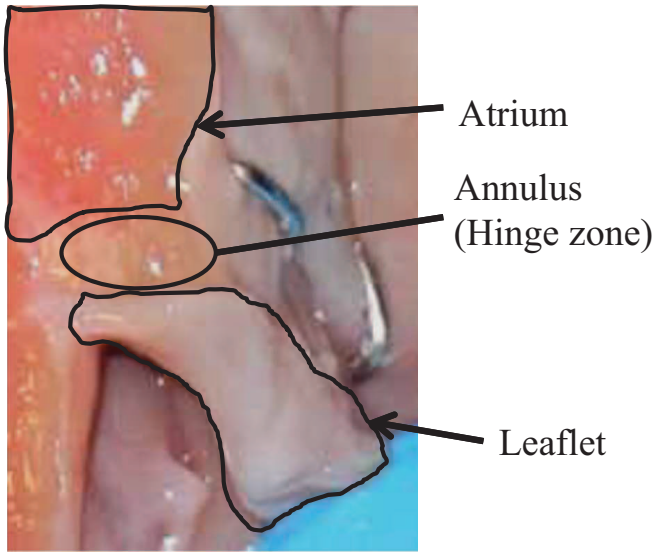

(b)

Figure 1.1: (a) The top view of the mitral valve: it consists of three main tissues, i.e., Annulus, Atrium, and Leaflet. The black line shows the annulus perimeter. (b) The cross section of mitral valve: the cross section of mitral valve shows that the atrium is surrounding the annulus ring from the top, and Leaflet is hanging from the annulus.

explained. The tissue is considered to be viscoelastic; and a viscoelastic contact model was developed parametrically for the tool-tissue interaction. Section 1.0.3 discusses the available contact models for surgical tools including the need for developing a parametric model. The developed model for viscoelastic contact can also be also used in surgical simulators to show the behaviour of soft tissues in contact with surgical catheters.

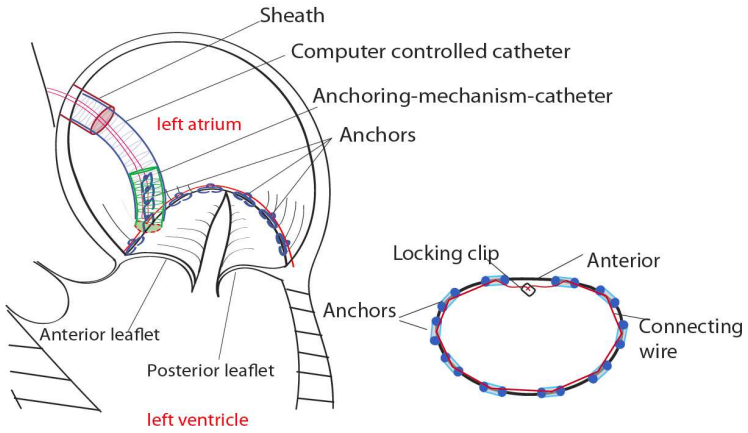

Figure 1.2: Schematic view of the proposed surgery technique

Since tissues show viscoelastic behaviour, the strain rate can also affect the stress-strain behaviour of tissues. This effect is more amplified when having several tissues with similar softness/hardness degrees. In other words, the softness/hardness perception for tissues can be changed without considering strain rate effect. Hence, the idea for the strain rate measurement during tactile sensing is proposed for the first time; and the idea is implemented in a new design of array tactile sensor. Available array sensors are discussed in Section 1.0.4.

Generally, the research on the tactile sensing side includes: (1) modeling of piezoresistive sensing element to use it as the force sensing element; (2) developing a new tactile sensor for MIS and CBT; (3) modeling the interaction of the sensor with atrial tissue during mitral annuloplasty repair surgery; and (4) developing a new array tactile sensor for tissues with viscoelastic behaviour.

The second part of the thesis is aimed at developing a three-dimensional tactile display that provides palpation capability to any surgeon performing robotic assisted MIS. In the literature, some research works were conducted to develop new techniques for finding hidden anatomical features during surgical operations [12, 13]. Surgeons in the course of open surgery commonly detect masses or stiffened tissues. Various diseases change the composition and consistency of biological tissues [14]. Tissue surrounding malignant tumours, for example, is generally softer than the tumours. Therefore, surgeons need to detect and precisely identify the location and size of all growths, whether cancerous or benign, that are present within surrounding tissue in order to assess the extent and nature of any future treatment plan. In the developed tactile display system, data is collected from two force/pressure matrices and processed with a new algorithm and graphically rendered. Consequently, the surgeon can determine the presence, location, and the size of any hidden superficial tumour/artery by grasping the target tissue in a quasi-dynamic way. Section 1.0.5 discusses the literature on available graphical display systems for MIS.

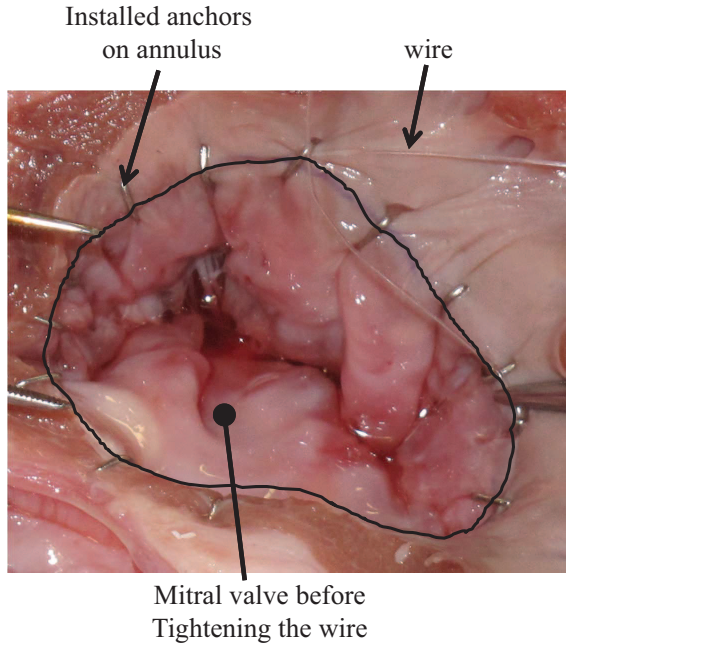

(a)

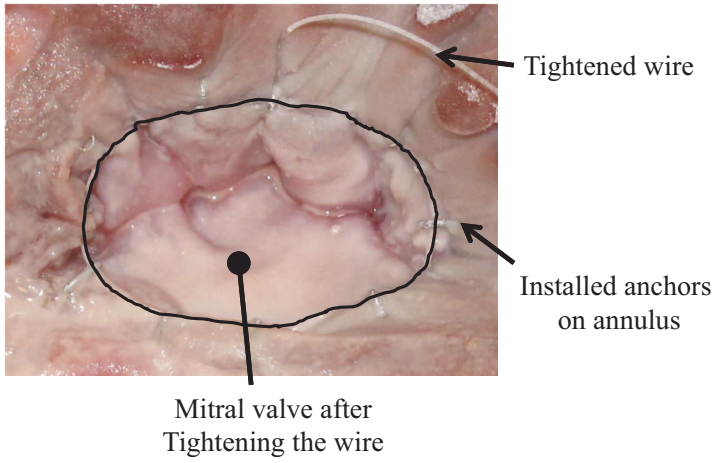

(b)

Figure 1.3: Reducing the mitral valve size of a porcine heart manually, for the proof of the proposed technique

1.0.1 Piezoresistive Sensing

The recent literature on modeling of semiconductive polymer composites are discussed in this section. Semiconductive polymer composites are used in a wide range of sensors and measurement devices, since early 1990s [15–22]. Recently, Nicola *et al.* proposed a biomimetic-fabric-based sensing glove, which is used for monitoring hand posture and gesture. They used a network of piezoresistive force sensors based on semiconductive polymer composites [23]. In another research work, Kawasaki *et al.* used distributed tactile sensors with 624 detecting points as the sensing element of a robot hand, named Gifu II [24]. Their distributed tactile sensor consists of a matrix of piezoresistive force sensors with semiconductive polymer composite elements. At the National Taiwan University, another similar robotic hand (the NTU hand) was developed by Lin and Huang who used the same type of sensors for robotic tactile perception [25]. Semiconductive polymer composites are suitable for use as pressure distribution sensors because of their simple structure in different applications [26,27]. Semiconductive polymer composites exhibit change in electrical resistivity caused by change in the force applied to their structure. Semiconductive polymer composites consist of impregnated nanoscale conductor particles inside the structure of a non-conductive material. The microstructure of conductor-filled polymer composites can be classified among the random whisker composites [28]. This is due to the fact that the conductive particles or fillers are randomly dispersed inside the structure of a

nonconductive matrix. The change of electrical resistance in semiconductive polymer composites occurs while changing the distance between conductor particles inside the matrix [29]. Wang *et al.* proposed a mathematical model for piezoresistivity of carbon-black-filled silicone rubber based on differences in carbon black contents [30]. They proposed a model of a piezoresistivity curve, which varies with different carbon black contents based on a shell model and tunneling current. Xie *et al.* [31] proposed a model for carbon-black-filled polymers under elongations. Hall *et al.* [32] proposed a calibration method for eliminating drift in force-sensing resistors (FSRs). In their proposed method, the drift of a force sensor was compensated by signal conditioning. However, they did not provide the theoretical basis for the drift of FSRs. Zhang *et al.* [33] proposed a model for predicting time dependency and piezoresistivity of conductor-filled polymer composites using interparticle separation change under applied pressure. Their developed piezoresistance model, however, does not take into account contact resistance. In addition, their proposed method for modeling creep is not suitable for polymer composites with viscoelastic behavior. In this work, a parametric model for semiconductive polymer composites is developed. Since polymeric materials have viscoelastic behaviour, they show creep as a result of application of pressure to their structure. The creep behaviour of semiconductive polymer composites is modelled and included in the general developed model. Further, the electrical

contact of the semiconductive polymer with electrodes are also developed and considered in the model. More details of the model is available in Chapter 2.

1.0.2 Tactile Sensing for CBT and MIS

The state of the art tactile sensors are elaborated in this section. Here, the main focus is the application of the tactile sensor for treatment of MR with CBT.

Nowadays, surgeons cannot use MIS or CBT with tactile feedback to perform mitral valve annuloplasty surgery, which is a common treatment of choice for MR [34]. In such surgical operation, surgeons must characterize three different types of cardiac tissues available at the site of operation. These tissues are mitral valve annulus, mitral valve leaflet, and atrium. The aim is to localize the annulus and perform the annuloplasty surgery, as is done in open surgery in which, surgeons use their visual and tactile perceptions to characterize these tissues. However, during CBT, surgeons suffer from a near total loss of visual perception and a total loss of tactile perception. Consequently, one solution would be to integrate tactile sensors with the tips of surgical tools, such as catheters, to mimic the tactile perception of the fingertips of surgeons by providing tactile feedback from the tool-tissue interaction.

Recently, several tactile sensors have been reported for use in MIS [35, 36]. More specifically, among such sensors, some designs have been proposed for use in CBT [37–39]. However, these sensors mainly measure only the contact force interacting between

surgical tools and tissues, and they cannot measure the relative hardness of contact tissues. For instance, an optical fiber-based sensor has been proposed to measure only the contact force interaction between catheters and the heart tissues without rendering any tactile information such as hardness [37]. Howe *et al.* has proposed a sensor to accurately measure the contact forces for use in beating heart intracardiac surgery [38,40]. More recently, in 2010, Polygerinos *et al.* [39] provided an overview of available sensors for use in cardiac catheterization procedures. All of these sensors are either a pressure or a force sensor that can only measure the contact forces between blood vessel walls and the catheter tip. The proposed tactile sensor in the present thesis is capable of measuring both the contact force and the relative hardness, which is required for mitral valve repair via CBT.

Generally, providing the force and tactile feedback is useful for both cardiac surgeons, who use CBT, and any other surgeon, who conducts MIS or MIRS. In fact, such artificial feedback enhances the performance of MIS and MIRS by helping the surgeons to characterize the contact tissues, and also to investigate the hidden anatomical structures of tissues. For such purposes, a wide range of force and tactile sensors have been introduced. For instance, king *et al.* have integrated a force feedback system with the da Vinci surgical robot [35, 41]. In their proposed system, a commercially available FlexiForce sensor and a pneumatic physical force display have been used to investigate the effects of only force feedback on grasping performance during MIRS.

The commercial force sensor used in their work can measure only the contact force.

Other sensors have been proposed to measure both the contact force and the distributed tactile information. Nevertheless, these sensors have been designed to be integrated with MIS and MIRS tools or surgical catheters. For example, Omata *et al.* [6] developed a tactile sensor that was able to detect the hardness/softness of an object impressed upon it. The principle behind the sensor is that the resonance frequency of a piezoelectric element would change if the element comes into contact with an object. In addition, measuring the stiffness of the tissue can provide useful information for tumour characterization [42–45]. As an example, Sokhanvar *et al.* [46, 47] proposed a tactile sensor for tissue characterization in MIS. However, their proposed sensor, which is a piezoelectric-based one, can perform only under dynamic loading conditions. This inadequacy of their sensor can be improved by using a sensing element that can perform under both static and dynamic loading conditions. In addition, recently proposed force and tactile sensors for providing tactile feedback in MIS and MIRS have been discussed by Puangmali *et al.* [36], and Schostek *et al.* [48], respectively. *Their reviews confirm that there is a need to develop robust tactile sensors for tissue characterization in MIS especially in CBT.*

A various number of these recently proposed sensors consist of moving parts, which might negatively affect the reliability of such sensors. The moving parts of the sensors tend to break in the case of any accidental misuse during operations, including the

application of excessive force to the sensor. Consequently, the development of a tactile sensor without having moving parts will address a lot of challenges involved in CBT. Further, such a tactile sensor must perform under both static and dynamic loading conditions similar to the tactile perception of the fingertips of surgeons. Chapter 3 discusses the details for the design, fabrication, test, and analysis of the developed tactile sensor that can address most of available mentioned problems.

1.0.3 Tool-tissue Modeling and Interaction

As mentioned before, treating MR with CBT technique is of particular interest. Therefore, understanding tool-tissue interaction is required to provide tactile and haptic feedback to the surgeon [11]; for example, to treat MR via CBT, the interaction of surgical device and heart tissue should be investigated [49]. Therefore, a contact model between tactile sensor and tissue becomes a key factor for the optimum design of surgical instruments and tactile sensors [50]. To develop the contact model, tissue behaviour should be investigated, first.

The knowledge of tissue behaviour has many applications in different areas, such as surgical simulations and haptic feedback in Robotic-assisted Surgeries (RAS) [51,52]. Researchers have long been aware that soft tissues exhibit viscoelastic behaviour [53]. Lumped-parameter models are often used for the modeling of tissue by virtue of their simplicity and fast response with relatively realistic deformation replication

[54, 55]. For example, three- and four-parameter constitutive models are widely used to represent the viscoelastic behaviour of different kinds of soft tissue [56, 57].

To model the interaction of the sensor with heart, atrial tissue of heart was modelled first, by using the concept of generalized Kelvin model, which gives a good representation of tissue behaviour. Hence, a generalized Kelvin model with 17 parameters was used in this work to model the atrial tissue of a porcine heart, as the three-parameter model cannot accurately represent the atrial tissue behaviour. *In vitro* experiments were also conducted on the atrial tissue of a porcine heart by means of dynamic mechanical analysis (DMA) to characterize tissue properties. A genetic algorithm was used to find the constants of the viscoelastic model, which is populated with data from DMA tests. Then, the viscoelastic model of the tissue was embedded in the contact model.

With regards to contact modeling methods, mass-spring and finite element models are widely adopted for analyzing the tool-tissue interaction in biomechanics. For example, Nedel *et al.* used a mass-spring model that can give rise to a natural and smooth deformation in the simulation of muscle [58]. Another mass-spring mesh model was used in the analysis of the suturing of small blood vessels [59]. Although the mass-spring model has some advantages, such as easy construction and low computation demands, it is difficult to express realistic contact properties using this model. Some researchers have used the finite element analysis (FEA) to have more

realistic models contact analysis [60]. For example, FEA was used in the contact modeling of tissue in surgery simulation [61], needle insertion [62], and soft-tissue cutting model [63]. For articular cartilage and other hydrated tissue, biphasic finite elements were used by Yang and Spilker [64]. Since the discretization involved in the FEA framework, the analysis performed on each nodal point of the finite element mesh can lead to discontinuity problems [65]. Additionally, FEA involves heavy computation demands, which do not allow for realtime computations.

For special problems, researchers have derived parametric closed-form solutions that overcome the above-mentioned disadvantages of mass-spring and models based on FEA. A mathematical model for frictionless elastic contact was used for joint articulation [66]. An approximation of a closed-form solution was also obtained for contact of two biphasic cartilage layers [67]. Recently, a closed-form solution of a contact problem between subchondral bone and articular cartilage was reported [68]. To the best of our knowledge, there are only limited parametric models available for contact of viscoelastic tissue with surgical tools that have annular shape, the case for some surgical catheters and tactile sensors.

Due to the considerable hardness difference between tissue and tactile sensor, tool-tissue interaction is modelled as a problem of a rigid indentor in contact with viscoelastic tissue. Similar to elastic contact, two categories exist in the presence of viscoelastic materials, *complete* and *incomplete* contact. Several viscoelastic contact

models have been developed by researchers for the indentation of viscoelastic materials [69, 70]. However, most of the models pertain to the indentation of tissue with conical or spherical indentors for incomplete contact problems [71]. In complete contact, the corresponding principle is mainly used to convert viscoelastic contact into elastic contact [72]. Chapter 4 discusses the details of the developed contact model for the interaction of tactile sensor with soft atrial tissue.

1.0.4 Array Tactile Sensor Configuration

The general review of literature for tactile sensor designs and drawbacks inspired the idea for the development of a new generation of tactile sensors, based on array sensors. As mentioned earlier, the developed array tactile sensor can measure the rate of applied force and the rate of applied displacement, in addition to force and displacement measurement. The measurement of force rate and displacement rate plays an important role in distinguishing different types of soft tissues with viscoelastic behaviour. This property can be helpful in robotic hands [73, 74] and in surgical applications.

Recently, many types of tactile sensors are developed for robotic arms and graspers. Recently, Dahiya *et al.* developed a PVDF matrix of tactile sensors for robotic grasping application [75]. Their developed tactile sensing chip can measure the dynamic

contact force in robotic application. Aoyagi *et al.* in a similar research work developed a matrix of capacitance sensors—embedded in PDMS for flexility—for robotic application. They used a neural network algorithm to compare the output of different sensors to estimate the components of the contact force in x, y, and z direction [76]. In another study, Hu *et al.* developed a piezoresistive array of tactile sensors to monitor the pressure rate of foot for wearable smart device application. Their sensor measured the local pressure versus time. In all of these developed tactile sensors, only the contact force/pressure is measured during the touch; and the sensors fail to extract any data about the softness of materials being touched.

In a recent two review articles of Dahiya *et al.* and Tiwana *et al.*, there is lack of tactile sensors that are suitable for determining the difference between two soft material, e.g. tissues, with viscoelastic properties [77, 78]. Our new developed tactile sensor is capable of distinguishing the difference between several soft tissues with viscoelastic behaviour.

The details of the design and the concept of the tactile sensor is explained in Chapter 5.

1.0.5 Tactile Display

The human hand performs many tasks during surgery, which is hard to reproduce in robotic surgery. For example, during complex abdominal surgery, the surgeon may

frequently be required to place his/her hand into the abdominal cavity, which is not possible during laparoscopic surgery. Although computed tomography (CT) or magnetic resonance imaging (MRI) provide surgeons with images from area with tumors, the surgeon must still actively palpate the tissue to detect and localize tumours. In addition to locating tumours, it is important that the surgeon be able to detect the presence of arteries hidden under covering tissue in order to prevent accidental dissection and internal bleeding [79]. Currently, different methods are used by surgeons to localize tumours and arteries, but each technique has certain shortcomings and can often cause confusion necessitating a full thoracotomy. The usual method is to use a long metal rod inserted through a port to feel the presence of hard nodules within the soft tissue [80]. For tumours located in deeper areas, this technique is not very effective so, in order to confirm the existence and location of a tumour, the surgeon may insert a finger inside the incision to palpate the tissue [80]. In some methods, before surgery, a marker is inserted near the tumour by using CT guidance [81]. In recent years, however, researchers have presented new techniques for tumour detection and localization. Kawahara *et al.* [82] proposed a method whereby the tissue was deformed by using air bursts; the extent of the deformation was measured by means of a laser detection system. Peine [83] developed a tactile display system integrated into a hand-held surgical probe in which a shape display regenerates the contact pressure measured by a tactile sensor. Dargahi *et al.* proposed a laparoscopic tactile sensor

with piezoelectric softness sensors [84, 85]. Takashima *et al.* [86] proposed a tactile sensor in which the relative motion between a transparent window and the end of an endoscope is measured using image-processing methods. In this work, an advanced feature is developed that renders the presence of a possible lump/artery in realtime 3D. The developed 3D rendering system is discussed in more detail in Chapter 6.

1.1 Thesis Objective and Scope

To summarize the introduction, the objective of this thesis is to develop tactile sensor and a feedback system for MIS and MR treatment by MIRS. To this end, the specific objectives of this thesis is classified in four main categories as below:

1. Modeling the piezoresistive sensing behaviour of force sensing resistors, which includes:

   (a) Review of available models for semi-conductive polymer composites and their drawbacks

   (b) Electrical contact resistance of the force sensor in the developed model

   (c) A model for the creep behaviour of Linqstat as the sensing element of force sensor based on experimental tests

   (d) Several tests and experiments on linqstat material, e.g. the results of scanning electron microscopy (SEM) and Thermogravimetric Analysis (TGA)

(e) A novel parametric model for piezoresistive force sensors

2. Developing a new tactile sensor for MIS and CBT application, which includes:

   (a) Review of available tactile sensors for MIS and CBT and their drawbacks

   (b) Methods of testing and fabrication

   (c) Finite element modeling of the sensor and phantom tissues

   (d) A new tactile sensor for MIS and CBT

3. Developing a viscoelastic model for contact interaction of the tactile sensor and tissue, including:

   (a) Review of available techniques for contact modeling

   (b) Contact problem definition

   (c) Combination-of-harmonics method to solve the contact problem

   (d) A viscoelastic model of tissue based on dynamic mechanical analysis and test experiments

   (e) A new parametric model for the viscoelastic contact

4. Developing a new array tactile sensor for distinguishing tissues with viscoelastic behaviour, including:

   (a) Review of available array tactile sensors

(b) Tissue-testing experimental setup

(c) New sensing algorithm development

(d) Design and fabrication of the array tactile sensor

5. Developing a 3D graphical tactile display system for visualizing embedded lumps and arteries during MIS, including:

(a) Review of the available graphical tactile rendering methods

(b) Fabrication and calibration of two piezoresistive force sensor matrix

(c) Development of a 3D lump localization algorithm in LabView

(d) Finite element modeling of different conditions for embedded lumps and arteries

(e) A new 3D graphical display for MIS

1.2 Contributions of Authors

The present thesis is presented in manuscript-based format in six chapters. The thesis is composed of *four published journal articles, one to be submitted journal article, and four published conference articles.* This thesis is organized and formatted based on "Thesis Preparation and Thesis Examination Regulations (version-2011) for Manuscript-based Thesis" of the School of Graduate Studies at Concordia University.

The motivation of the thesis, literature survey, and thesis objectives and scope are addressed in Chapter 1. The literature review includes a comprehensive but brief survey on the piezoresistive sensing, tactile sensing in MIS and CBT, tool-tissue modeling and interaction, and tactile graphical displays.

Chapter 2 presents a novel parametric model for piezoresistive force sensor based on the following published journal article in the IEEE/ASME Transaction on Mechatronics [87]:

1. *Kalantari, M., Dargahi, J., Kövecses, J., Mardasi, M., and Nuri, S., 2011. "A new approach for modeling piezoresistive force sensors based on semiconductive polymer composites". IEEE/ASME Transactions on Mechatronics, 17(03), pp. 572–581*

The contribution of M. Mardasi and S. Nuri was in electrical contact modeling and viscoelastic modeling of Linqstat.

Chapter 3 presents the novel design of a tactile sensor based on the following published journal article in the International Journal of Medical Robotics and Computer Assisted Surgery, and two conference papers published in Proceedings of IEEE Haptics Symposium and Proceedings of IEEE 37th Annual Northeast Bioengineering Conference [88–90], as below:

1. *Kalantari, M., Ramezanifard, M., Ahmadi, R., Dargahi, J., and Kövecses, J., 2011. "A piezoresistive tactile sensor for relative tissue characterization during*

catheter-based cardiac surgery". International Journal of Medical Robotics and Computer Assisted Surgery, 7(4), pp. 431–440

2. *Kalantari, M., Ramezanifard, M., Ahmadi, R., Dargahi, J., and Kövecses, J., 2010. "Design, fabrication, and testing of a piezoresistive hardness sensor in minimally invasive surgery". In Proceedings of IEEE Haptics Symposium, Boston, USA, March 2010, pp. 431–437.*

3. *Kalantari, M., Shen, J., Dargahi, J., Kövecses, J., and Zadeh, M., 2011. "Localization of annulus with a tactile sensor". In 2011 IEEE 37th Annual Northeast Bioengineering Conference (NEBEC), pp. 1–2.*

The contribution of M. Ramezanifard, R. Ahmadi and J. Shen was in conducting experiments.

Chapter 4 presents a parametric model for the viscoelastic contact of the developed tactile sensor with biological tissues, based on a published journal article in IEEE Transaction on Biomedical Engineering and a published conference article in 2011 CCToMM Symposium on Mechanisms, Machines, and Mechatronics [91,92] as below:

1. *Shen, J., Kalantari, M., Kövecses, J., Angeles, J., and Dargahi, J., 2011. "Viscoelastic modeling of the contact interaction between a tactile sensor and atrial tissue". IEEE Transactions on Biomedical Engineering, 59(6), pp. 1727–1738*

2. *Shen, J., Kalantari, M., Kövecses, J., Angeles, J., and Dargahi, J., 2011. "Measuring the properties of heart tissue with dynamic mechanical analysis method". In Proceedings of the 2011 CCToMM Symposium on Mechanisms, Machines, and Mechatronics (2011 CCToMM M3), Montral, Qubec, Canada.*

The contribution of J. Shen was in the contact modeling part of the paper.

Chapter 5 presents a novel array tactile sensor design based on piezoresistive sensing elements for soft tissue. The new idea of displacement rate measurement is introduced by this array sensor. This chapter is to be submitted to as a journal article.

1. *Kalantari, M., Dargahi, and J., and Kövecses, J., "A novel array tactile sensor for hardness measurement of viscoelastic tissue". To be submitted*

Chapter 6 presents a new 3D graphical tactile display for MIS based on a published journal article in the ASME Journal of Medical Devices, and a published conference article in the proceedings of ASMEs 2010 Frontiers in Biomedical Devices Conference [93, 94], as below:

1. *Kalantari, M., Ramezanifard, M., Dargahi, J., and Kövecses, J., 2011. "3D graphical rendering of localized lumps and arteries for robotic assisted MIS". Journal of Medical Devices, 5(2), p. 021002.*

2. *Kalantari, M., Ramezanifard, M., Ahmadi, R., Kövecses, J., and Dargahi, J.,*

2010. "2D lump/artery detection by using piezoresistive force sensors". In ASMEs 2010 5th Frontiers in Biomedical Devices Conference & Exhibition, ASME Press.

The contribution of M. Ramezanifard was the LabView code development, and the contribution of R. Ahmadi was in conducting experiments.

Chapter 7 presents a comprehensive conclusion for all of the chapters, contributions, and suggested future works.

Chapter 2

Modeling Piezoresistive Force Sensors Based on Semiconductive Polymer Composites

This chapter discusses the development of a model and a new theoretical formulation for predicting piezoresistive behavior in semiconductive polymer composites. In addition, the contact resistance is considered between the electrodes and polymer composites in the formulation. The relationship between electrical resistance and force applied to the piezoresistive force sensor can be predicted by using the proposed theoretical formulation. In order to verify the proposed formulation, the piezoresistive behavior of Linqstat, a carbon-filled polyethylene, was modeled mathematically.

Further, some experimental tests, such as thermo gravitational analysis and Scanning electron microscope (SEM), have been performed on Linqstat to find the volume fraction and size of carbon particles, which are essential for modeling. On a fabricated force sensor using Linqstat, a force-resistance curve was obtained experimentally, which verified the validity and reliability of the proposed formulation.

Semiconductive polymer-composite force sensors show drift in their output. The reason for drift in such force sensors could be due to the creep behavior of the semiconductive polymer composite used as the sensing element. If a polymer composite such as Linqstat (a patented name) is subjected to a constant force, it exhibits creep behavior, which causes the drift in the output of the force sensor [33]. In order to include the drift of the force sensor in the formulation, a viscoelastic model is used to represent semiconductive polymer composites based on their creep behavior. Hence, the strain rate of semiconductive polymer composites is formulated and used in the proposed formulation. To verify the validity of the proposed formulation, an experimental setup was prepared and various tests were performed. Linqstat, as an industrial semiconductive polymer composite, was selected to be tested. Furthermore, an accurate force sensor, made from Linqstat material, was developed and calibrated. The force-resistance curve of the sensor was determined and compared with the proposed formulation. In addition, a creep test was conducted on Linqstat and the results were compared to the model predictions.

2.1 Development of the Proposed Formulation

2.1.1 Review of Related Formulation

In semiconductive polymer composites, the matrix is selected from nonconductive polymers, while the filler is selected from conductive materials. By subjecting the polymer composite to compressive stress, the filler particles inside the matrix start to display micro-Brownian motion [30]. The fillers move closer to each other because of the strain in the matrix, which causes a change in the electrical resistance of the polymer composite. There are two main types of resistances that cause a change in resistivity within the composite, namely, constriction resistance and tunneling resistance. It was shown [29] that the total resistance of the polymer composites can be given as

$$R = \frac{(L-1)\,R_m + LR_c}{S} \tag{2.1.1}$$

where R_m is the resistance between two adjacent filler particles, R_c is the resistance across a single filler particle, L is the number of particles forming one conductive path, and S is the total number of effective conduction paths. The tunneling current would flow through a gap between adjacent particles [95]. The tunneling current at low applied voltages [96] can be written as:

$$J = \frac{3\sqrt{2m\varphi}}{2s}\left(\frac{q}{h}\right)^2 V e^{-\left(\frac{4\pi s}{h}\sqrt{2m\varphi}\right)} \tag{2.1.2}$$

where q and m are electron charge and mass respectively, φ is the height of the potential barrier between two adjacent filler particles, h is Plank's constant, V is the applied voltage, and s is the thickness of the insulating film. The height of the potential barrier can be extracted from the work function of the polymer. The φ between adjacent particles in a composite can be calculated by subtraction of the polymer (matrix) work function from the filler work function. In this current project, carbon black and polyethylene is used as the filler and matrix, respectively. Therefore, the required potential height of carbon black and polyethylene is considered as 0.05 (eV) [97]. The tunneling resistivity is proportional to area a^2 [33] of the contact between two filler particles,

$$R_m = \frac{V}{a^2 J} = \frac{8\pi s}{3a^2\gamma q^2} e^{\gamma s} \tag{2.1.3}$$

where J is the tunneling current, and

$$\gamma = \frac{4\pi}{h}\sqrt{2m\varphi} \tag{2.1.4}$$

By putting R_m in eq.(2.1.1), and equating $L - 1 \sim L$, [33] the total resistance can be introduced as

$$R = \frac{L}{S}\left[\frac{8\pi s}{3a^2\gamma q^2}\ e^{\gamma s}\right] + \frac{L}{S}R_c \tag{2.1.5}$$

In this current research work, carbon black is selected to be the filler particle inside the matrix. The matrix is selected to be a nonconductive material with high resistance. Therefore, the resistance of carbon black, R_c, which is highly conductive can

be considered negligible. So, $\frac{L}{S}R_c$ in the above equation is omitted for the coming derivations. By dividing the actual resistance with the initial resistance [33], the following formula is obtained.

$$\frac{R}{R_0} = \frac{s}{s_0} e^{-\gamma(s_0 - s)} \tag{2.1.6}$$

where R_0 is the initial resistance of the composite, and s_0 is the initial distance between two adjacent filler particles. As a result of application of stress to the composite, it is also assumed that only the polymer (matrix) would carry the load. The deformation of the filler particles is in the range of a few nanometers, which is negligible in comparison with that of the matrix. The inter-particle separation distance [33] can be simply shown as

$$s = s_0 \left(1 - \varepsilon\right) \tag{2.1.7}$$

where ε is the strain of the polymer matrix which could be considered time dependent. Wu [98] showed that the inter-particle separation between two spherical fillers can be calculated from the following relation

$$s_0 = D \left[\left(\frac{\pi}{6\phi} \right)^{1/3} - 1 \right] \tag{2.1.8}$$

where D is the filler particle diameter, and ϕ is the volume fraction of filler particles. By substituting eqs.(2.1.7) and (2.1.8) into eq.(2.1.6), similar to that shown in [33], it can be written that

$$\frac{R}{R_0} = \left(1 - \varepsilon\right) e^{-\gamma D \varepsilon \left[\left(\frac{\pi}{6\phi} \right)^{1/3} - 1 \right]} \tag{2.1.9}$$

As mentioned earlier, R_0 is the initial resistance of the polymer composite which can be measured by precise measurement techniques.

2.1.2 Working Principle of a Piezoresistive Force Sensor

In a typical force sensor that uses polymer composites, a thin layer of the polymer composite is sandwiched between two layers of electrode. The electrodes are then covered with two layers of polyester films. Figure 2.1a shows the schematic view of the components of such a sensor.

When a compressive force is applied to the surface of the force sensor, its resistance drops due to a decrease in the resistance of the piezoresistive polymer, and also due to a slight decrease in the contact resistance between the conductors and the piezoresistive polymer. In other words, applying force causes a decrease in distance between filler particles inside the matrix, and an increase in the number of conductive paths which leads to a decrease in the resistance of polymer composites. Because there is no adhesive between the electrodes and the polymer in the fabrication process, when force is applied air between the electrode and polymer would leave from the air vent in the tail of the sensor. This results in a sudden decrease in contact resistance between the electrodes and the polymer composite. As shown schematically in Fig. 2.2, the average distance between conductor particles would decrease by applying force to the sensor.

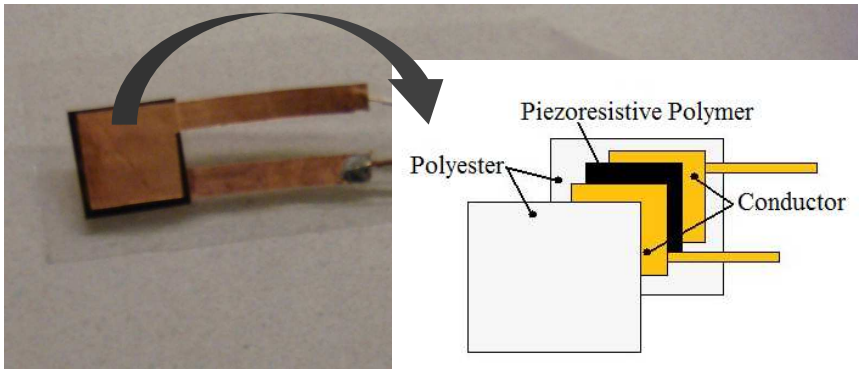

(a)

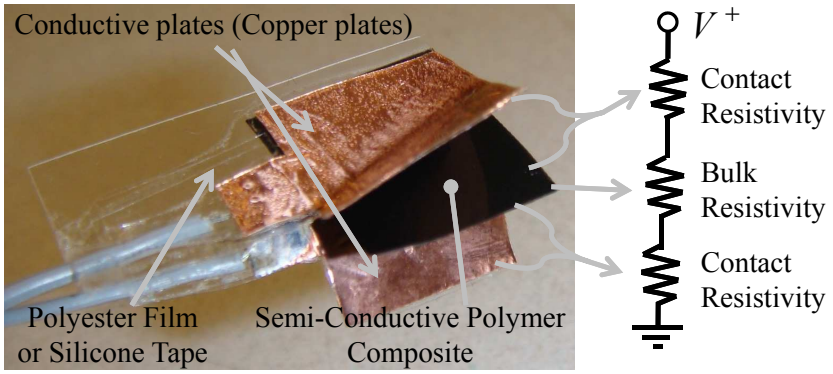

(b)

Figure 2.1: (a) View of the fabricated force sensor using Linqstat and its components (b) The schematic view of current flow geometry

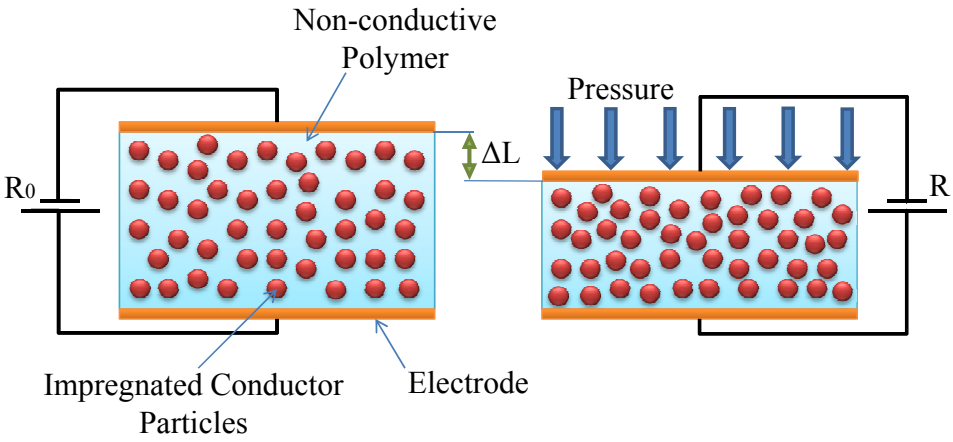

Figure 2.2: Schematic view of the piezoresistive force sensor based on semiconductive polymer composites materials. The figure shows the working principle of the sensor.

2.1.3 Contact Resistance

In order to obtain an accurate reading of the force sensor output, the contact resistance between electrodes and the polymer composite was taken into account. It has been shown that the effective contact area between two adjacent members is only a small fraction of the apparent macroscopic area of contact [99]. Looking at the contact interface on a microscopic scale, the roughness of surfaces would be evident. Therefore, the electrical contact would take place on both separable mating surfaces through asperities, or a-spots [100]. In the present work, it is assumed that there is no film resistance caused by thin oxide layers on the contact surfaces since the polymer, polyethylene, does not oxide in the room temperature. Therefore, based on this assumption total resistance of the force sensor which is read by a measurement system attached to the sensor can be written as

$$R_{total} = 2R_{Con} + R_{Pol} \tag{2.1.10}$$

where R_{total} is the total resistance of the sensor, R_{Con} is the contact resistance between each electrode and polymer composite, and R_{Pol} is the resistance of the polymer composite which is to be determined. Figure 2.1b shows the schematic view of the total electrical resistance of the sensor. By using the Holm and Greenwood formula [101], the contact resistance can be written as

$$R_{Con} = \frac{\rho_1 + \rho_2}{4na} \tag{2.1.11}$$

where ρ_1 and ρ_2 are the electrical resistivity of the two materials in contact, a is the radius of a-spot, and n is the number of a-spots. The number and the radius of a-spots increase when force is applied to the contact surfaces. Figure 2.3 shows the change in the number of electrical contacts and the change of the interface of two adjacent members upon applying force. All of the a-spots can be assumed as having

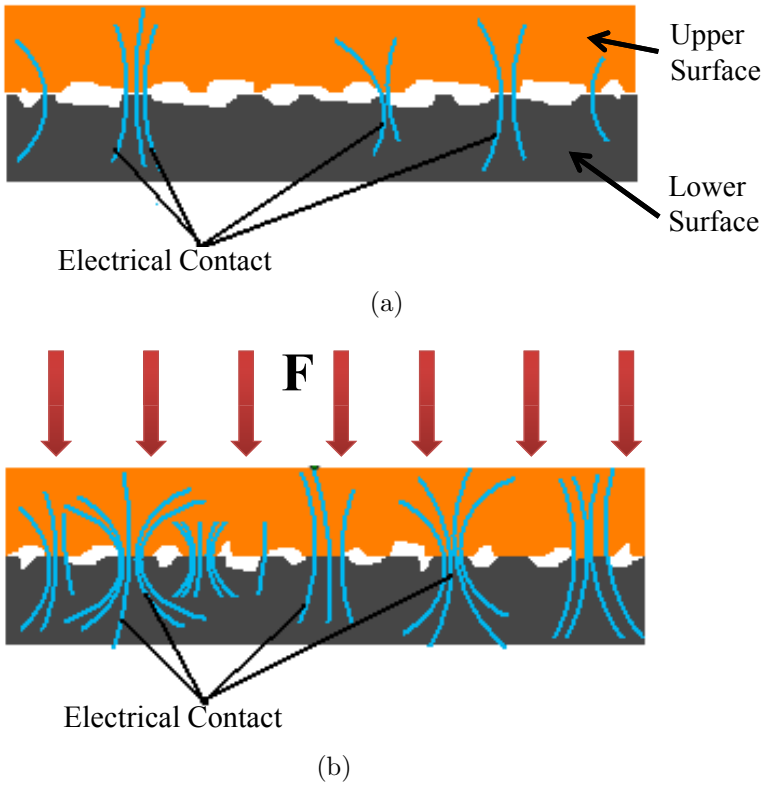

Figure 2.3: The schematic view of current path through contact (a) unloaded contact area (b) loaded contact area

an effective contact area which is affected by the applied force [102]. An increase in this applied force results in a larger effective area. From Fig. 2.3, it can be seen that when force is applied, there still exists some area between the two surfaces which are

not in contact, known as ineffective regions. The effective area could be written as the summation of all a-spots. Holm [99] presented a formula about contact resistance between different members with contact forces of 0 to 100N as

$$R_{Con} = \frac{\rho_1 + \rho_2}{4}\sqrt{\frac{\pi H}{F}} \tag{2.1.12}$$

where ρ_1 and ρ_2 are the electrical resistivity of the two materials, F is the applied force, and H is the Meyer hardness of the softer member.

2.1.4 Resistance of Semiconductive Polymer Composite by Considering Contact Resistance

The equivalent resistance of a piezoresistive sensor can be derived using the formulation presented in the previous sections. The following shows the total change in resistance of a semiconductive polymer composite caused by applied load. By substituting eqs.(2.1.9) and (2.1.12) into eq.(2.1.10), we can write

$$R_{total} = 2R_{Con} + R_{Pol} = \frac{\rho_1 + \rho_2}{2}\sqrt{\frac{\pi H}{F}} + R_0\left(1-\varepsilon\right)e^{-\gamma D\varepsilon\left[\left(\frac{\pi}{6\phi}\right)^{1/3}-1\right]} \tag{2.1.13}$$

$$R_{Con} = \frac{\rho_1 + \rho_2}{4}\sqrt{\frac{\pi H}{F}}$$

$$R_{Pol} = R_0\left(1-\varepsilon\right)e^{-\gamma D\varepsilon\left[\left(\frac{\pi}{6\phi}\right)^{1/3}-1\right]}$$

$$\gamma = \frac{4\pi}{h}\sqrt{2m\varphi}$$

Volume fraction of carbon particles	0.2873
Diameter of carbon particles (nm)	500
Thickness of Linqstat (mm)	0.2
Resistivity of Linqstat (Ω·cm)	500
Hardness (Meyer)	52
Active area of the force sensor (mm × mm)	15×15
Resistivity of Copper electrodes (Ω·cm)	0

Table 2.1: Some of mechanical and electrical properties of Linqstat

where ρ_1 and ρ_2 are the electrical resistivity of two materials in contact , H is the Meyer hardness of the softer member, F is the applied force, R_0 is the initial resistance of the semiconductive polymer composite, ε is the strain, D is the filler particle diameter, ϕ is the volume fraction of the filler particles, h is Plank's constant, m is electron mass, and φ is the height of the potential barrier between two adjacent filler particles. The measured parameters are listed in Table 2.1.

2.1.5 Modeling Creep Behavior

After reviewing the total resistance results from eq.(2.1.13), it is clear that the total resistance of the sensor is a function of the material properties of the semiconductive polymer composite, the applied force, and the induced strain. The strain in eq.(2.1.13) is considered constant for constant forces. However, in a real situation, the strain changes slightly with time while having a constant force on the material. In other words for a constant force, the strain is not constant due to the creep, and

changes with time. The reason is that when a constant force is applied, semiconductive polymer composites show creep behavior due to the viscoelastic properties inherent within all polymers. The creep of the polymer composites appears as drift in the force sensor output. Therefore, by applying a constant force to the force sensor, the resistivity decreases with time. For the prediction of creep behavior in semiconductive polymer composites a model is developed based on spring-damper elements. Polymers behave as an elastic solid in some instances, and as a viscous fluid in other cases; they can generally be considered using viscoelastic material models [103]. A single Maxwell or a single Kelvin-Voigt element cannot represent the transient and instantaneous response of polymers accurately. Hence, using a combination of the two elements is recommended [104–107]. The strain in a creep test of semiconductive polymer composites, such as Linqstat which is used when fabricating a force sensor, tends towards a constant value after a longer period of time. In fact, the impregnated carbon particles inside the polyethylene matrix, which is a thermoplastic polymer, change the mechanical properties of the composite similar to those of thermosets. These results were obtained after several accurate creep tests on Linqstat using a BOSE ELECTROFORCE 3200 device. Therefore, a standard linear solid model with three-parameters, shown in Fig. 2.4a, is used for modeling the creep in semiconductive polymer composites such as Linqstat. In fact the creep curves of both the Linqstat and standard linear solid model are very similar to each other, due to the fact that

the strain in both of them tends toward a constant value with time. Since the creep behaviour of the Linqstat is being modeled, the standard linear solid model becomes the best fit for this purpose. Figure 2.4a illustrates the selected lumped-parameter model and the creep curve for the standard linear solid model as well. The consti-

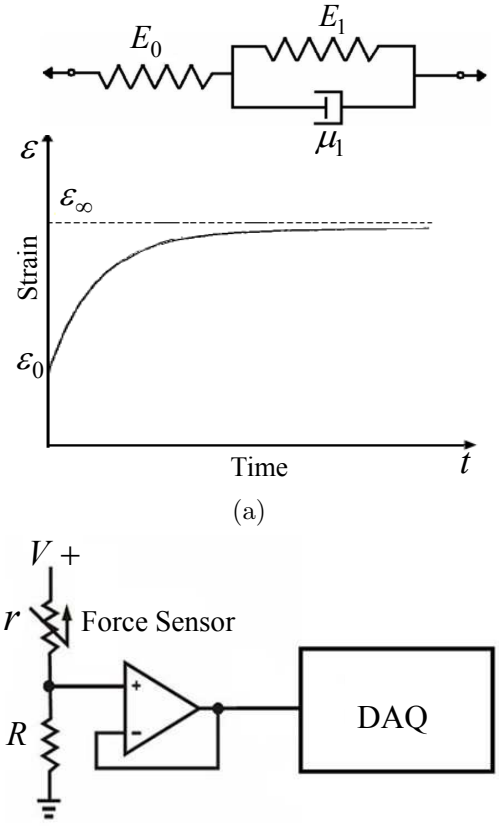

Figure 2.4: (a) Three parameters solid model and the creep behavior of it (b) The electric circuit of a single force sensor connected

tutive equation of the standard linear solid model, governing the behaviour of the

element, is written as [103]

$$\sigma + \frac{\mu_1}{E_0 + E_1}\dot{\sigma} = \frac{E_0 E_1}{E_0 + E_1}\,\varepsilon + \frac{\mu_1 E_0}{E_0 + E_1}\,\dot{\varepsilon} \tag{2.1.14}$$

where ε is the induced strain, σ is the applied stress, is the strain rate, is the stress rate, E_0 and E_1 are elastic modulus of the springs, and μ_1 is viscosity of the damper element as shown in Fig. 2.4a. In this work only the compressive stress component is of interest which is normal to the plane of the sensor as shown in Fig. 2.4a. Thus, other stress and strain components would not be taken into consideration and the main stress or force component would be in the z direction. To find E_0, E_1, and μ_1, the creep test conditions are applied to the constitutive eq.(2.1.14). The equation can then be solved and the coefficients determined according to experimental data. In a creep test, a constant stress is applied to the sample and maintained for the duration of the test. Therefore, the stress is constant and the stress rate is zero. So by inserting these two conditions into eq.(2.1.14), the constitutive equation is changed to a first order differential equation of strain. By solving the first order differential equation and by converting the stress to the corresponding force element [103], the induced strain as a function of time is written as

$$\varepsilon(t) = \frac{F}{AE_0} + \frac{F}{AE_1}\left(1 - e^{-\frac{\mu_1}{E_1}t}\right) \tag{2.1.15}$$

where $\varepsilon(t)$ is the induced strain, and A is the corresponding area of the force sensor, F is the applied force, E_0 and E_1 are elastic modulus of the springs, μ_1 is viscosity of

the damper element, and t is the time. The stress is converted to force in eq.(2.1.15). The coefficients E_0, E_1, and μ_1 are then determined experimentally and are calculated from the creep curve of semiconductive polymer composites.

2.1.6 Modeling of the Total Resistance

By considering time dependency of strain, eq.(2.1.15) could be substituted into eq.(2.1.9) resulting in a new time dependent expression for the resistance of polymer. In this expression, the creep behaviour is modeled and included in the formulation as discussed before. The new formula for the resistance of polymer, including the creep effect could be written as

$$R_{Pol*} = R_0 \left[1 - \left(\frac{F}{AE_0} + \frac{F}{AE_1}(1 - e^{-\frac{\mu_1}{E_1}t})\right)\right] e^{-\gamma S_0\left[\frac{F}{AE_0} + \frac{F}{AE_1}\left(1 - e^{-\frac{\mu_1}{E_1}t}\right)\right]} \tag{2.1.16}$$

where S_0 can be found from eq.(2.1.8), and γ can be found from eq.(2.1.4). Therefore, the final relationship between the resistance of a semiconductive polymer composite and the applied force taking into account the effects of contact and creep can be written as

$$\begin{aligned} R_{total*} &= 2R_{Con} + R_{Pol*} = \\ &= \frac{\rho_1 + \rho_2}{2}\sqrt{\frac{\pi H}{F}} + R_0 \left[1 - \left(\frac{F}{AE_0} + \frac{F}{AE_1}(1 - e^{e^{-\frac{\mu_1}{E_1}t}})\right)\right] e^{-\gamma S_0\left[\frac{F}{AE_0} + \frac{F}{AE_1}\left(1 - e^{-\frac{\mu_1}{E_1}t}\right)\right]} \end{aligned} \tag{2.1.17}$$

2.2 Experiments

2.2.1 Experimental Setup

In order to verify the validity of the proposed formulation, creep tests were performed on Linqstat from which, a force sensor was subsequently fabricated with the intention of its being used. The fabricated force sensor is intended to be used as an element of a force sensor array in minimally invasive surgery applications. The resolution of the fabricated force sensor is 0.1 N. The formulation proposed above can be used to optimize the sensor by eliminating drift and obtaining a better output. The fabricated force sensor, as shown in Fig. 2.1a, has one input/output port. The sensor must be fed by a constant DC voltage supply. The input voltage to the sensor was set to 5V. The sensor was then connected to a buffer circuit which, in turn, was connected to a PC via a Data Acquisition (DAQ) board. The buffer circuit was used to reduce the loading effect of the force sensor on the DAQ amplifiers. Consequently, the cross talk between the different input channels of the DAQ system was minimized. To relate the force sensor output, measuring DC voltage, to the sensed force, a calibration procedure was implemented. Experimental data showed that the force (F) applied to the sensor has a linear relationship with the conductance (C), Fig. 2.5b shows the force and conductance relationship in which $C = mF + n$, where m and n are constants [89]. The circuit in Fig. 2.4b was used to find the relationship between

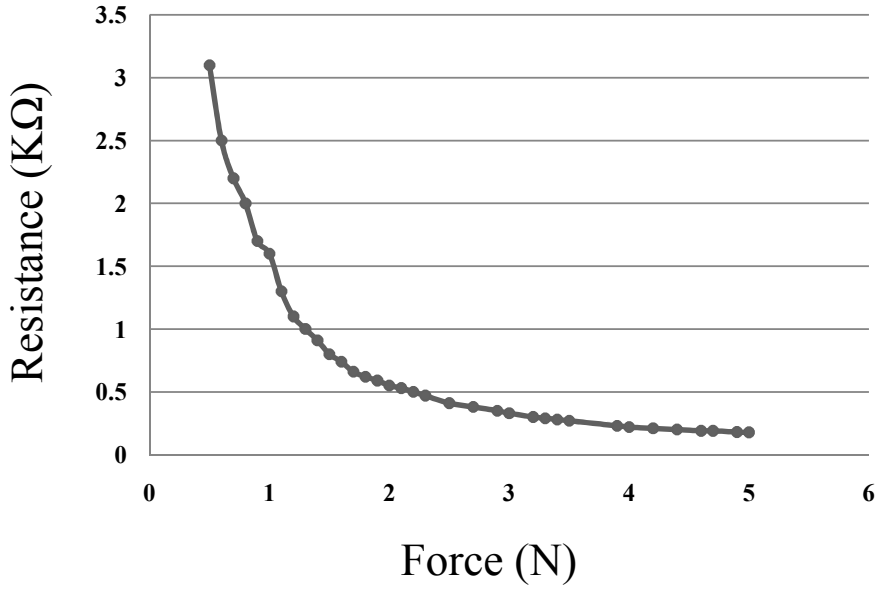

(a)

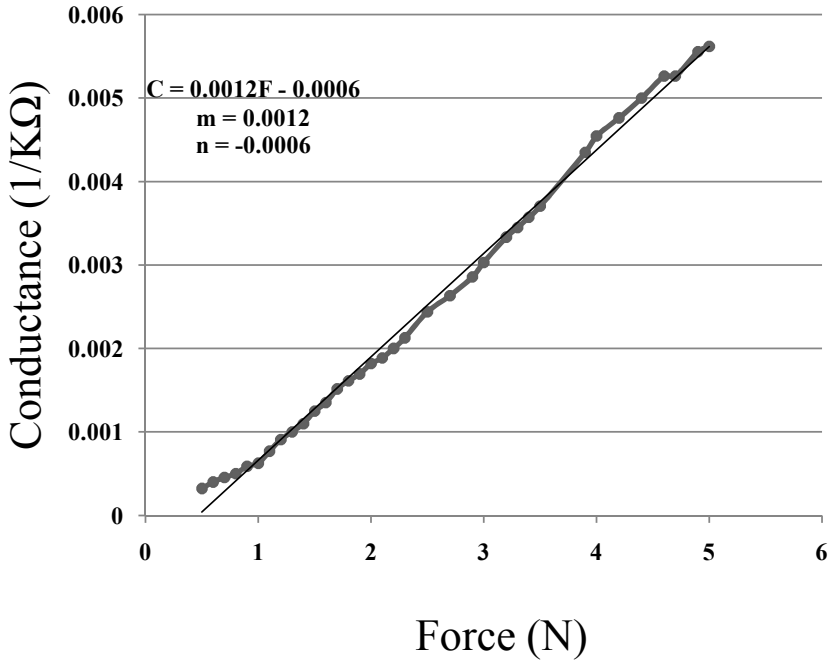

(b)

Figure 2.5: (a) Force-resistance relationship (b) Force-conductance relationship

conductance and force. In order to apply accurate normal forces to the piezoresistive force sensors during calibration, an ELECTROFORCE 3200 BOSE device was used to apply a normal force to the sensor plane. As shown in Fig. 2.4b, a simple formula can be obtained [89] for the input-output voltage relationship as

$$V_o = \frac{R}{R+r}V^+ \Rightarrow C = \frac{1}{r} = \frac{1}{(\frac{V^+}{V_o}-1)R}$$
$$\xrightarrow[Substitute]{C=mF+n} F = \frac{1}{(\frac{V^+}{V_o}-1)R.m} - \frac{n}{m} \tag{2.2.1}$$

where F is the force, C is the conductance, R is the resistance, and m and n are constants. The LabView program measures V_o for the known force applied to the sensor. Therefore, by knowing the input voltage V^+, and the connected resistance R, and by reading F and V_o from the Bose device and the LabView software, the two unknowns m and n can be found with a simple curve fitting as shown in Fig. 2.5. The force sensor was calibrated in the range of 0 to 5N which is sufficient for the intended applications. Moreover, the creep test for the sensor is also performed in this same range. Figure 2.5a shows the curve of the output of the force sensor for different applied loads. The output of the force sensor was gathered one second after application of the force at each step of the experimentation.

2.3 Tests and Discussions

As mentioned earlier, several creep tests were performed on four standard samples using the ELECTROFORCE 3200 BOSE device. Figure 2.6a shows the results for the creep tests. By using creep data, the viscoelastic coefficients in eq.(2.1.15), E_0, E_1, and μ_1 were determined for 2, 4, 6, and 8 N, respectively.

Finally, three lines were fitted to each set of coefficients using the least square method. Figure 2.6b shows the extracted coefficients from creep data, and fitted lines to each set of coefficients. By substituting the three expressions in eq.(2.1.14), the final relation between force and resistance can be extracted for Linqstat as

$$R_{total} = \frac{\rho_1 + \rho_2}{2}\sqrt{\frac{\pi H}{F}} + \left(R_0\left(\frac{F}{A}\left(\frac{e^{\left(-\frac{(449900F+397700)t}{1208200F\ +\ 2892800}\right)}-1}{449900F+397700} - \frac{1}{60900F+651200}\right)+1\right)\right) \times e^{-\frac{F}{A}\left(\frac{\gamma S_0}{60900F+651200}+\frac{1-e^{\left(-\frac{t(449900F+397700)}{1208200F+2892800}\right)}}{449900F+397700}\right)} \tag{2.3.1}$$

From this formulation, the curve for the change of resistance based on applied force can be calculated for Linqstat, eq.(2.3.1). Various properties such as volume fraction and size of impregnated carbon particles, hardness of the polymer composite, and the resistivity of the polymer composites are all required parameters for this formulation. These required data were determined using different tests. Thermogravimetric Analysis (TGA) was performed on Linqstat samples in order to find the volume fraction of carbon particles in the polymer. A specimen was cut from a Velostat sheet and

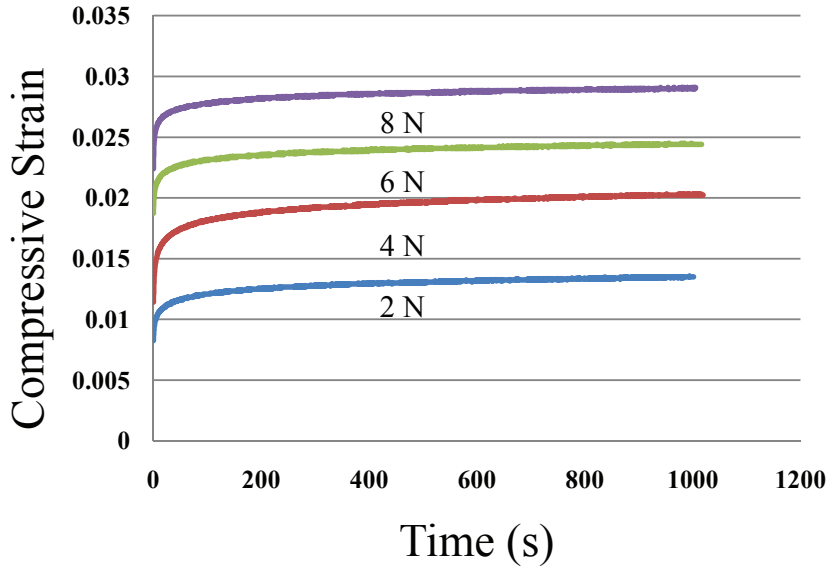

(a)

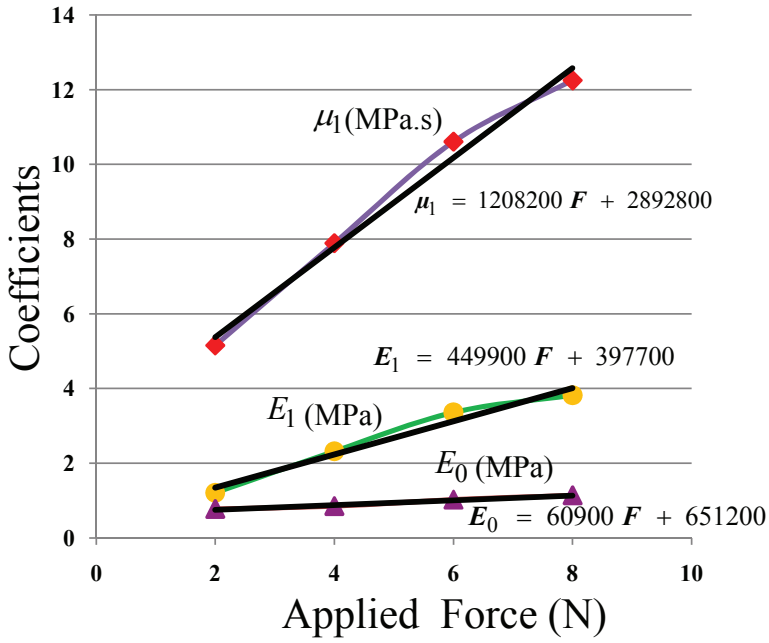

(b)

Figure 2.6: (a) Creep test result of Linqstat samples (b) Viscoelastic coefficients for Linqstat using creep data

was placed inside a platinum pan of the TGA device. The sample weight of Linqstat was $21.1580mg$. The test range was from $25°C$ to $1000°C$ with a $20°C/min$ increase in the heating rate. In some methods of thermogravimetric analysis, nitrogen gas is introduced as a purge between the temperature range of $25°C$ to $650°C$, and then the nitrogen is switched to air from $650°C$ to $1000°C$ which results in complete oxidation of residual carbon [108]. In this case, almost no ash remains at the end. However, in the current TGA analysis, nitrogen gas was only introduced to the sample in order to preserve the residual carbon, so that it could be used later as a sample for Scanning Electron Microscopy to determine the size of the carbon particles. The result showed that Linqstat contained 19.89% of carbon, and 80.11% of polyethylene with additives. So, the weight of carbon particles inside the composite was equal to $4.2083mg$, and the weight of the matrix, polyethylene, was $16.9496mg$. By considering the mass density of polyethylene as an amorphous structure having a mass density of $0.910gr/cm^3$, which is suitable for low density polyethylene, the volume of polyethylene was $0.0186cm^3$. Also, by considering the mass density of carbon black as $0.56gr/cm^3$, the volume of carbon was calculated as $0.0075cm^3$. So, the volume fraction of the carbon inside the Linqstat was $\phi = 0.2873$, which can be placed in eq.(2.1.8).

The size of impregnated filler particles inside the nonconductive polymer is another important parameter that had to be taken into account. The size of the carbon

black used in this present research was measured using Scanning Electron Microscopy (SEM). A sample of Linqstat was prepared for SEM testing by coating it with gold-palladium alloy with the thickness of $250nm$. Then, the sample was analyzed by SEM. Figure 2.7 shows the carbon particles inside the sample. Carbon particles are

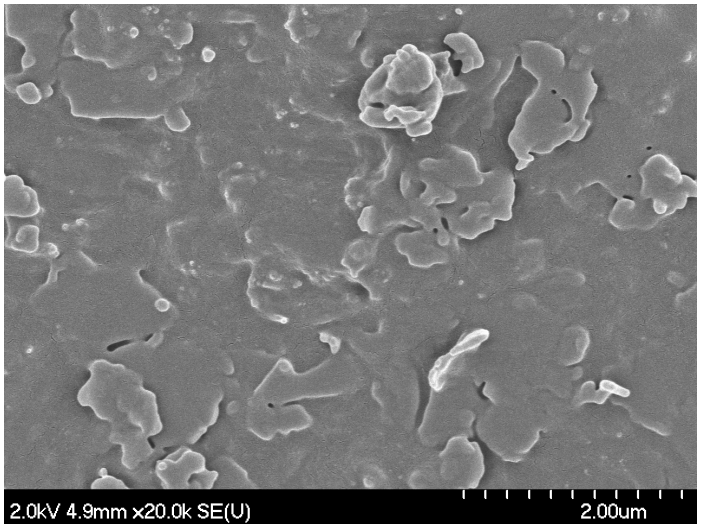

Figure 2.7: Carbon black particles inside polyethylene matrix (Linqstat)

dispersed inside the polymer like large connected colonies and it was determined that their diameter is $D = 500nm$. By having D and ϕ, the interparticle separation between two adjacent carbon particles in Linqstat can be determined from eq.(2.1.8).

As mentioned earlier, different devices were used to test the Linqstat and the force sensor. Figure 2.8 shows three of the main devices used in the current research work. The first is the ELECTROFORCE 3200 BOSE used for testing the force sensor and for testing the creep behaviour and is shown in Fig. 2.8a. The second is the TA Q50 Thermogravimetric Analyzer was used for TGA tests, and is shown in Fig. 2.8b.

The third is the Hitachi S-4700 scanning electron microscope, used to find the size of carbon particles inside the Linqstat and as shown in Fig. 2.8c.

The hardness of the Linqstat was also measured by using the Meyer hardness testing procedure. The overall mechanical and electrical properties of Linqstat together with the dimensions of the fabricated force sensor based on experimented data are presented in Table 2.1. The output of the sensor was collected one second after the application of the force during experimentation. So, by plotting the predicted output of the sensor at $t = 1s$, and plotting the experimental results for Linqstat it can be seen that the proposed formulation closely match the sensor response. Figure 2.9a compares the experimental results and the theoretical results. As can be seen from Fig. 2.9a, taking into account the contact resistance in the formulation proved to have a significant effect on the results. The net result was that the experimental data closely matched the model readings, for low resistance values. The slight difference between the computed response and experimental data are due to inaccuracies in the measurement procedures. In addition, another set of experiments was conducted to verify the improvement in the proposed model due to the inclusion of the creep behavior of Linqstat as a viscoelastic material. In this test, several constant forces with different magnitudes were applied to the force sensor. Then, the change in the resistance of the force sensor over time was recorded for each of the forces to show

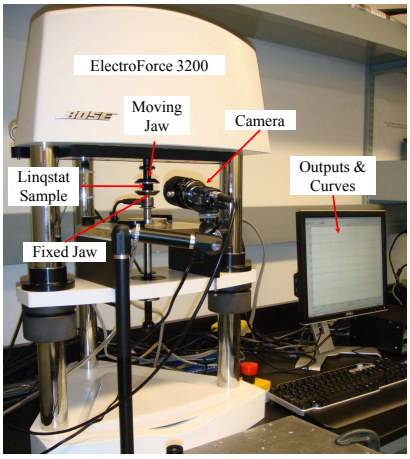

(a)

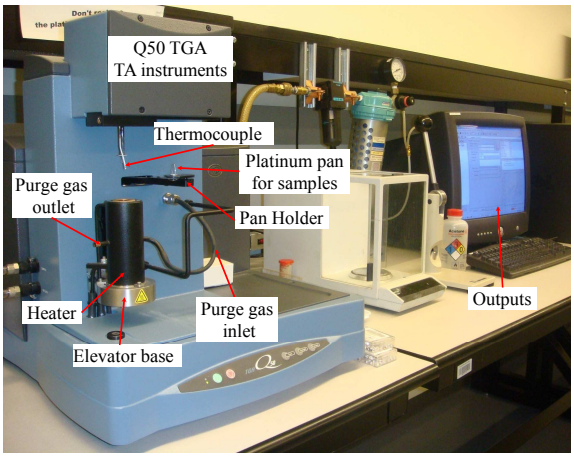

(b)

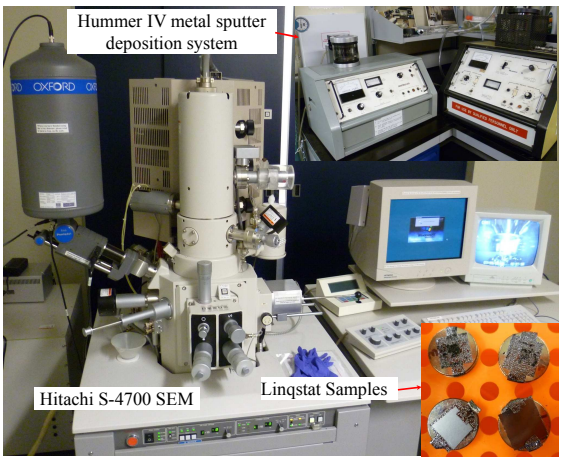

(c)

Figure 2.8: (a) ELECTROFORCE 3200 BOSE device (b) TA Q50 Thermogravimetric Analyzer (c) Hitachi S-4700 scanning electron microscopy

the creep behavior in the sensor output. The gathered data for each force were finally compared to the theoretical model prediction for that specific force as shown in Fig. 2.9b.

To include all the comparison results together, the chart was drawn in logarithmic scale for the resistance. As can be seen from the test results of the comparison in Fig. 2.9b, the model predictions closely match the experimental results of the test.

The proposed theoretical model contains three variables namely, resistance, force, and time. The relationship of these three variables is shown in Fig. 2.10 as a three dimensional surface.

The piezoresistive behaviour of other kind of semiconductive polymer composites, such as Velostat, can be predicted by the developed model. Linqstat and Velostat have some differences in the size and the volume fraction of carbon black particles, and in the type of the nonconductive polymer, resulting in different hardnesses for Velostat and Linqstat. Hence, the model can be also used for another type of semiconductive polymer composites by populating the model with appropriate parameters.

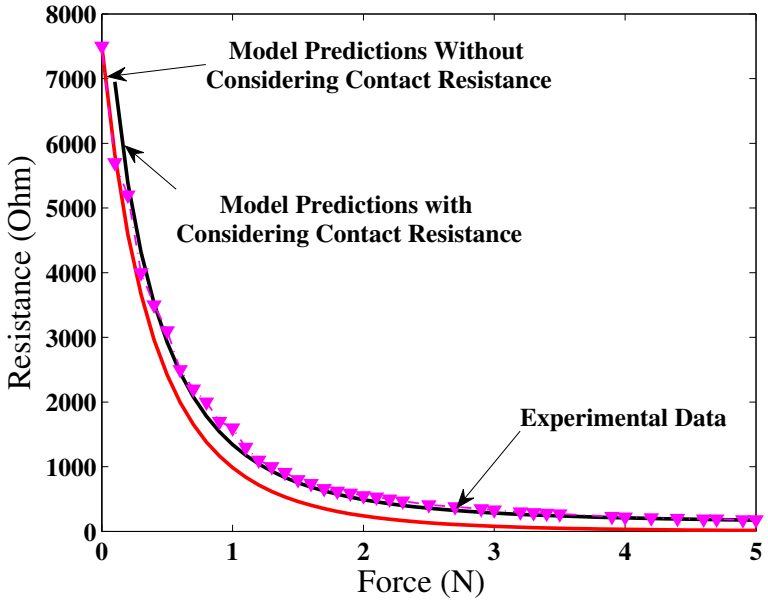

(a)

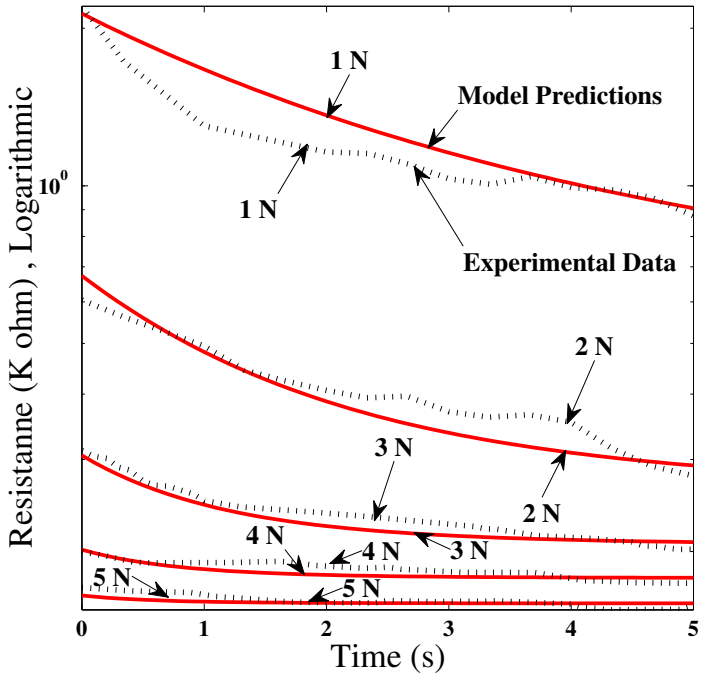

(b)

Figure 2.9: (a) Comparison of the experimental results and the theoretical results for change of resistance per applied force (b) Comparison of the experimental results and the theoretical results for change of resistance over time for different force magnitudes

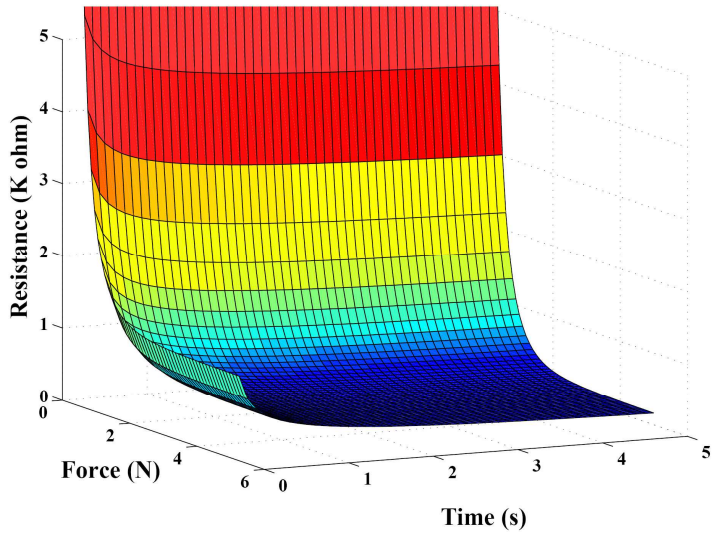

Figure 2.10: Graphical representation of the proposed model.

Chapter 3

A New Tactile Sensor for MIS and CBT

This chapter discusses the development of an innovative tactile sensor for use in both MIS and CBT. Two piezoresistive force sensors are used in the structure of the tactile sensor, which can easily be miniaturized and integrated into surgical catheters. The tactile sensor is fabricated and tested to characterize different elastomers, as the phantom of cardiac tissues. Based on a developed finite element analysis (FEA) of the elastomers, the interaction between the sensor and those materials are modelled to validate the output of the sensor. The sensor measures the difference of hardness of soft objects. This capability of the sensor helps surgeons to distinguish different types of cardiac tissues involved in mitral valve annuloplasty.

Most of tactile sensors in the literature that are developed for MIS cannot be used in CBT by virtue of their incompatible configuration. However, the developed tactile sensor has a simple and circular configuration that can be easily integrated on the tip of surgical catheters with circular shape. The proposed sensor may also be used in magnetic-resonance-guided environment by changing the piezoresistive force sensors to piezoelectric force sensors, which can be performed by using Polyvinylidene Fluoride (PVDF) sheets as the sensing elements [109,110]. However, by using PVDF material, the sensor can work only under dynamic force condition. The developed tactile sensor may also be used in some other surgical applications, such as catheter ablation. Determining tissue contact force has been shown as a determinant factor for determining lesion size during catheter ablation [37, 111]. Low contact pressure would cause a long ablation procedure, while the high contact pressure would increase the risk of tissue perforation [112].

The sensor structure, fabrication and display are described in the first section of the chapter. In the modeling and analysis section, two elastomers with different degree of softness are modelled as hyperelastic materials to verify the concept of the sensor design using FE method. Three different test setup are designed in the results section to verify the performance of the sensor, which are (1) testing with durometer; (2) testing with sensor; and (3) psychophysical test. All of the test results are compared together in the results section. The overall conclusion about the sensor

is presented in the discussion section.

3.1 Materials and Methods

3.1.1 Description of the sensor

The proposed sensing architecture consists of two circular force sensors with different diameters, and one plastic filler plate (Fig. 3.1). The inner and outer diameters of the latter are identical to the diameters of the smaller and larger force sensors, respectively, as shown in Fig. 3.1. The smaller force sensor is placed inside the hollow part of the filler plate, and over the larger force sensor, which then becomes the surface in contact with the material. Figure 3.2 shows a schematic view of a section

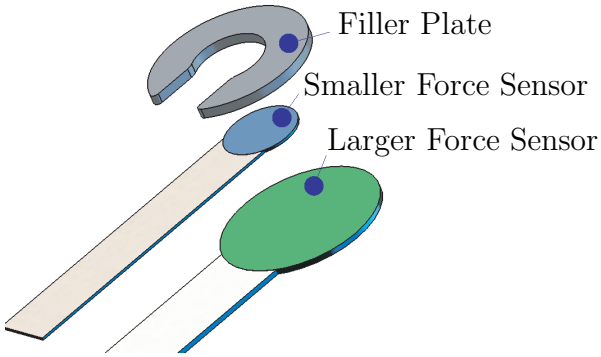

Figure 3.1: Schematic view of the sensor and the filler plate

of the tactile sensor in contact with soft material [89]. All forces, applied to the filler plate along the normal direction are recorded by the larger force sensor. A is the inner diameter of the filler plate and T_1 represents the thickness of the larger force sensor.

Similarly, T_2 and T_3 represent the thicknesses of the smaller force sensor and the filler plate. Therefore, L represents the distance the material needs to be displaced until touching the smaller sensor, which is $L = T_3 - T_2$. The $L = 0.8mm$ in the tactile sensor; this is found experimentally. The degree of the hardness of the object being

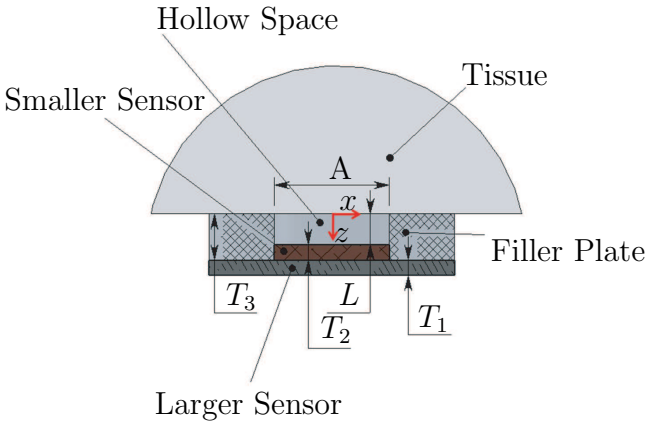

Figure 3.2: Section view of the tactile sensor

tested determines the optimal diameter of the hollow part of the filler plate and the optimal thickness of the filler plate. For instance, the ratio A/L should be larger for harder materials than for softer materials. If a material is touched by the filler plate, the force applied by the sensor onto the material is detected by the larger sensor. However, this output is not taken into account until the smaller sensor begins to send an output signal. As the surface of the material comes into contact with the filler plate, the part of the material touching the plate becomes constrained. Then, as force is progressively applied to the material, the material starts to penetrate the hollow center of the filler plate, finally reaching the smaller sensor inside. At this point, this smaller sensor begins to send an output signal. At the moment of contact between the

smaller sensor and the material, the output of the larger force sensor shows the force required for a given displacement L of that specific material. This force/pressure, which is called threshold, can be used as a the measure of material hardness. The larger the threshold force, the harder the material. In fact, the threshold force for the displacement L of the material is a measure of elastic property of materials. This elastic property is in direct relation with the hardness and in inverse relation with the softness of materials, respectively. Figure 3.3 shows two steps of applying force to a material until it reaches the smaller sensor, thus resulting in the measurement of the threshold force. When dealing with samples of different size and area during experiments, the threshold force can be converted to threshold pressure instead. From the design of the sensor it is apparent that the sensor has the limitation of sensing tissues with the thickness values larger than L. However, the value of L is very small, $L = 0.8mm$ in the proposed design, to be a noticeable limitation.

3.1.2 Sensing Principle and Fabrication

Piezoresistive force sensors are used in miniature size to prove the viability of the concept in the fabrication process due to their low thickness (less than $200\mu m$), quick response, low noise, and small size. The measuring element of the piezoresistive force sensor is semiconductive polymer composite. The performance, theoretical modeling

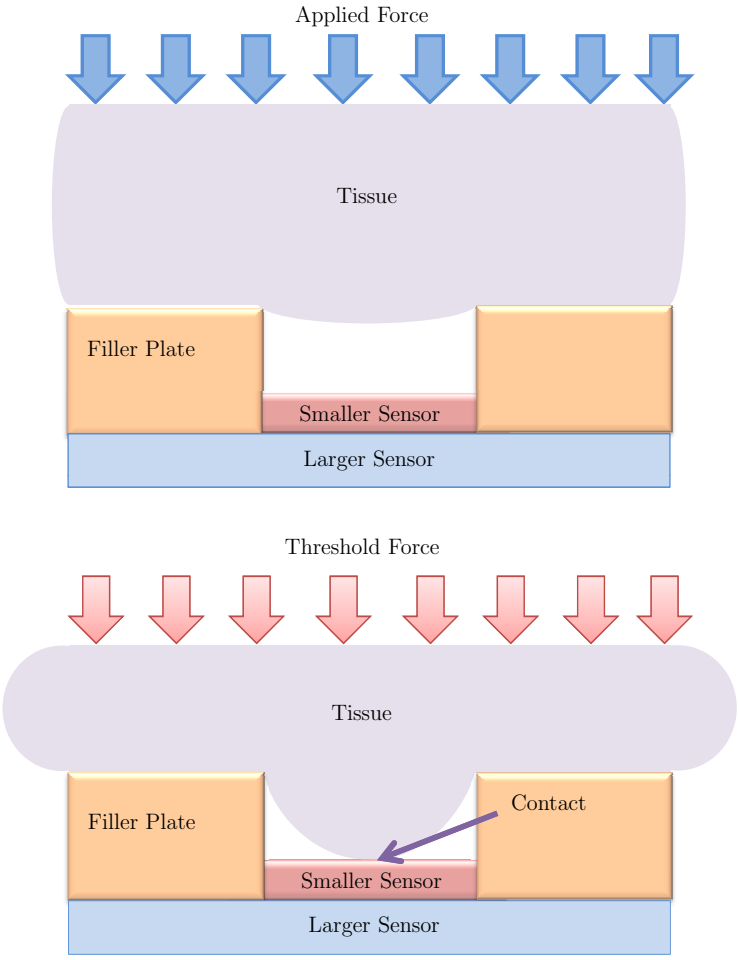

Figure 3.3: Schematic exaggerated view of measuring the threshold force

of output and the characteristics of piezoresistive force sensors based on semiconductive polymer composites is published in [87]. However, some other characteristics of the piezoresistive force sensors are addressed in the present chapter.

The output of the piezoresistive sensor is linear within the 0 to $25N$ force range, which is acceptable in MIS [4], with resolution of $\pm 0.1N$. As the displacement of the tissue is equal to $0.8mm$, it means that the sensitivity of the sensor to the stiffness is $\pm 125N/m$. In addition, the accuracy of the sensor is 2.5% of full scale with an appropriate static and dynamic response. The diameters of the large and small sensors are $6mm$ and $3mm$, respectively. Each force sensor has one input/output port which is fed by a constant supply of DC voltage of $0.5V$.

A calibration procedure was implemented for converting the voltage output of the sensor to the sensed force. Experimental data shows that the force applied to the force sensor has a linear relation with the conductance which is explained in detail in [87]. Figure 3.4 shows the output of the larger force sensors from experimental data and the linear relation of the force F with conductance C. In addition, the accuracy of the sensor is also specified in terms of the sensor linearity [113], as shown in Fig. 3.4. The least-square straight line $F = 20.94C - 0.132$ determines the nominal output of the sensor, and the accuracy is determined in terms of the linear output. As a percentage of the sensor readings, the accuracy is shown to be $+3.9\%$ and -6.15% of the full scale. To characterize the dynamic response of the piezoresistive sensor

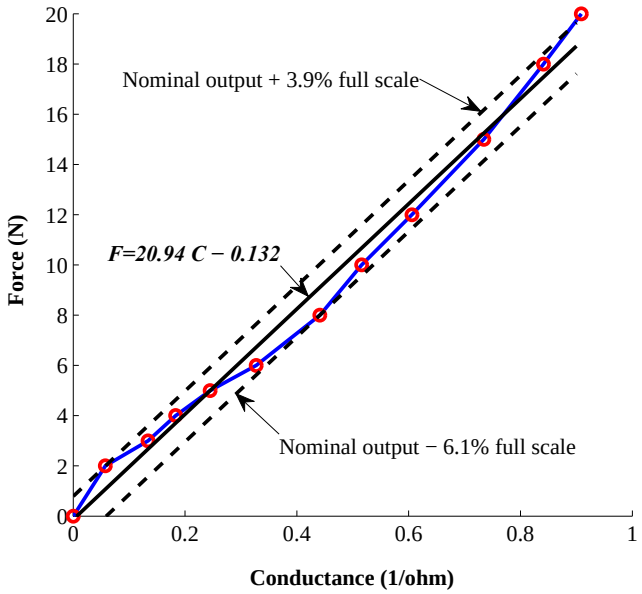

Figure 3.4: The curve of Conductance-Force for the larger force sensor, and the accuracy limits of the sensor

to applied forces, $0.1 - 2.6N$ sinusoidal force chirps from $0.2 - 2Hz$ was applied to the sensor by ElectroForce 3200 BOSE device (ElectroForce Systems Group of Bose Corporation, Minnesota, USA). Both sensors were sampled at $200Hz$. Figure 3.5a shows the output of the piezoresistive sensor plotted with the applied force from the ElectroForce device. The amplitude and the phase of both signals match together with the root mean square error value (RMS) of 0.611, indicating a good match. To test the linearity of the piezoresistive sensor for dynamic applied loads, a square force from 0.1 to $2.5N$ with $0.1N$ interval and the frequency of $1Hz$ was applied to the sensor, as shown in Fig. 3.5b. In this figure, the response of the piezoresistive sensor is plotted with the applied dynamic force. Interestingly, the filtered and unfiltered

outputs of the sensor are following each other with almost no considerable noise, as opposed to the readings from the measurement device, ElectroForce 3200 BOSE. However, using the filtered output of the sensor results in more accurate data for harmonic loads with high frequency. The low level of noise shows that the sensor has significantly large signal-to-noise ratio if being micro-fabricated. Furthermore, the output of the sensor has a good agreement with the applied force.

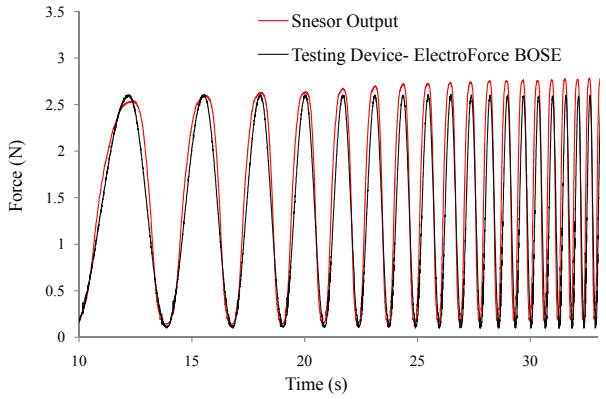

(a)

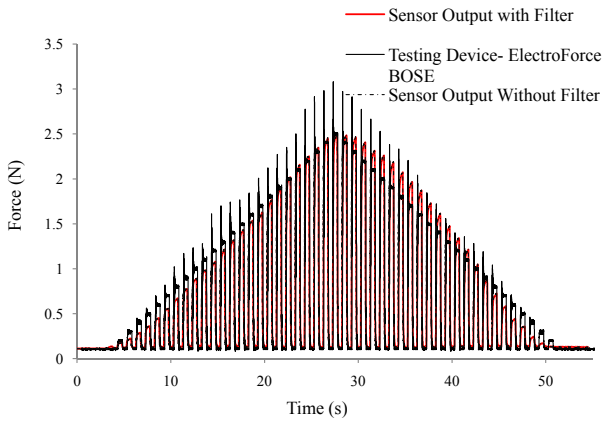

(b)

Figure 3.5: (a) Input force and response for sinusoidal chirp force to the sensor (b) Input force and response for applied dynamic square force to the sensor

A signal processing code is developed by using LabView software to analyze the output data from the two force sensors and to display the calculated threshold force. Moreover, a buffer circuit is used to reduce the loading effect of the tactile sensor on Data Acquisition (DAQ) amplifiers and to minimize the cross talk between the different input channels of the DAQ. The tactile sensor is connected to the buffer circuit which, in turn, is connected to the DAQ board, and to the developed LabView code. The processing software in the LabView environment, calculates the applied and the threshold force values according to the input voltages. At the instant when the smaller sensor is activated, the output of the larger force sensor is recorded by using the LabView code. The output of the smaller sensor triggers the recording of the output of the larger force sensor, at the threshold force.

Figure 3.6a shows the fabricated tactile sensor and the required buffer circuit in the left image; while the right image shows a miniaturized version of the tactile sensor on the tip of an annular tube, representing a catheter, which is attached to the end effector of CRS Catalysit 5 axis robot arm form Quanser Inc. Figure 3.6b shows the graphical display of the software. A first-order Butterworth low pass filter is used to filter out the $60Hz$ noise from input signal. Since the attenuation factor for the first order filter is not very high, the cut-off frequency at $10Hz$ was chosen in order to have enough attenuation for the $60Hz$ noise. If a higher-order filter was used, the cut-off frequency could be moved to $40-50Hz$. However, a higher-order filter reduces

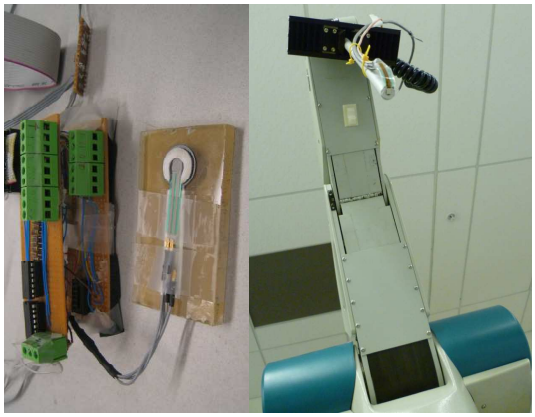

(a)

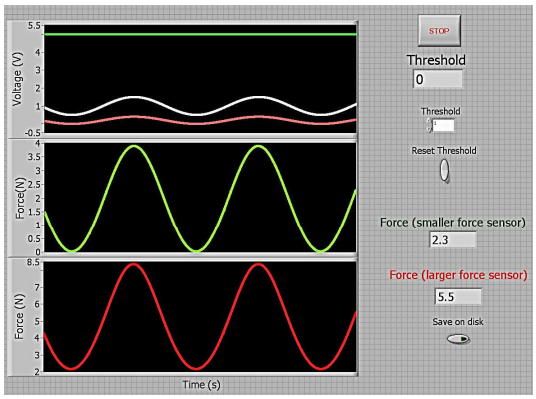

(b)

Figure 3.6: (a) Miniaturized tactile sensor on the tip of CRS Catalysit robot (b) The graphical display

the speed of the software which causes delay in detecting the threshold value, and consequently the value representing the hardness. Since the sensor is intended to be used in realtime operations, the delay in the output of the sensor is to be avoided.

To manufacture the tactile sensor, two force sensors and a filler plate are fabricated and integrated together. Each force sensor is consisted of two conductive plates, two polyester films, and a piezoresistive sensing element as shown in Fig 3.7a. The radii of the small and the large piezoresistive sensor are $1.5mm$ and $3mm$, respectively. The electrodes are covered with two layers of polyester film, or silicone tape (Fig. 3.7b). The thin layer of the polymer composite is then sandwiched between the two layers of electrode (Fig. 3.7c). The filler plate is cut from a rigid plastic plate and polished. Then, the two sensors and the filler plate are adhered together to form the tactile sensor as shown in Fig. 3.7d.

3.1.3 Modeling and Analysis

In order to model the sensor, and illustrate the difference in the hardness degree of elastomers, two elastomers are selected to be modelled. In fact, the hardness of the selected elastomers is similar to the hardness of tissues; the two elastomers were selected to represent hard and soft tissues. The stress-strain curve of the two elastomers was established by compression test, which caused a displacement of mm in both samples. The obtained stress-strain data were used to verify the concept of the tactile

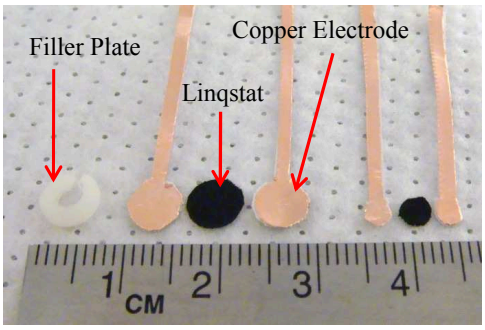

(a)

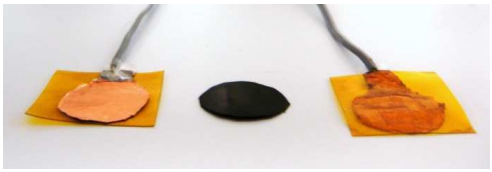

(b)

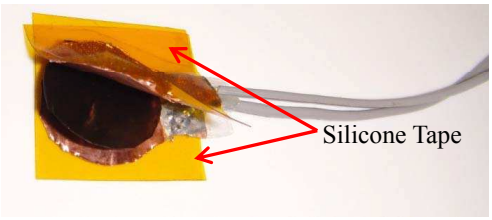

(c)

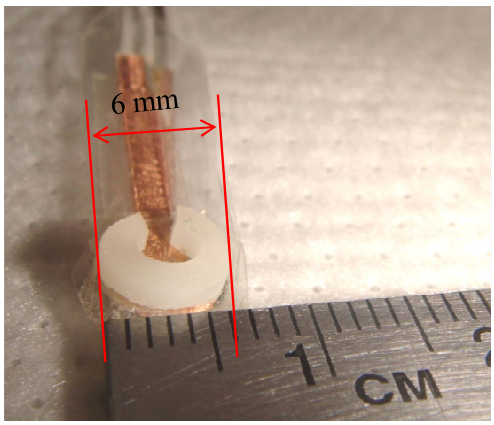

(d)

Figure 3.7: The steps of fabricating the tactile sensor

sensor design using finite element analysis (FEA). For this purpose, the interaction of the tactile sensor and the elastomers was modelled. The elastomers were considered as nearly incompressible and isotropic hyperelastic materials by virtue of their large deformation under applied force. Concepts for nonlinear stress-strain behaviour of hyperelastic materials can be found in [114–116]. In hyperelastic material, there exists the second Piola-Kirchhoff stress tensor, which is derivative of scalar strain energy function to strain components. The second Piola-Kirchhoff stress tensor relates forces in the reference configuration to area in the reference configuration, which is written as

$$\boldsymbol{S} = 2\frac{\partial W(\boldsymbol{\varepsilon})}{\partial \boldsymbol{B}} \tag{3.1.1}$$

where $W(\boldsymbol{\varepsilon})$ is the strain energy function, and $\boldsymbol{B}$ is the right Cauchy-Green deformation tensor. The second Piola-Kirchhoff stress is also related to Cauchy stress tensor $\boldsymbol{\sigma}$ by $\boldsymbol{S} = J\boldsymbol{F}^{-1} \cdot \boldsymbol{\sigma} \cdot \boldsymbol{F}^{-T}$, where $\boldsymbol{F}$ is the deformation gradient tensor and $J = det\boldsymbol{F}$. In addition, the right Cauchy-Green deformation tensor is written in terms of deformation gradient as $\boldsymbol{B} = \boldsymbol{F}^T \cdot \boldsymbol{F}$. So, by mathematical and physical manipulation, Cauchy (true) stress elements is expressed as

$$\sigma_{ij} = -p\delta_{ij} + 2\frac{\partial W(\varepsilon_{ij})}{\partial I_1}B_{ij} - 2\frac{\partial W(\varepsilon_{ij})}{\partial I_2}B_{ij}^{-1} \tag{3.1.2}$$

where p is the hydrostatic pressure, δ_{ij} is kronecker delta, I_1 and I_2 are invariants of right Cauchy-Green deformation tensor, and B_{ij} is the component of it. The hydrostatic pressure in the present research is zero. The three invariants of the $\boldsymbol{B}$

tensor are

$$I_1 = \lambda_1^2 + \lambda_2^2 + \lambda_3^2 = \mathrm{tr}(\boldsymbol{B}) \tag{3.1.3}$$

$$I_2 = (\lambda_1\lambda_2)^2 + (\lambda_2\lambda_3)^2 + (\lambda_1\lambda_3)^2 = \frac{1}{2}[I_1^2 - \mathrm{tr}(\boldsymbol{B}^2)] \tag{3.1.4}$$

$$I_3 = (\lambda_1\lambda_2\lambda_3)^2 = \det(\boldsymbol{B}) \tag{3.1.5}$$

where λ_1, λ_2, and λ_3 are the principal stretches (equal to $\lambda_i = 1 + \varepsilon_i$). For incompressible materials, it can be written that $I_3 = (\lambda_1\lambda_2\lambda_3)^2 = 1$. Mooney-Rivlin [117] proposed strain energy function W as a general polynomial in I_1 and I_2 in the form of

$$W(I_1, I_2) = \sum_{i=0}^{\infty}\sum_{j=0}^{\infty} c_{ij}(I_1 - 3)^i(I_2 - 3)^j \tag{3.1.6}$$

where c_{ij} are Mooney-Rivlin constants. The constants of c_{ij} do not have any physical meaning as they are only curve fitting parameters. It should be noted that in stress free condition, the strain energy is equal to zero. Therefore, by setting $i = 0, j = 0$, the c_{00} constant is equal to zero either. In the present paper, the elastomers were modelled with three parameter Mooney-Rivlin constants. Therefore, by setting $i = 0, j = 1$; $i = 1, j = 0$; and $i = 1, j = 1$ in eq.(3.1.6), the three terms Mooney-Rivlin equation is obtained as

$$W(I_1, I_2) = c_{10}(I_1 - 3) + c_{01}(I_2 - 3) + c_{11}(I_1 - 3)(I_2 - 3) \tag{3.1.7}$$

For the present study, the compression test was conducted on two elastomers to characterize their stress-strain curve, and the Mooney-Rivlin model for the compression

test of elastomers was used for modeling. Uniaxial compression is identical to equi-biaxial tension due to the property of the incompressibility of the elastomers. In other words, the deformation of the material does not change with adding a tensile or compressive hydrostatic stress on the incompressible hyperelastic material [118, 119]. So, for an elastomer with an isotropic material property in an unconstrained compression test, the applied stretches is considered as $\lambda_1 = \lambda_2, \lambda_3 = \lambda$. So, the deformation gradient, and the right Cauchy-Green deformation tensor are

$$\boldsymbol{F} = \begin{pmatrix} \lambda^{-1/2} & 0 & 0 \\ 0 & \lambda^{-1/2} & 0 \\ 0 & 0 & \lambda \end{pmatrix} \Rightarrow \boldsymbol{B} = \boldsymbol{F}^T \cdot \boldsymbol{F} = \begin{pmatrix} \lambda^{-1} & 0 & 0 \\ 0 & \lambda^{-1} & 0 \\ 0 & 0 & \lambda^2 \end{pmatrix} \tag{3.1.8}$$

which makes the first and the second invariant as $I_1 = \lambda^2 + 2\lambda^{-1}$ and $I_2 = 2\lambda + 2\lambda^{-2}$ while $I_3 = 1$. So, according to eq.(3.1.2), the principal stresses are shown as

$$\begin{aligned} \sigma_{33} &= -p + 2\left(\frac{\partial W(\varepsilon_{ij})}{\partial I_1}\right)\lambda^2 - 2\left(\frac{\partial W(\varepsilon_{ij})}{\partial I_2}\right)\lambda^{-2} = 2(\lambda^2 - \lambda^{-1})(c_{10} + c_{01}\lambda^{-1}) \\ \sigma_{11} &= \sigma_{22} = -p + 2\left(\frac{\partial W(\varepsilon_{ij})}{\partial I_1}\right)\lambda^{-1} - 2\left(\frac{\partial W(\varepsilon_{ij})}{\partial I_2}\right)\lambda = 0 \end{aligned} \tag{3.1.9}$$

One soft and one hard elastomers, B1-A and ICF (from PROFOM Co., Quebec, Canada), were selected to be modelled for the FE analysis. Using curve-fitting techniques, different Mooney-Rivlin models such as 2-, 3-, and 5-parameters were fitted to the obtained stress-strain curves of the elastomers, and constants were calculated. The compressive stress-strain curve for the two elastomers and the fitted Mooney-Rivlin models are shown in Fig. 3.8, from which it can be seen that the third order

Mooney-Rivlin model fits best to the experimental data for both elastomers. The normalized error norm for the three-parameter Mooney-Rivlin model for B1-A and ICF is $e_{B1-A} = 1.134$ and $e_{ICF} = 0.098$, respectively.

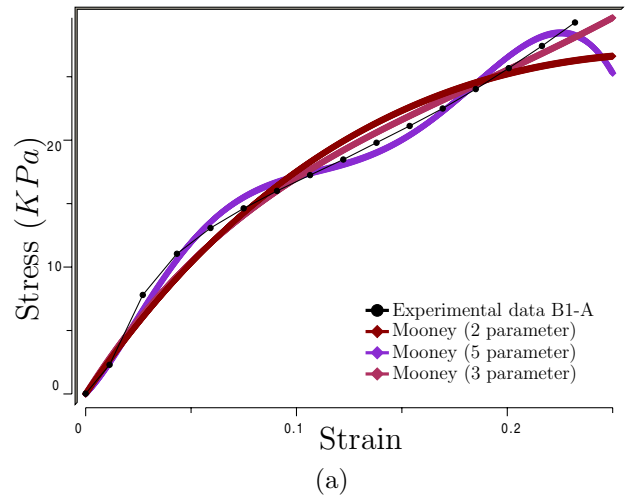

(a)

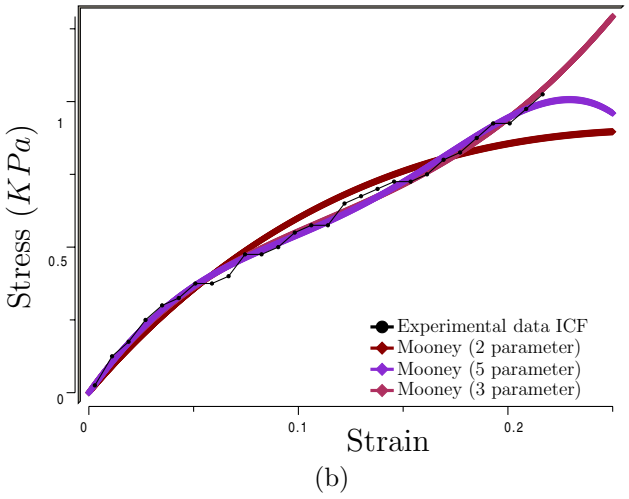

(b)

Figure 3.8: A typical fitting of Mooney-Rivlin model with 2-, 3-, and 5-parameters to the uniaxial compression data of the two elastomers (a) B1-A elastomer (b) ICF elastomer

The Mooney-Rivlin Constants for B1-A and ICF are shown in Table 3.1.

elastomers	C_{10}	C_{01}	C_{11}
B1	-129700	173670	55812
ICF	-8598.8	10284	5143.6

Table 3.1: Constants of the three parameter Mooney-Rivlin model

FE analysis was performed to validate the output of the tactile sensor for the determination of the difference in hardness of materials. The calculated constants from modeling of the two elastomers were entered as the hyperelastic material properties.

To examine the performance of the sensor, and compare it with FEA results, the sensor was experimentally tested with seven elastomers of different hardnesses, as phantom of tissues. The tactile sensor and the materials were placed between the jaws of ElectroForce 3200. A normal force was applied to the materials by device until they had a displacement of $L = 0.8mm$, reaching the inner force sensor. Since the stress-strain behaviour of the elastomers is nonlinear, a constant value of young modulus or stiffness cannot be assigned for them; and the value for the stiffness would vary in each displacement point. However, it can be written that the ratio of the measured threshold force to the length of displacement $L = 0.8mm$ is proportional to the tissue stiffness, for $0.8mm$ of displacement. To validate the results of the experiments with tactile sensor, the hardness degree of the elastomers was also tested with two other methods; (1) by a durometer; and (2) by a psychophysical test. A durometer of type OO—a standard device for hardness measurement of soft materials—was used to characterize the initial hardness of the seven elastomers according to ASTM D2240

Standard. Since the tactile sensor is designed to be mounted on a tip of a surgery catheter to play the role of the surgeon's finger, the output of the tactile sensor should be similar to that of a human. Therefore, a comparison between the outputs of the tactile sensor with the hardness feeling of humans was also performed by designing a psychophysical test. Hence, a group of 20 engineering students were selected to report their feeling of hardness of the seven elastomers. The students were asked to press the elastomers with their index finger, and report their feelings about the degree of hardness/softness of the elastomers. As the elastomers are pressed by the sensor for hardness detection, the students were asked to close their eyes, and similarly press the elastomers with their index finger without sliding finger on the elastomers. By closing their eyes, students were able to concentrate only on their tactile perception. Then, they were asked to assign a relative hardness number to elastomers, starting from one for the softest and seven for the hardest material.

3.2 Results

The elastomers and the tactile sensor were modelled in ANSYS using appropriate elements which are formulated on the basis of finite deformation theories. The tactile sensor was modelled with 2D 3-node structural solid element (PLANE 42). Also, 2D 6-node structural solid element (PLANE 183) was selected to model the hyperelastic elastomers. This element has capability of large deformation which makes

Method	Pressure for B1-A (KPa)	Pressure for ICF (KPa)
FEA	17.25	0.375
Sensor Experiments	22.28	0.4

Table 3.2: Comparison of the results for the two elastomers between the FEA and the tactile sensor outputs

it suitable for modeling nearly incompressible hyperelastic materials [120]. The 2D contact elements (TARGET 169 and SURFACE 172) were selected to model contact between tactile sensor and elastomer. The coefficient of friction between the upper surface of the tissue and the tactile sensor was set to 0.4 [121]. In addition, the lower surface of the tissue was considered to be fixed. The range of applied pressure on elastomers started from small amounts and increased until contact of elastomer and the smaller sensor. Then the applied pressure on the total area, on the larger sensor, was calculated.

Figure 3.9a and Fig. 3.9b shows FE analysis for both B1-A and ICF materials, respectively. The elastomers were constrained in FEA from the bottom, while the sensor was displaced toward the material. The outer and the inner radii of the sensor were considered equal to $3mm$ and $1.5mm$, respectively. The sensor was displaced $1.4mm$ to allow the materials reach into the hollow part by $0.8mm$ displacement. Table 3.2 compares the results of the FE analysis with the real testing outputs for the same elastomers. In this table, the recorded threshold pressure is listed for both elastomers in FE and experimental test.

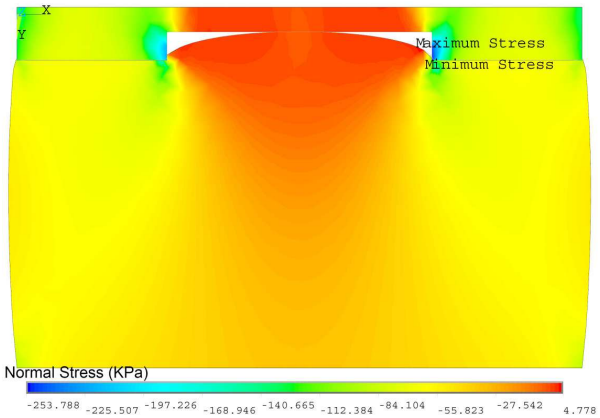

(a)

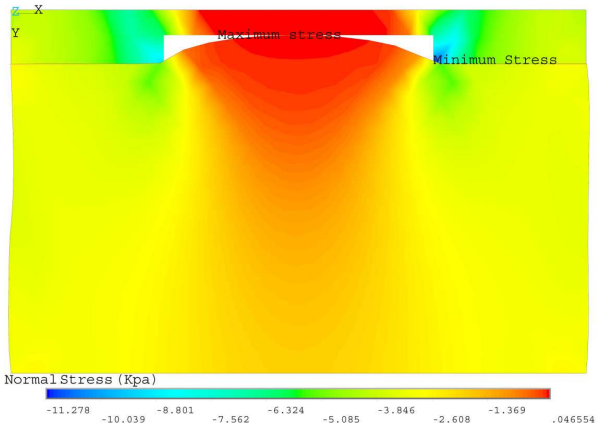

(b)

Figure 3.9: The normal stress in Y-direction for both elastomers to displace $0.8mm$ and reach the smaller sensor (a) Normal stress for B1-A elastomeric material (b) Normal stress for ICF elastomeric material

From Table 3.2, it can be seen that the required pressure value by B1-A material to reach the inner surface of the smaller sensor is much greater than that for the ICF material in both experimental and FEA tests. The difference between results of FEA and experimental test can be attributed to few parameters. Considering elastomers as incompressible can introduce inaccuracy since the elastomers are not completely incompressible. In addition, the resolution and the drift of the force sensor cause some inaccuracies for the data extracted from the experimental test.

Figure 3.10 shows the result for the psychophysical test of the seven elastomers by 20 engineering students. The results show that students have different feeling about materials with similar degree of hardness, such as H1-N, B1, and EVA elastomers. Table 3.3 shows the comparison between results of the sensor, the durometer, and the psychophysical test. The elastomers in this table are arranged in accordance to their decreasing hardness/increasing softness from left to right. In order to have a feeling of the hardness of elastomers indicated in shore scale and their relation with the hardness of tissues, the hardness of a porcine atrial tissue was measured, which was 25 shore type OO.

As shown in Table 3.3, the relative hardness of the elastomers that are established by the tactile sensor agrees to the relative hardness established by the standard durometer, and the group of the 20 people.

The results of Table 3.3 shows that for a relatively small increase in the measured

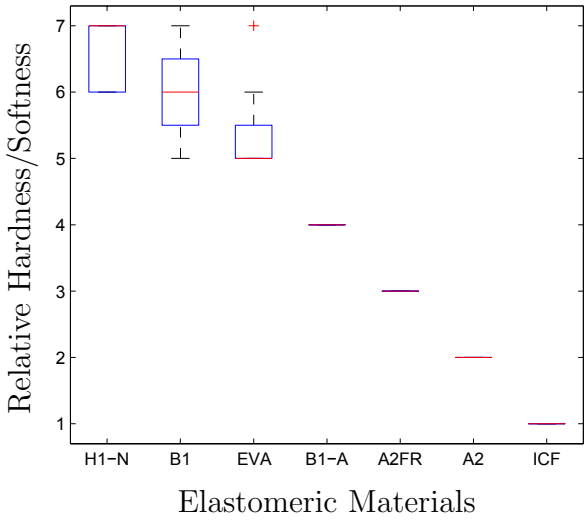

Figure 3.10: Comparison of the hardness feeling of 20 people on the seven elastomeric materials

Elastomeric Materials	H1-N	B1	EVA	B1-A	A2FR	A2	ICF
Hardness (Shore OO)	48	45	42	36	13	4	1
Psychophysical test	7	6	5	4	3	2	1
Threshold Pressure (KPa) by Sensor	89.8	52.0	39.3	22.3	2.8	0.9	0.4

Table 3.3: Comparing the results for the hardness measurement of the elastomers

hardness from B1 to H1-N, from 45 to 48 Shore OO, the threshold pressure by the tactile sensor shows a large increase, from 52 to 89.8Kpa. The reason for this difference is due to the metallurgical structure of the two elastomers. B1 elastomer has a homogeneous structure, while the H1-N elastomer has a nonhomogeneous structure with a relatively compressed and dense material near its surface. Therefore in the test with a durometer, the major part of the deformation of H1-N occurs in the middle area of the elastomer which is softer in comparison to its surface. However, by virtue of the design of the tactile sensor, the hard surface of the H1-N elastomer is deformed during the measurement. Hence, the records of the sensor output show a higher change in the threshold pressure. The tests result of Table 3.3 can be also used in calculating the required force to be applied by a surgical catheter to cause sufficient tissue deformation for hardness measurement by the sensor. The outer and the inner radii of the tactile sensor in Fig. 3.7d are 3mm and 1.5mm, respectively. Hence, the required force for the hardness detection by this sensor would fall in the range of 0.01N to 1.9N for the softest to the hardest tissue. This range can be easily tuned by changing the contact area of the sensor with tissue, which can be achieved by changing the ratio of the inner to the outer radii of the tactile sensor, and by changing the thickness of the filler plate. In other word, by changing the ratio of A/L, in Fig. 3.2, the range of required force to be applied to the tissue can be tuned. Therefore, the range of required force can be adjusted for each catheter to fall within

the limits of the catheter for applying force.

Chapter 4

Viscoelastic Modeling of the Contact Interaction of the Tactile Sensor

Modeling and parameter identification of soft tissue are essential in establishing an accurate contact model for tool-tissue interaction, which can be used in the development of high-fidelity surgical instruments. This chapter discusses the interaction between tissue and the developed tactile sensor in minimally invasive surgery, the focus being a novel technique for robotic-assisted mitral valve repair, in which tactile sensors are used to distinguish between different kinds of tissue by their relative softness. A discrete viscoelastic model is selected to represent the tissue behaviour. To

populate the model of the tissue with actual data, a set of tissue-testing experiments is designed and implemented on the atrial tissue of a swine heart by analyzing its dynamic response. By means of a genetic algorithm, data of the complex compliance are extracted and used to find the coefficients of the model. Further, a viscoelastic contact model is developed to model the interaction between tissue and the tactile sensor with annular shape. Finally, the relation among the indentation displacement, the ratio of the radii, and the applied force are established parametrically.

Recently, a number of heart interventions have been conducted by means of robotic-assisted surgery (RAS). In current robotic-surgery systems, surgeons face problems such as lack of tactile and haptic feedback during the operation. To treat MR with RAS, the surgeon needs tactile feedback from the patient organ. Integrating a tactile sensor into the tip of surgical tools can provide tactile feedback from interaction between surgical instrument and tissue during surgery. In this case, a computer-controlled catheter can conduct the operation while the heart is beating and the blood is flowing [8]. The surgeon moves the catheter through the femoral vein to the inside of the heart. Although the computer-controlled catheter is equipped with different mapping systems such as 3D ultrasound imaging systems, the recognition of the mitral annulus from the surrounding tissue is limited, without having tactile feedback from inside the heart [122]. The reason here is that the localization of the moving annulus—while the heart is beating and blood is flowing—needs more

advanced techniques than those that are currently available. Consequently, to localize the mitral annulus, it would be advantageous to have access to tactile sensing during the operation.

This chapter discusses the identification of viscoelastic properties of heart tissue in contact with a tactile sensor, currently under design for minimally invasive surgery applications [88], with focus on MR repair by RAS [8]. The tactile sensor is fabricated at the tip of a surgical catheter; it distinguishes different kinds of tissue by their relative softness or hardness for that matter. A parametric model for annular viscoelastic contact of the tactile sensor and the atrial heart tissue is developed to investigate the tool-tissue interaction and to optimize the design of the sensor. According to the annular geometry of the sensor, some simplifications are made in the analysis: the tissue is modelled as a viscoelastic half-space; the sensor is rigid; and the interface between tissue and sensor is frictionless. Under these assumptions, the contact problem falls into the *complete* category. The model includes the indentation depth of the tissue into the hollow space of the tactile sensor in terms of the applied force, the inner and outer radii of the tactile sensor, and time. The contact model can be used to simulate the behaviour of the tissue being touched by the sensor. In addition, the model can be used to optimize the design of tactile sensors and catheters with annular shape. Furthermore, as the model is parametric, it can simulate the tool-tissue interaction for surgical training systems in real-time applications.

The tactile sensor structure is described briefly in Section 4.1. After describing the contact problem in Section 4.2.1, the solution of the contact problem is elaborated in elasticity in Section 4.2.2. The viscoelastic behaviour of the tissue is modelled in Section 4.3. DMA experiments are outlined in Section 4.4, while the actual data from experiments are used in a parameter identification process, employing a genetic algorithm, to obtain the model parameters in Section 4.5. The solution of the viscoelastic contact model of the tissue and the tactile sensor is implemented in Section 4.6.

4.1 Sensor Structure

The proposed sensing architecture consists of two circular force sensors with different diameters, and one plastic filler plate (Fig. 3.1). The inner and outer diameters of the latter are identical to the diameters of the smaller and larger force sensors, respectively, as shown in Fig. 3.1. The sensor design and development procedure is explained in details in Chapter 3. Figure 4.1 shows a schematic view of a section of the tactile sensor in contact with soft material in Cartesian coordinates (x, y, z) [89]. The tactile sensor is axisymmetric with respect to the z-axis. The origin of the coordinate system is denoted by O, the y-axis not being shown, as it is normal to the xz plane in Fig. 4.1. All forces applied to the filler plate along the normal direction are recorded by the larger force sensor.

Figure 4.2 shows the difference in the design of the sensor for two groups of

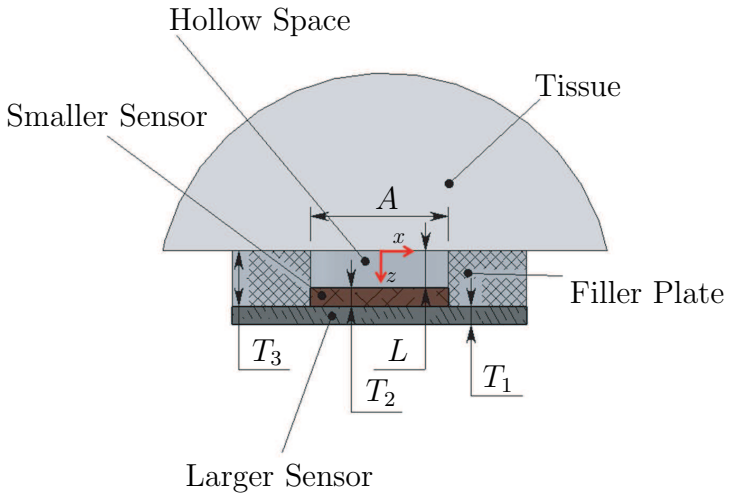

Figure 4.1: CAD model of the tactile sensor

materials with different levels of hardness. For example, the length L distance should be higher for soft materials. In this case, it would be easier to distinguish the difference between recorded forces of soft materials, and compare their hardness.

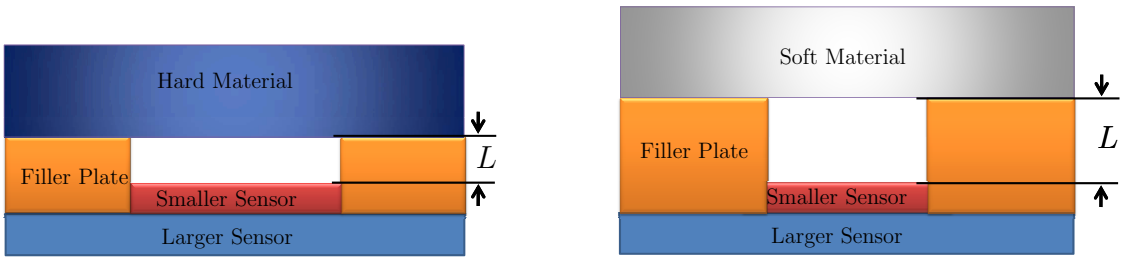

Figure 4.2: Section view of the tactile sensor in contact with (a) a hard and (b) a soft material

4.2 The Elastic Boundary-value Problem

As shown in Fig. 4.1, the contact model can be formulated as a boundary-value problem, with the boundary conditions defined piecewise: (1) the exterior of the large sensor radius; (2) the interior of the small sensor radius; and (3) the contact area. This problem is called the *three-part boundary-value problem*. The boundary-value problem thus arising, in the realm of linear elasticity, is formulated and solved in this section. A few researchers have discussed the three-part boundary-value problem in elasticity since the 1960s, [71, 123]. Many methods were used in an attempt to solve the problem, each with its own merits and demerits; however, none of them led to a closed-form solution. A combination-of-harmonics method is used in the present chapter for solving the problem at hand. The flowchart in Fig. 4.3 shows the detailed steps toward solving the contact problem for the three-part boundary-value problem at hand.

4.2.1 Problem Formulation

By defining the variable $r = \sqrt{x^2 + y^2}$, the boundary conditions for the contact between the sensor and the tissue can be represented in Cartesian coordinates depicted

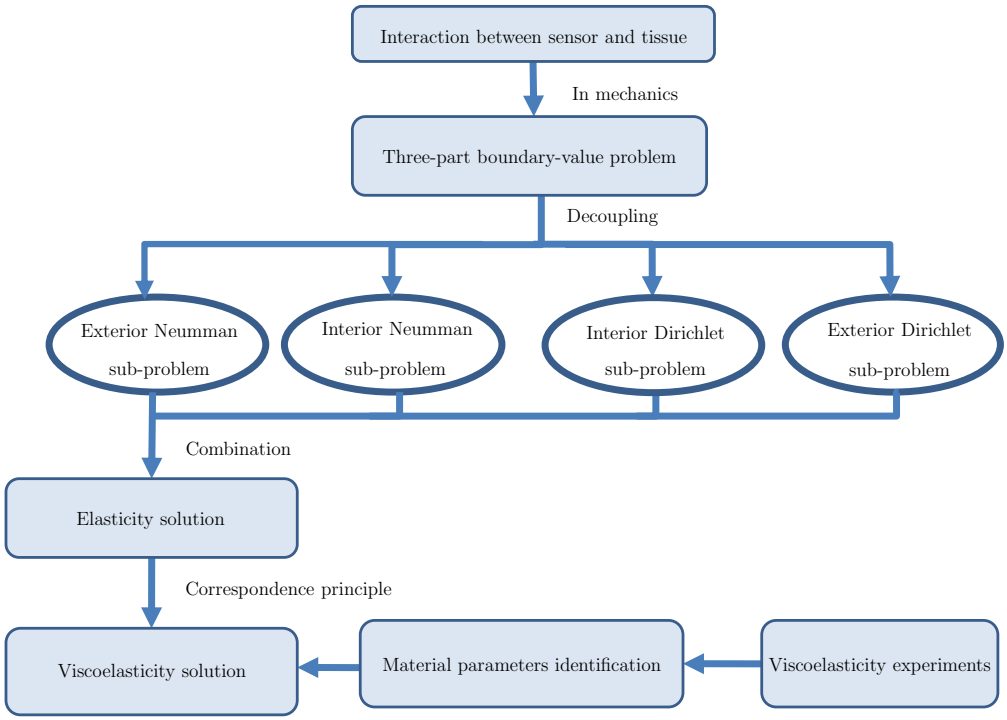

Figure 4.3: The step-by-step flowchart for solving the three-part boundary-value problem

in Fig. 4.1 as,

$$\sigma_{zz}(x,y,0) = 0, \qquad 0 \le r \le r_i, r_o \le r \tag{4.2.1}$$

$$u_z(x,y,0) = \epsilon_0, \qquad r_i \le r \le r_o \tag{4.2.2}$$

$$\sigma_{xz}(x,y,0) = \sigma_{yz}(x,y,0) = 0, \qquad 0 \le r \tag{4.2.3}$$

where ϵ_0 is the sensor displacement, σ_{zz} is the normal stress of the tissue in the z direction, u_z is the tissue displacement in the z direction, σ_{xz} and σ_{yz} are the shear stresses of the tissue in the xy plane, r_i and r_o being the inner and outer radii of the annular contact area, respectively. In addition, the tissue is considered as a half space. For three-dimensional problems in the absence of body forces, a useful result is the Papkovich-Neuber solution [124],

$$2G\boldsymbol{u} = -4(1-\nu)\boldsymbol{\psi} + \boldsymbol{\nabla}(\boldsymbol{r}\cdot\boldsymbol{\psi} + \phi) \tag{4.2.4}$$

where ν is the Poisson ratio and G is the shear modulus of the tissue, while $\boldsymbol{\psi}$ and ϕ are harmonic functions. Only appropriate harmonic functions $\boldsymbol{\psi}$ and ϕ are needed to satisfy the specified boundary conditions. For axisymmetric contact problems, two particular Papkovich-Neuber solutions were developed by Green and Zerna [125]. The first one considers $\Delta\phi = 0$ and $\Delta\boldsymbol{\psi} = \mathbf{0}$, where Δ is the harmonic operator. The second one considers $\phi = 0$, $\Delta\boldsymbol{\psi} = \alpha[0 \quad 0 \quad 1]^T$ and $\Delta\alpha = 0$. If the harmonic functions α and ϕ satisfy the relationships

$$\phi = (1-2\nu)\varphi, \quad \alpha = \frac{\partial\varphi}{\partial z}, \quad \Delta\varphi = 0 \tag{4.2.5}$$

where φ is an arbitrary harmonic function, the sum of α and ϕ will produce the deformed state below:

$$2Gu_z = 2(1-\nu)\frac{\partial \varphi}{\partial z} - z\frac{\partial^2 \varphi}{\partial z^2} \tag{4.2.6}$$

$$\sigma_{zz} = -\frac{\partial^2 \varphi}{\partial z^2} - z\frac{\partial^3 \varphi}{\partial z^3}, \quad \sigma_{xz} = z\frac{\partial^3 \varphi}{\partial x \partial z^2}, \quad \sigma_{yz} = z\frac{\partial^3 \varphi}{\partial x \partial z^2} \tag{4.2.7}$$

From eq.(4.2.7), it is apparent that σ_{xz} and σ_{yz} are zero for $z = 0$. Hence, the frictionless condition, expressed in eq.(4.2.3) at the contact area is satisfied. In order to satisfy the boundary condition (4.2.1), the harmonic function α, through eqs.(4.2.5) and (4.2.7), must satisfy

$$-\frac{\partial^2 \varphi}{\partial z^2} = -\frac{\partial \alpha}{\partial z} = 0 \qquad 0 \le r \le r_i, r_o \le r \tag{4.2.8}$$

Similarly, for the boundary condition (4.2.2), the harmonic function α, through eqs.(4.2.5) and (4.2.6), must satisfy

$$2(1-\nu)\frac{\partial \varphi}{\partial z} = 2(1-\nu)\alpha = 2G\epsilon_0 \qquad r_i \le r \le r_o \tag{4.2.9}$$

These equations show the relation between α and ϵ_0. Since α in eqs.(4.2.8) and (4.2.9) satisfies the boundary conditions, an appropriate value for α is sought in the next Sections.

4.2.2 Combination-of-harmonics Method

Oblate spheroidal coordinates forms 3D orthogonal coordinate system. These coordinates result from rotating a 2D elliptic coordinate system about the non-focal

axis of the ellipses [126]. In this section, spheroid coordinates are used to solve the boundary-value problem at hand.

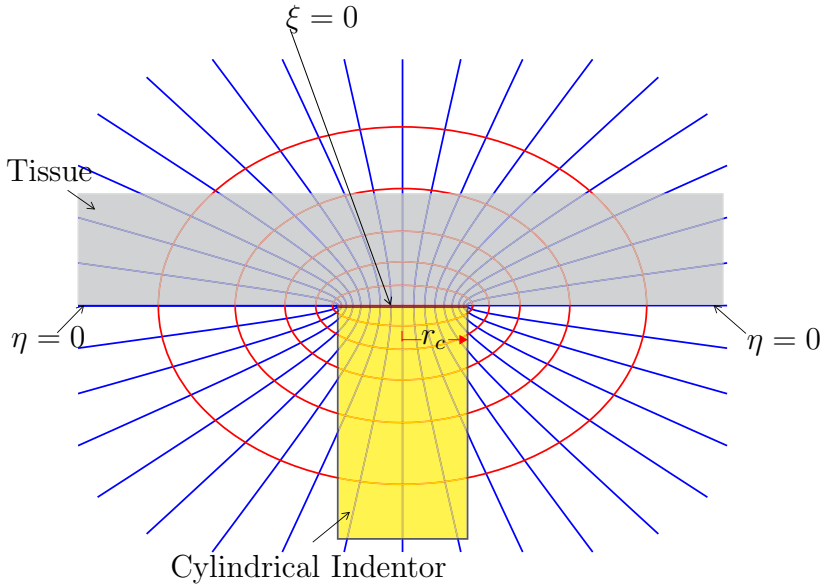

Figure 4.4: The cylindrical indentor in the oblate coordinate system

First, a piecewise-boundary value problem is considered in the oblate spheroidal coordinate system (ξ, η, θ), as shown in Fig. 4.4. The relation between the spheroidal coordinates (ξ, η, θ) and the Cartesian coordinates (x, y, z) is recalled:

$$r = \sqrt{x^2 + y^2} = r_c\sqrt{(1+\xi^2)(1-\eta^2)}, \quad z = r_c\xi\eta \tag{4.2.10}$$

where r_c is the contact radius, $-1 \leq \eta \leq 1$ and $\xi \geq 0$. From eq.(4.2.10), the surfaces $\xi = 0$ and $\eta = 0$ are, respectively, the interior and exterior of the circle $r = r_s$, $z = 0$. Obviously, ξ and η are also functions of the Cartesian coordinates (x, y, z). The stress and the strain at infinity within the tissue region are assumed to be negligibly

small. This assumption requires that the harmonic function α be finite at infinity. Additionally, in accordance with the cylindrical symmetry of the sensor, α is also cylindrically symmetric. With the symmetry of the harmonics, the general harmonic function α in spheroidal coordinates can be expressed as [127]

$$\alpha = \varrho P_n^m(\eta) Q_n^m(i\xi) \tag{4.2.11}$$

where ϱ is an arbitrary constant, and i is the imaginary unit. Also, P_n^m and Q_n^m are Legendre polynomials of the first and the second kind, respectively. After expressing α in Cartesian coordinates (x, y, z), for the piecewise boundary-value problem, four types of problems, interior Dirichlet, interior Neumann, exterior Dirichlet, and exterior Neumann, are orderly classified as

$$\alpha(x,y,0) = \varsigma_1 \qquad 0 \le r \le r_c \quad ; \quad \frac{\partial \alpha}{\partial z}(x,y,0) = 0 \qquad r_c < r \tag{4.2.12}$$

$$\frac{\partial \alpha}{\partial z}(x,y,0) = \varsigma_2 \qquad 0 \le r \le r_c \quad ; \quad \alpha(x,y,0) = 0 \qquad r_c < r \tag{4.2.13}$$

$$\frac{\partial \alpha}{\partial z}(x,y,0) = 0 \qquad 0 \le r \le r_c \quad ; \quad \alpha(x,y,0) = \varsigma_3 \qquad r_c < r \tag{4.2.14}$$

$$\alpha(x,y,0) = 0 \qquad 0 \le r \le r_c \quad ; \quad \frac{\partial \alpha}{\partial z}(x,y,0) = \varsigma_4 \qquad r_c < r \tag{4.2.15}$$

where ς_1, ς_2, ς_3 and ς_4—ς is to be read "varsigma"—are prescribed functions of x and y. Figure 4.4 refers to the interior Dirichlet problem.

From the properties of the Legendre polynomial, Gladwell [128] gave the solutions to the four problems. If the scripts m and n are of the same parity, eq.(4.2.11) is the solution for the interior Dirichlet problem, and ς_1 is a polynomial of degree n in

r. When m and n are of opposite parity, eq.(4.2.11) is the solution to the interior Neumann problem. For the exterior Dirichlet problem, the solution is

$$\alpha = (1+\xi^2-\eta^2)^{-\frac{1}{2}} P_n^m[\xi(1+\xi^2-\eta^2)^{-\frac{1}{2}}] Q_n^m[i\eta(1+\xi^2-\eta^2)^{-\frac{1}{2}}] \tag{4.2.16}$$

where m and n are of the same parity, and ς_3 is a polynomial of degree $n+2$ in r^{-1}. If m and n are of the opposite parity, eq.(4.2.16) becomes the solution to the exterior Neumann problem. With respect to the axisymmetric contact problem, the superscript m of the Legendre polynomial is assumed to be 0 [129]. The boundary conditions of the contact between sensor and tissue cannot be defined as the Dirichlet or Neumann problem, since the shape of the sensor is similar to an annular indentor. Therefore, a combination of four Dirichlet and Neumann boundary problems, eqs.(4.2.12–4.2.15), is used to define the contact between sensor and tissue.

For the boundary-value problem, eqs.(4.2.10) are used to establish the oblate spheroidal coordinate systems $(\xi_1, \eta_1, \theta_1)$ shown in Fig. 4.5a, by replacing r_c with r_o. In the said coordinate system, the solution α_{1iD} of the interior Dirichlet problem and the solution α_{1eN} of the exterior Neumann problem can be obtained.

Similarly, the oblate spheroidal coordinate system $(\xi_2, \eta_2, \theta_2)$, shown in Fig. 4.5b, can be established by replacing r_c with r_i. In the latter, the solution α_{2eD} of the exterior Dirichlet problem and the solution α_{2iN} of the interior Neumann problem can be obtained. After transforming α_{1iD} and α_{2eD} into cylindrical coordinates, one

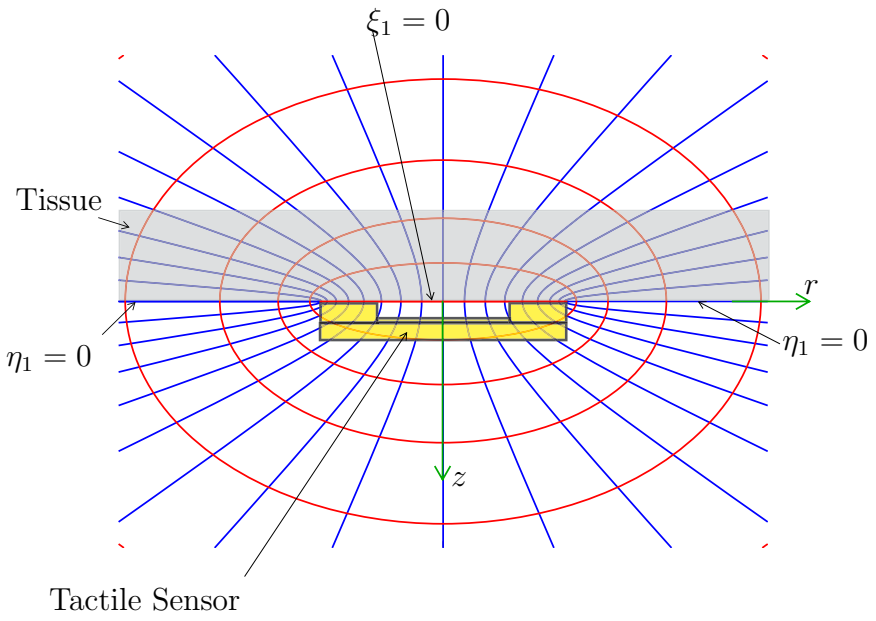

(a)

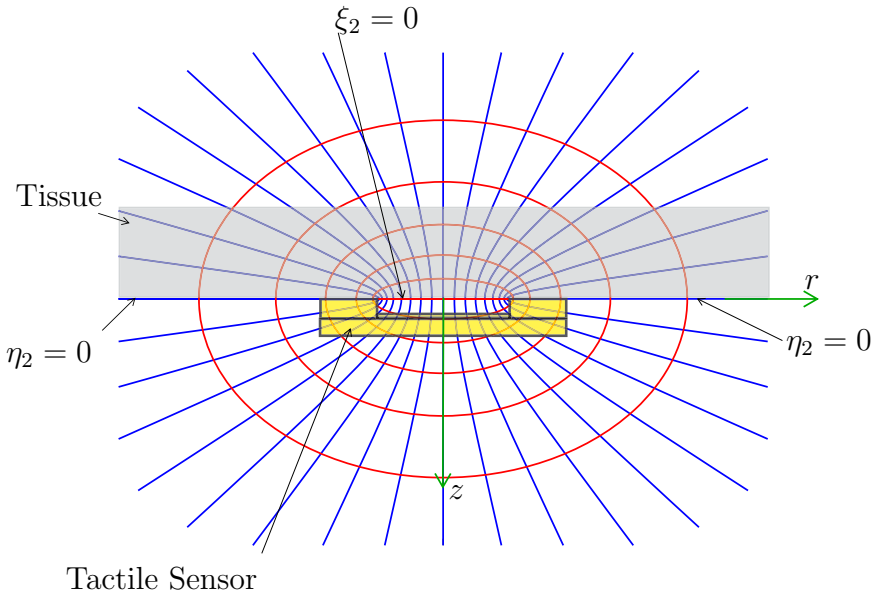

(b)

Figure 4.5: Oblate coordinate system for (a) Oblate coordinate system for outer radius and (b) Oblate coordinate system for inner radius

part of the harmonic function α, which is named α_1, is written as

$$\alpha_1 = \alpha_{1iD} + \alpha_{2eD} \tag{4.2.17}$$

From eqs.(4.2.12) and (4.2.14), if

$$\varsigma_{1iD} + \varsigma_{2eD} = \frac{2G\epsilon_0}{1-\nu} \tag{4.2.18}$$

where ς_{1iD} is a prescribed function related to α_{1iD}, while ς_{2eD} is related to α_{2eD}, then α_1 is a harmonic function that satisfies eq.(4.2.9).

Further, α_{1eN} and α_{2iN} are expressed in Cartesian coordinates. By considering eqs.(4.2.13) and (4.2.15), the sum $\alpha_{1eN}+\alpha_{2iN}+\alpha_1$ is found to be also a function that satisfies eq.(4.2.9). Additionally, the stress condition in eq.(4.2.8) can be satisfied by adjusting the coefficients ϱ in α_{1eN} and α_{2iN} to obtain

$$\frac{\partial(\alpha_{1eN}+\alpha_{2iN}+\alpha_{1iN})}{\partial z} = 0, \quad \frac{\partial(\alpha_{2iN}+\alpha_{2eN})}{\partial z} = 0 \tag{4.2.19}$$

Thus,

$$\alpha \;\; = \;\; \alpha_{1eN} + \alpha_{2iN} + \alpha_{1iD} + \alpha_{2eD} \tag{4.2.20}$$

For the flat annular elastic contact problem in our case, an approximate result that relates the applied force p and the indentation displacement ϵ_0 is obtained as

$$\frac{(1-\nu)p}{4Gr_o\epsilon_0} = 1 - \frac{4\beta^3}{3\pi^2} - \frac{\beta^4}{8}, \quad \beta = \frac{r_i}{r_o} \tag{4.2.21}$$

where p is the total load on the sensor, and β is the ratio of the inner to the outer radius. Equations (4.2.21) will be extended to include viscoelasticity in Section 4.6.

4.3 A Viscoelastic Model of Tissue

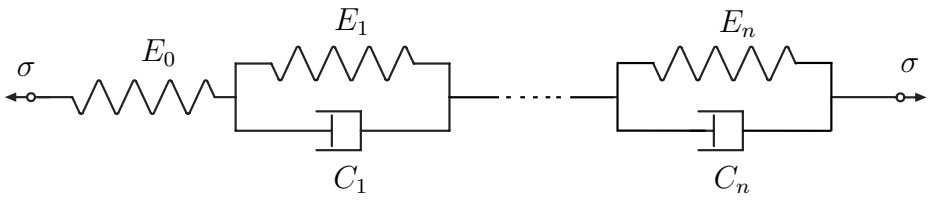

Figure 4.6: The generalized Kelvin model

To model the viscoelastic behaviour of the heart tissue, the generalized Kelvin model is selected, as shown in Fig. 4.6 [130]. By writing the related equations for the spring and dashpot elements, the constitutive equation for the generalized Kelvin model with one Kelvin unit is derived as [70, 103]

$$\boldsymbol{\Sigma} + \frac{C_1}{E_0 + E_1}\dot{\boldsymbol{\Sigma}} = \frac{E_0 E_1}{E_0 + E_1}\boldsymbol{E} + \frac{C_1 E_0}{E_0 + E_1}\dot{\boldsymbol{E}} \tag{4.3.1}$$

where E_0 is the instant elastic modulus at the start of excitation, E_1 is the elastic modulus in the Kelvin unit, C_1 is its viscous counterpart, while $\boldsymbol{\Sigma}$ and $\boldsymbol{E}$ are the stress and strain tensors applied on the generalized Kelvin model, respectively. E_0 and E_1 contribute for the elastic modulus in the equilibrium of the generalized Kelvin model. The complex modulus and compliance can be calculated from the response of the material to sinusoidal stress and strain inputs. By expressing the stress and strain in exponential form, and by substituting them into the constitutive equation (4.3.1), the expression for complex modulus or compliance is derived. The exponential form

of strain and stress can be written, respectively, as

$$\boldsymbol{E}(\omega) = \boldsymbol{E}_0 e^{i\omega t} = \boldsymbol{E}_0[\cos(\omega t) + i\sin(\omega t)] \tag{4.3.2}$$

$$\boldsymbol{\Sigma}(\omega) = \boldsymbol{\Sigma}_0 e^{i(\omega t+\delta)} = \boldsymbol{\Sigma}_0[\cos(\omega t + \delta) + i\sin(\omega t + \delta)] \tag{4.3.3}$$

where $\boldsymbol{E}_0 = \boldsymbol{E}\Big|_{t=0}$, $\boldsymbol{\Sigma}_0 = \boldsymbol{\Sigma}\Big|_{t=0}$. Practically, only the real part of eqs.(4.3.2) and (4.3.3) is applied to the specimen during the dynamic test. However, writing the stress and the strain in exponential form makes it simpler to derive the equations for complex compliance or modulus. By substituting eqs.(4.3.2) and (4.3.3) into the constitutive equation (4.3.1), one obtains

$$\boldsymbol{\Sigma}_0 e^{i\omega t+\delta} + \frac{C_1}{E_0 + E_1} i\omega \boldsymbol{\Sigma}_0 e^{i\omega t+\delta} = \frac{E_0 E_1}{E_0 + E_1}\ \boldsymbol{E}_0 e^{i\omega t} + \frac{C_1 E_0}{E_0 + E_1}\ i\omega \boldsymbol{E}_0 e^{i\omega t} \tag{4.3.4}$$

Upon factoring and rearranging of terms, the componentwise solution for complex compliance in the z-direction, as shown in Fig. 4.1, can be written as

$$D^*(\omega) = \frac{\dfrac{i\omega}{E_0} + \dfrac{E_0 + E_1}{C_1 E_0}}{i\omega + \dfrac{E_1}{C_1}} \tag{4.3.5}$$

Further, upon multiplying both sides of this equation by their complex conjugates, and then simplifying the result, an expression for the complex compliance is derived in the form

$$D^*(\omega) = D_g + \frac{D_1}{\omega^2\tau_1^2 + 1} - i\frac{\omega D_1 \tau_1}{\omega^2\tau_1^2 + 1} \tag{4.3.6a}$$

$$\text{with} \quad \tau_1 = \frac{C_1}{E_1} \quad \text{and} \quad D_1 = \frac{1}{E_1} \tag{4.3.6b}$$

where τ_1 is a time delay due to the presence of dashpot elements. It should be noted that the expression $1/E_0$ is substituted by D_g, which is known as the Glassy compliance. According to eq.(4.3.6), the elastic and the viscous compliances are defined as the real and imaginary parts of the complex compliance, respectively. It should be noted that the negative sign of the imaginary part in the expression for the loss compliance is dropped, as the function is positive. Hence, the compliance equations are

$$D^*(\omega) = D_e(\omega) + D_v(\omega) \quad , \quad D_e(\omega) = D_g + \frac{D_1}{\omega^2\tau_1^2 + 1} \quad , \quad D_v(\omega) = \frac{\omega D_1 \tau_1}{\omega^2\tau_1^2 + 1} \tag{4.3.7}$$

where $D_e(\omega)$ is the elastic compliance and $D_v(\omega)$ is the viscous compliance.

It is not advisable to use the generalized Kelvin model with one Kelvin unit for modeling the time-dependent behaviour of the atrial tissue. In fact, the generalized Kelvin model with n Kelvin units yields higher-order differential equations and models the behaviour of the tissue accurately. In addition, the constitutive equation of the generalized Kelvin model can be written in the form of a Prony Series, which is a more suitable representation of the behaviour of viscoelastic materials when performing Finite Element Analysis (FEA). Figure 4.6 shows the generalized Kelvin model elements. The constitutive equation derived for a generalized Kelvin model with one Kelvin unit can be expanded as a model with n Kelvin units [131]. The elastic and viscous compliance for the generalized Kelvin model with n Kelvin units is expressed

as

$$D_e(\omega) = \frac{1}{E_0} + \sum_{i=1}^{n} \frac{1}{E_i(\omega^2\tau_i^2 + 1)} \quad , \quad D_v(\omega) = \sum_{i=1}^{n} \frac{\omega\tau_i}{E_i(\omega^2\tau_i^2 + 1)} \tag{4.3.8}$$

4.4 Experiments

In Section 4.2.2, a mathematical model was developed to model the contact between tactile sensor and viscoelastic tissue. The model needs to be populated with compliance data of the tissue, which can be found experimentally. Researchers use different techniques, such as dynamic testing, to measure the viscoelastic behaviour of tissue [132, 133]. Dynamic Mechanical Analysis (DMA) is a technique for studying and characterizing the behaviour of viscoelastic materials such as tissue. To find the tissue compliance, a test setup was designed to conduct DMA on heart tissue using a Bose ElectroForce 3200 device. First, the left atrial tissue of a swine heart was selected for testing, as it was easier to cut in the required shape. Since the left atrial tissue is constrained inside the heart, the same boundary conditions should be recreated in the testing procedure to obtain accurate results. However, for simplification, these boundary conditions were not applied to the sample tissue during DMA. The tissue was only constrained from the top and the bottom. Figure 4.7 shows the position of the tissue between the jaws of the ElectroForce device. The temperature of the jaws and the tissue during tests was considered constant. To test the tissue dy-

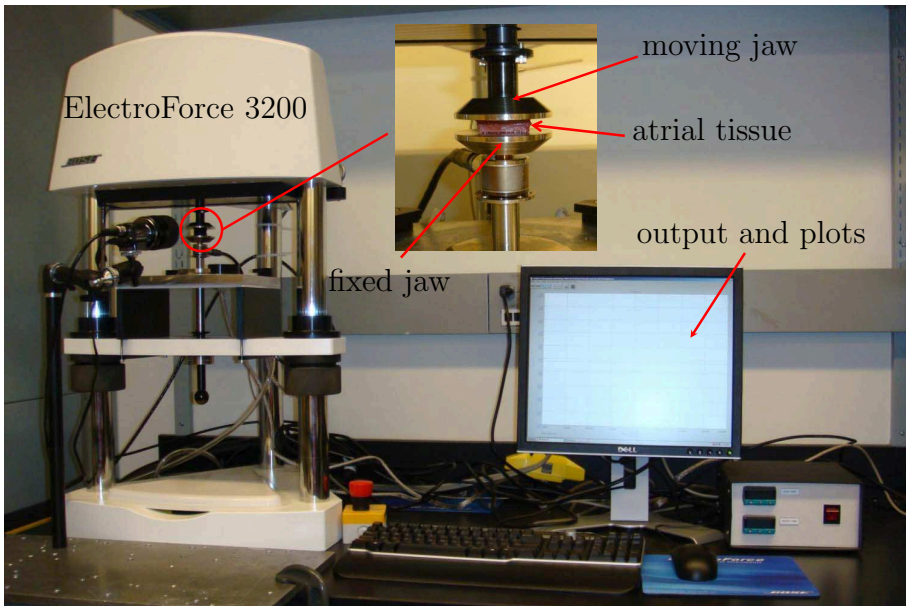

Figure 4.7: The position of the sample tissue between the two jaws of the device

namically, harmonic load and displacement were applied to the tissue. Measurement of the response of the tissue to periodic deformation or load shows that the stress and strain are not in phase. The strain lags the stress by a phase angle δ, namely,

$$\tan[\delta(\omega)] = \frac{E_v(\omega)}{E_e(\omega)} \tag{4.4.1}$$

where $E_e(\omega)$ and $E^v(\omega)$ are the elastic and viscous moduli, respectively. The elastic complex modulus can also be defined as

$$E^*(\omega) = E_e(\omega) + iE_v(\omega) \tag{4.4.2}$$

To conduct DMA, a series of test conditions is defined and applied to the test procedure systematically. A range of different frequencies, between 1 Hz and 36 Hz, was applied to the sample in eight different cycles. The frequency was increased by 5 Hz

for each subsequent cycle, starting from 1 Hz. Figure 4.8 shows the scope image of two successive test cycles.

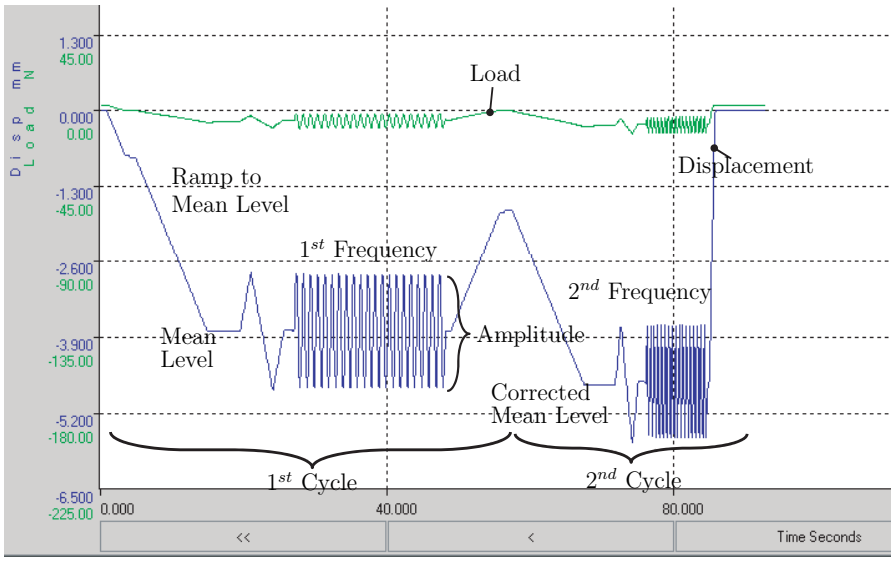

Figure 4.8: The graphical view of the two consecutive test cycles with different frequencies

The upper jaw first ramps to a specified load hold level, which is again held for a predefined time to allow the dimensions of the specimen and fixture to adjust to the temperature. This reading is used as a relative zero position for all subsequent commands and force feedback. The system then ramps to the specified mean level, which is held again for a specified time to allow for any creep or relaxation to occur prior to dynamic testing. Once the dynamic cycling has begun, the specimen is pre-cycled a user-specified number of cycles to allow for amplitude control and specimen

stabilization prior to data being taken.

Data are taken at an optimum acquisition rate for analysis. The dynamic cycling is then stopped and the system again ramps to the original load condition while data are stored to minimize dynamic cycling of the specimen and prepare for the next test condition. The WinTest software package then calculates the output data automatically, according to the size of the specimen, which has been input to the package. Figure 4.9 shows the recorded response of the specimen to the applied displacement to show the phase difference between the two scope data curves.

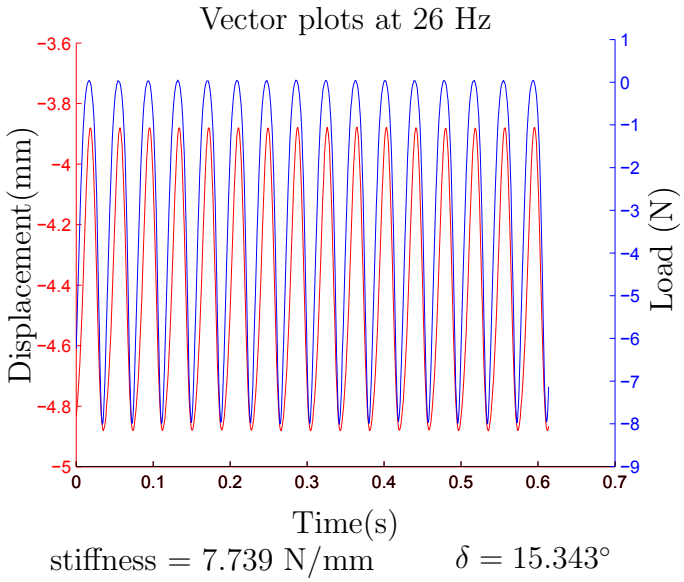

Figure 4.9: The scoped signals of load and displacement to represent the phase difference between two signals

Upon conducting DMA tests at different frequencies, the complex, the viscous, and the elastic moduli were converted from the recorded response data to the frequency

domain, as shown in Fig. 4.10. The next step is to populate the viscoelastic model of

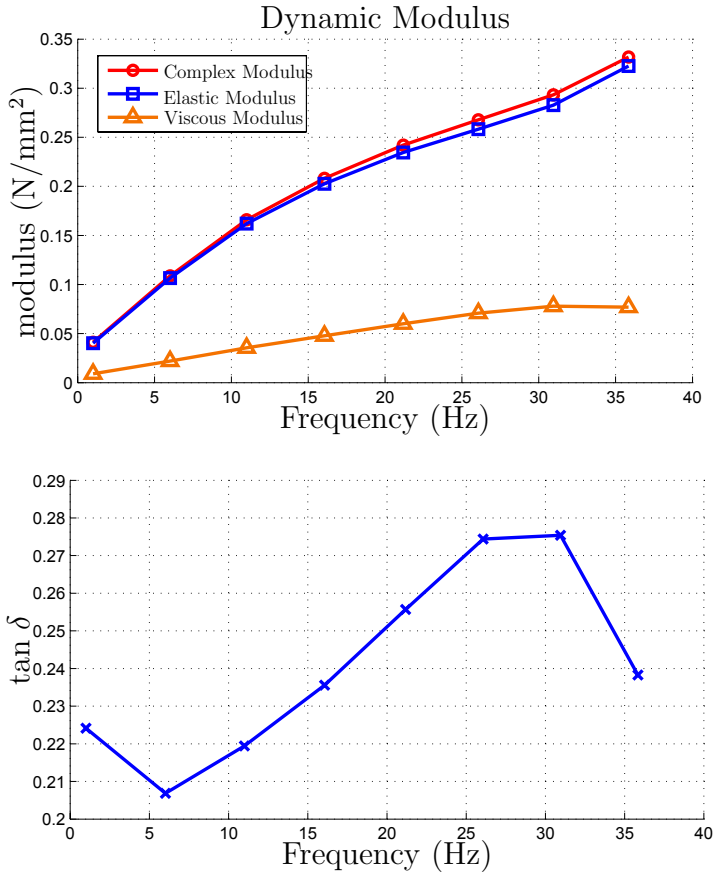

Figure 4.10: Complex modulus, elastic modulus, viscous modulus, and tanδ for swine heart atrial tissue

the tissue with the DMA test data, which requires using an optimization method.

4.5 Parameter Identification via a Genetic Algorithm

By using optimization techniques, the data obtained can be fitted to the constitutive equations. A genetic algorithm (GA) is used to obtain the constants of the generalized Kelvin model formulated in Section 4.3. A brief description of the GA is included below.

Genetic algorithms are based on Darwin's theory of evolution, *survival of the fittest* [134]. GAs search the solution space of a function by creating a simulated evolution. A population of solutions is created, then mated with different techniques to create new generations. The fittest individuals of any population tend to survive by becoming parents to the next generation. The chromosomes of each population are selected randomly from the solution space. Each individual is assigned a fitness value according to the predefined fitness function. Those having stronger chromosomes and higher fitness value have a greater chance of being selected for the next generation. When they unite with others, in a process called crossover, the child they create will likely posses an even greater fitness value than the parents. In addition, the individual chromosome genes can be randomly changed in a process called mutation in order to search the wider space of the solution and to avoid falling into local minima. GAs do not require exact knowledge of the search space, as in the case of deterministic

Constants	Fitness Values (MPa)	Constants	Fitness Values (s)
E_0	56.45258219	τ_1	2.455236432
E_1	0.003942097	τ_2	2.405097351
E_2	0.007498926	τ_3	0.021752025
E_3	0.060282772	τ_4	2.440387389
E_4	0.002390291	τ_5	2.416770843
E_5	0.006842171	τ_6	2.392975402
E_6	0.005091904	τ_7	0.021876111
E_7	0.093982545	τ_8	2.438807782
E_8	0.001876492		

Table 4.1: Constants for the compliance of generalized Kelvin model

methods [135].

The *objective function* $f(\boldsymbol{\chi})$ to be minimized is defined as the square of the Euclidean norm of the error in the approximation of both the elastic and viscous compliance, $D_e(\omega)$ and $D_v(\omega)$, respectively, as defined in eq.(4.3.8), each comprising eight elements, i.e., with $n = 8$. To construct the objective function $f(\boldsymbol{\chi})$, two 8-dimensional arrays $\boldsymbol{g}$ and $\boldsymbol{v}$ are defined as

$$g_i = D_e^{num}(\omega_i) - D_e^{exp}(\omega_i) \qquad v_i = D_v^{num}(\omega_i) - D_v^{exp}(\omega_i) \qquad i = 1, \ldots, 8$$

where $D_e^{num}(\omega_i)$ and $D_v^{num}(\omega_i)$ denote the fitting values for the elastic and viscous compliances, while $D_e^{exp}(\omega_i)$ and $D_v^{exp}(\omega_i)$ are their counterpart experimental values, and ω_i is the frequency. The best fitness with the experimental data was found under these conditions, with a total of 17 unknown parameters, namely,

$$\boldsymbol{\chi} = [E_0, E_1, \ldots, E_8, \tau_1, \ldots, \tau_8] \tag{4.5.1}$$

The fitness function is thus

$$f(\boldsymbol{\chi}) = \|\boldsymbol{g}\| + \|\boldsymbol{v}\| \quad \rightarrow \quad \min_{\boldsymbol{\chi}} \tag{4.5.2}$$

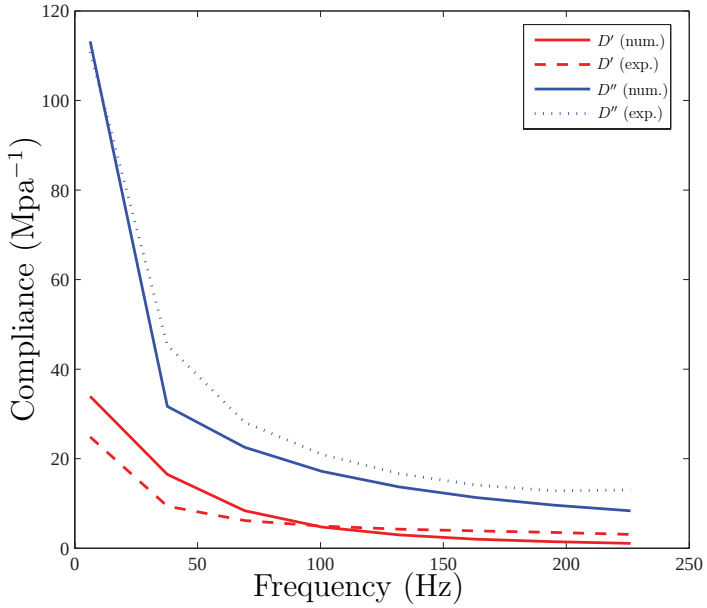

Figure 4.11: Comparison of the experimental results and the model results for the compliance of the atrial tissue

The compliance constants obtained by the GA are summarized in Table 4.1. Figure 4.11 shows a comparison of the compliance of the tissue and the model developed with the generalized Kelvin model with 17 constants. Apparently, the model can fairly replicate the elastic and viscous compliance of the atrial tissue.

4.6 Results

For solving a viscoelastic boundary-value problem, the time-dependent constitutive equation poses many challenges. However, in situations with fixed boundary conditions, elasticity results can be extended into the viscoelastic realm upon invoking the correspondence principle [136]. Although the integral constitutive equation offers many advantages at this stage, its differential counterpart is used because of its simplicity. Hence, the generalized form of eq.(4.3.1) can be expressed by using linear time derivative operators P_1^d, Q_1^d, P_2^d, and Q_2^d to express the viscoelastic model of springs and dashpots, as

$$P_1^d \boldsymbol{\Sigma}_e = Q_1^d \boldsymbol{E}_e, \quad P_2^d \boldsymbol{\Sigma}_v = Q_2^d \boldsymbol{E}_v \tag{4.6.1}$$

where $\boldsymbol{\Sigma}_e$ is the stress deviator, $\boldsymbol{\Sigma}_v$ the hydrostatic stress, $\boldsymbol{E}_e$ the strain deviator and $\boldsymbol{E}_v$ the hydrostatic strain. Furthermore, $\bar{P}_i^d$ and $\bar{Q}_i^d$ denote P_i^d and Q_i^d, for $i = 1, 2$, in the domain of the Laplace variable s. According to the correspondence principle, by replacing $2G$ with $\bar{Q}_1^d/\bar{P}_1^d$, and $3K$ with $\bar{Q}_2^d/\bar{P}_2^d$ in the elastic solution, the corresponding viscoelastic solution in the Laplace domain can be found. The viscoelastic solution in the time domain is obtained by means of the inverse Laplace transform.

Most kinds of tissue can be assumed to be incompressible [137]. Hence, in the case at hand, the Poisson ratio ν of the tissue is assumed to be 0.5. The shear constitutive relation is also represented by the generalized Kelvin model shown in Fig. 4.12, its

differential constitutive equation being

$$\sum_{k=0}^{8} m_k \frac{d^k \boldsymbol{\Sigma}_e}{dt} = \sum_{k=0}^{8} h_k \frac{d^k \boldsymbol{E}_e}{dt} \tag{4.6.2}$$

where m_k and h_k are functions of the constitutive parameters.

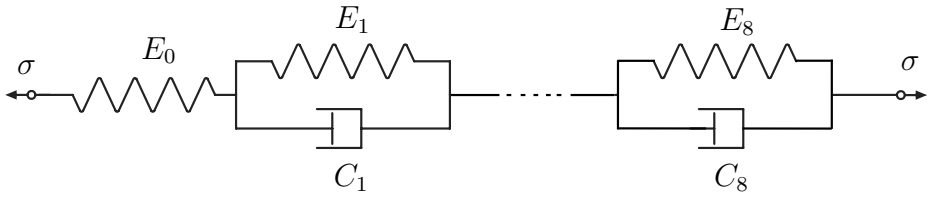

Figure 4.12: The eight-element generalized Kelvin model

Thus, the extension of eq.(4.2.21) to viscoelasticity can be achieved by setting ν to 0.5 and replacing G with

$$G = \frac{\sum_{n=0}^{8} h_n s^n}{2 \sum_{k=0}^{8} m_k s^k} \tag{4.6.3}$$

After introduction of the inverse Laplace transform and substitution of the constitutive parameters obtained in Section 4.5, the relation between force and indentation displacement is obtained as

$$\begin{aligned} \epsilon_0 = \frac{p}{4 r_o \kappa} (1708.08 - 10.64 e^{-4.29t} - 16.58 e^{-2.77t} - 133.35 e^{-0.0031t} - 146.15 e^{-0.0028t} \\ - \ 196.39 e^{-0.0021t} - 253.67 e^{-0.0016t} - 418.36 e^{-0.00098t} - 532.91 e^{-0.00077t}) \end{aligned} \tag{4.6.4}$$

$$\kappa = 1 - \frac{4\beta^3}{3\pi^2} - \frac{\beta^4}{8} \tag{4.6.5}$$

where r_o is the radius of the larger force sensor, κ is a function of the ratio of the inner to the outer radius, t is time, and p is the force applied to the sensor. This

equation can be used for the contact between the atrial tissue and a tactile sensor or a surgical catheter having annular shape with various inner and outer radii. The indentation displacement for various ratios and forces are plotted in Fig. 4.13. This figure shows the relation between the indentation displacement, the force applied to the sensor, time, and the ratio of the inner to the outer radius.

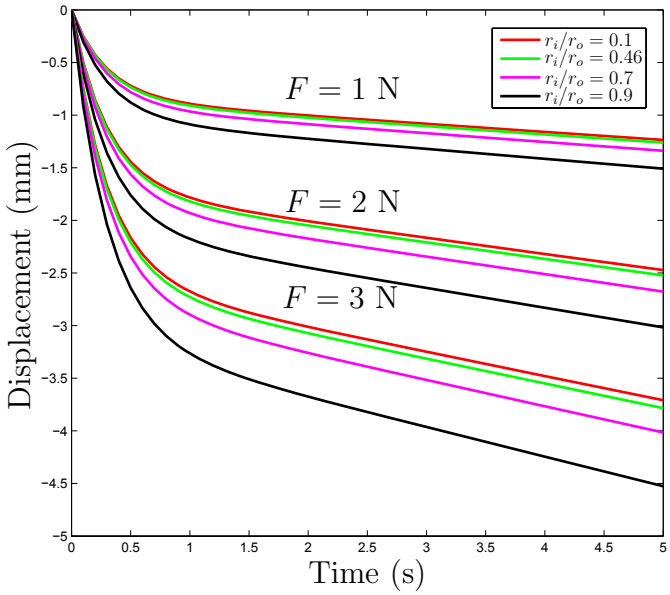

Figure 4.13: The indentation displacement for various ratios and forces

4.7 Discussion

The model for annular viscoelastic contact here derived reveals significant information about the tool-tissue interaction. The contact model can be used in several applications, as: (1) to analyze the tissue indentation depth inside the hollow space

of the tactile sensor, and to select the optimum dimensions for the sensor; (2) to optimize the design of surgical catheters by analyzing the indentation depth of the tissue, as robotic catheters usually have an annular shape; and (3) to simulate the real-time response of tissue being touched by a surgical catheter under quasi-static loading conditions. In addition, since the contact model developed here is parametric, the simulation of the tissue behaviour is much faster and simpler when compared to other modeling techniques such as FEA. Hence, the contact model can be used in real-time graphical and haptic-based training simulators to replicate the viscoelastic behaviour of tissue in contact with catheters and surgical instruments.

According to Fig. 4.13, the difference in the ratio of the inner to the outer radius of the tactile sensor has a higher influence on the indentation displacement for larger applied forces. In reality, the applied force on tissue during RAS should be limited and minimized in order to avoid any possible damage to the heart tissue. It is recommended to keep the force applied to the heart tissue lower than 2 N, if possible, without exceeding 3 N [138]. In addition, since the tissue may have a convex/concave surface, this may lead to pre-penetration of the bulge of tissue inside the hollow space of the tactile sensor. In order to reduce those effects, the ratio of the inner to the outer radius of the tactile sensor should be decreased; alternatively the diameter of the small sensor should be reduced to avoid pre-penetration of the tissue. Furthermore, less sensing time is of interest in RAS. Therefore, the optimum dimensions of

the tactile sensor should obey $r_i/r_o = 0.1$ and $L = 0.7$ mm, according to Fig. 4.13. In this case, by applying a 1N force for a duration of 0.5 s, the atrial tissue penetrates and touches the surface of the smaller sensor.

The same discussion of the optimum dimensioning of tactile sensor can be used in size optimization of surgical catheters, based on the conditions for which they are intended.

The contact model can be also used in quasi-static conditions to replicate the response of the tissue to dynamic loads. For example, if a constant static load $F_1 = -0.2$ N is applied to the tissue, and a harmonic load $F_2 = 0.2\sin(2\pi t)$ is added to the constant load after 2 s, the tissue shows different behaviour for each condition. To find the response of the tissue to the dynamic load, the equation of applied force is written in the Laplace domain as

$$\bar{p} = -\frac{0.2}{s} + \frac{\pi}{2e^{2s}(s^2 + 4\pi^2)} \tag{4.7.1}$$

By substituting eq.(4.7.1) in the Laplace domain eq.(4.2.21), and by applying the inverse Laplace transform, the equation of the indentation of tissue for the dynamic load is derived as

$$\epsilon_0 = [H(t-2)(-2.86e^{7.07t}\cos(6.28t) + 6679.99e^{2.78t} + 391.05e^{4.31t} + 0.06e^{7.07t} + 1.52e^{7.07t}\sin(6.28t)) + 2.12e^{2.78t} + 3.31e^{4.30t} - 5.46e^{7.07t}]/(4r_0\kappa e^{7.07t}) \tag{4.7.2}$$

where $H(t-2)$ is the Heaviside step function. Based on eq.(4.7.2), the indentation

depth of the tissue for different ratios of the outer to the inner radii is plotted in Fig. 4.14. As can be seen, the tissue shows a combination of creep and harmonic deformation to the force applied. For the first 2 s, the tissue deforms and shows creep behaviour due to the constant load; after adding the harmonic load to the previous one, the tissue shows the dynamic indentation, while having the creep behaviour due to the constant load. Therefore, Fig. 4.14 shows that the contact model here developed can replicate the tissue viscoelastic behaviour for dynamic loads.

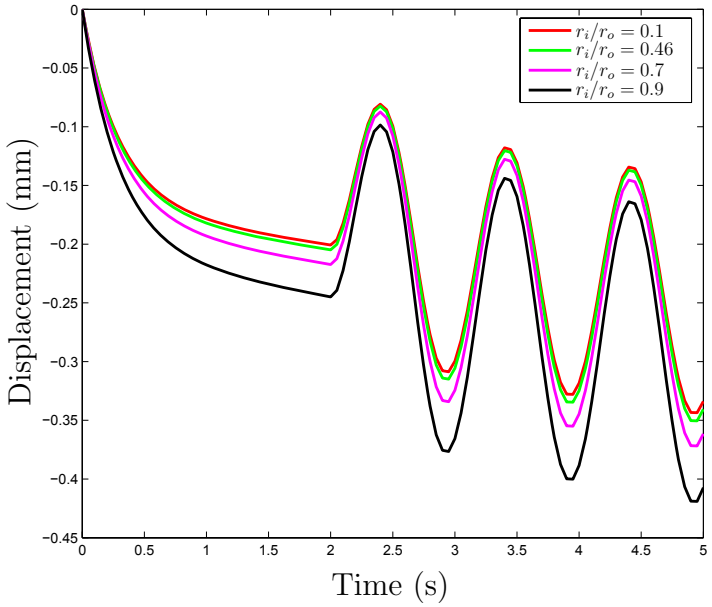

Figure 4.14: The response of the tissue for quasi-static loading conditions

Chapter 5

A New Array Sensor for Soft Tissues with Time-Dependant Behavior

This chapter describes the development of a new type of tactile sensors for use in MIS, where the interaction with soft tissue is dominant. Review articles show that tactile sensors are being developed with various designs and transduction methods, e.g., piezoelectric, piezoresistive, optic, pneumatic, etc. Although many types of tactile sensors are being developed by researchers, the variety of data being collected with these sensors are very limited and similar to each other. Many of tactile sensors being used in either industry or academic areas can only read the pressure/force

mapping during the touch. Other newly developed tactile sensors can extract force and displacement data during touch. The force and displacement data can relatively convey the concept of young modulus, compliance, or hardness based on the design of the sensor and based of the way measurements were conducted. The developed tactile sensors measure the degree of softness/hardness with acceptable accuracy. However, in tissue related applications, extra parameters about viscoelastic behavior of tissue can be measured to add more certainty to the sensor output, where tissues show similar properties. The new parameters that can be measured are the force rate and displacement rate, in addition to force and displacement measurements. The force rate and displacement rate can be taken into account by virtue of time-dependent response of the tissue to stress or strain. If timing is taken into account during touch mechanism, different tissues can be touched with the same displacement rate by the tactile sensor, resulting in more accurate comparison. Our experiments show that a single tissue shows different force-displacement behaviour for different displacement rates application. Therefore, in measuring the degree of hardness, the same strain rate should be maintained to all of tissues during touch. So, it becomes crucial to record the time for the force rate and the displacement rate measurements.

5.1 Sensor Structure Design

In this chapter a new design of tactile sensor is introduced based on piezoresistive sensing principle. The sensor is capable of measuring time-dependent behavior of tissues in addition to hardness measurement. In detail, force, displacement, and the average displacement rate can be measured with this new array tactile sensor, which is composed of two piezoresistive array sensors and one piezoresistive force sensor. The piezoresistive array sensors act as tactile switches to trigger recording the output of the single force sensors. The schematic exploded configuration of the tactile sensor is shown in Fig. 5.1

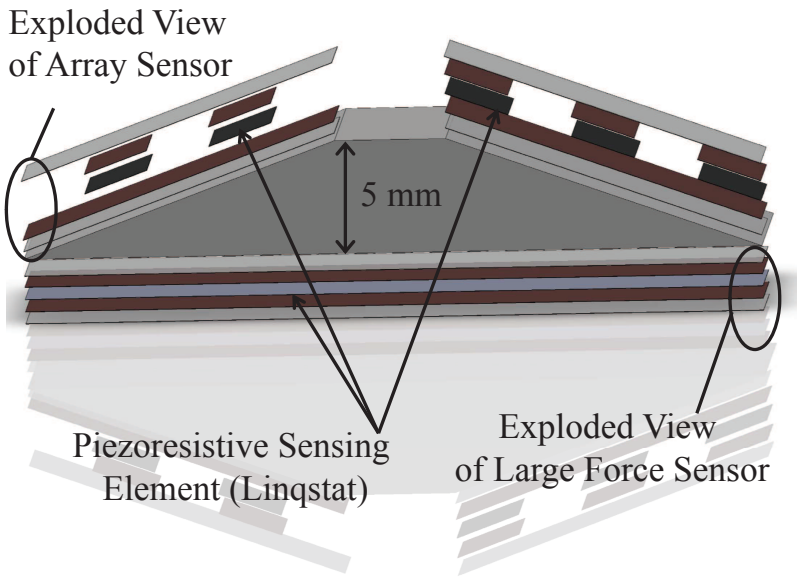

Figure 5.1: Schematic exploded view of the sensor and its components

The piezoresistive sensing array on the left side of the sensor has two sensing

elements, while the sensing array on the right side has three sensing elements. The arrangement of the sensing elements on each side of the sensor is in a way that the summation of the two arrays together can cover the total height of the sensor with sensing elements. Together, the two array sensors have five sensing elements, tactile switches, to cover the $5mm$ indentation depth of the sensor.

5.1.1 Sensor Fabrication

To manufacture the sensor—similarly to fabrication method in chapter 3—two array sensors, one force sensor, and a trapezoidal plate are fabricated and integrated together. Each of the array sensors consists conductive electrodes, polyester films, and piezoresistive sensing elements, see Fig. 5.2. One of the electrodes is commonly used by all of sensing elements. The electrodes are covered with two layers of polyester film, or silicone tape from top and bottom. The thin layer of the polymer composite is then sandwiched between the two layers of electrodes. The trapezoidal plate is manufactured from steel.

After fabrication of the individual components of the array tactile sensor, Fig. 5.3a, the elements are adhered together to form the tactile sensor as shown in Fig. 5.3b. The electrical circuit of the array sensors is similar to those in Chapter 3, but in array format.

In both array sensors, there are total of five tactile switches, which have $1mm$

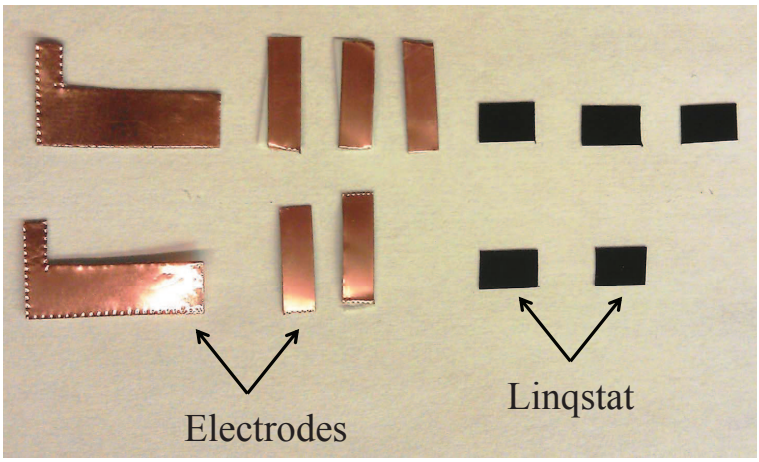

(a)

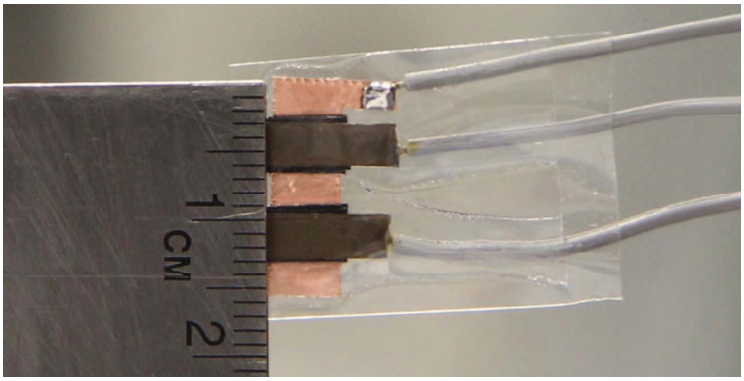

(b)

Figure 5.2: (a) Components of array sensor (b) The fabricated array sensor size

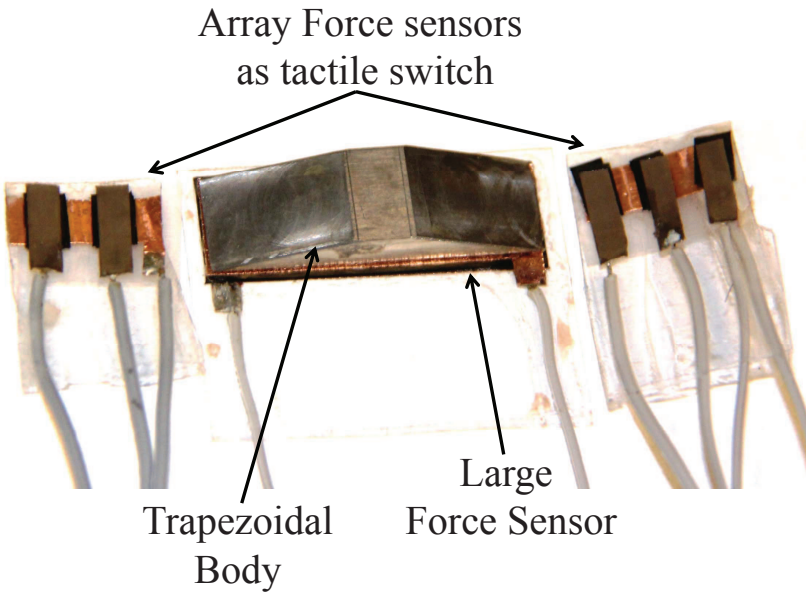

(a)

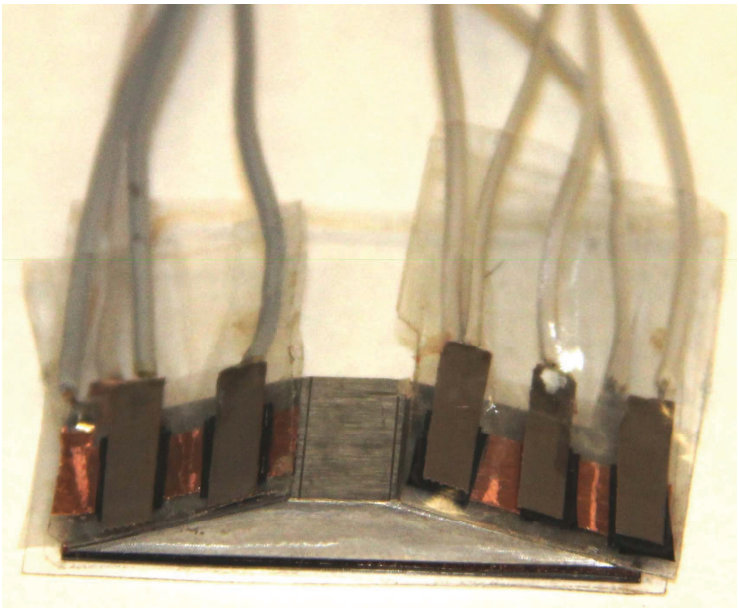

(b)

Figure 5.3: (a) Manufactured components of the array tactile sensor (b) Fabricated tactile sensor

perpendicular distance from each other. Therefore, during the indentation of tactile sensor into the tissue, tactile switches send five separate signals for force and time recording purpose in each $1mm$ indentation depth for the total length of $5mm$. The trapezoidal plate has a 20° angle on each side, which was found experimentally.

5.2 Sensing Algorithm

A novel sensing algorithm is developed for the tactile sensor. The algorithm is relatively simple and has several features for measuring different tissue properties. Figure 5.4 shows the flowchart for the sensing algorithm. As shown in the flowchart, the output of the large force sensor is being continuously measured to ensure that the tissue is in touch with the force sensor. A threshold value can be also assigned for the large sensor output, in presence of noise. For piezoresistive sensors, this threshold value is set to zero by virtue of the low noise generation in their structure. If the output signal of the sensor becomes larger than the threshold value, here zero, then it means that the sensor is touching the tissue and the time recording process starts from that moment. Following the application of force, the sensor penetrates inside the tissue, therefore reaching the tactile switches on the sensor in each $1mm$ indentation depth. At the instant of tissue contact with tactile switches, the force output of the large sensor and the time is recorded. Therefore it can be considered that

$$F = F_i, \quad \text{and} \quad \delta T = T_i - T_{i-1} \tag{5.2.1}$$

where F_i is the measured force at each instant $i = 1 \cdots 5$, and δT is the time during which the tissue is displaced for $1mm$ in the ith step. So, for each complete indentation depth, five different δT is being recorded. By taking the average of these five displacement timing, the average displacement rate can be achieved for each complete touch, as

$$\bar{V} = \frac{5}{\sum_{i=1}^{5} T_i} \quad (mm/sec) \tag{5.2.2}$$

where $\bar{V}$ is the average displacement rate, i.e., average velocity.

During touch, first, the tissue is pressed by the sensor, and then the tissue is released. The recorded force, time, and displacement measurements during loading is of interest in tactile sensing. However, the tactile switches of the sensor are in contact with the sensor both during loading and unloading, continuously sending data to the program. To distinguish useful data—those extracted during loading—shift registers are used, i.e., the recorded output from a tactile switch in time N is compared with both previous data in time $N - 1$ and a pre-defined threshold value. If the data is greater than those two latter, then it means that data is being taken during loading part of the touch, otherwise data is ignored. Since the tactile switches has the same structure of force sensor, therefore its output voltage has direct relation

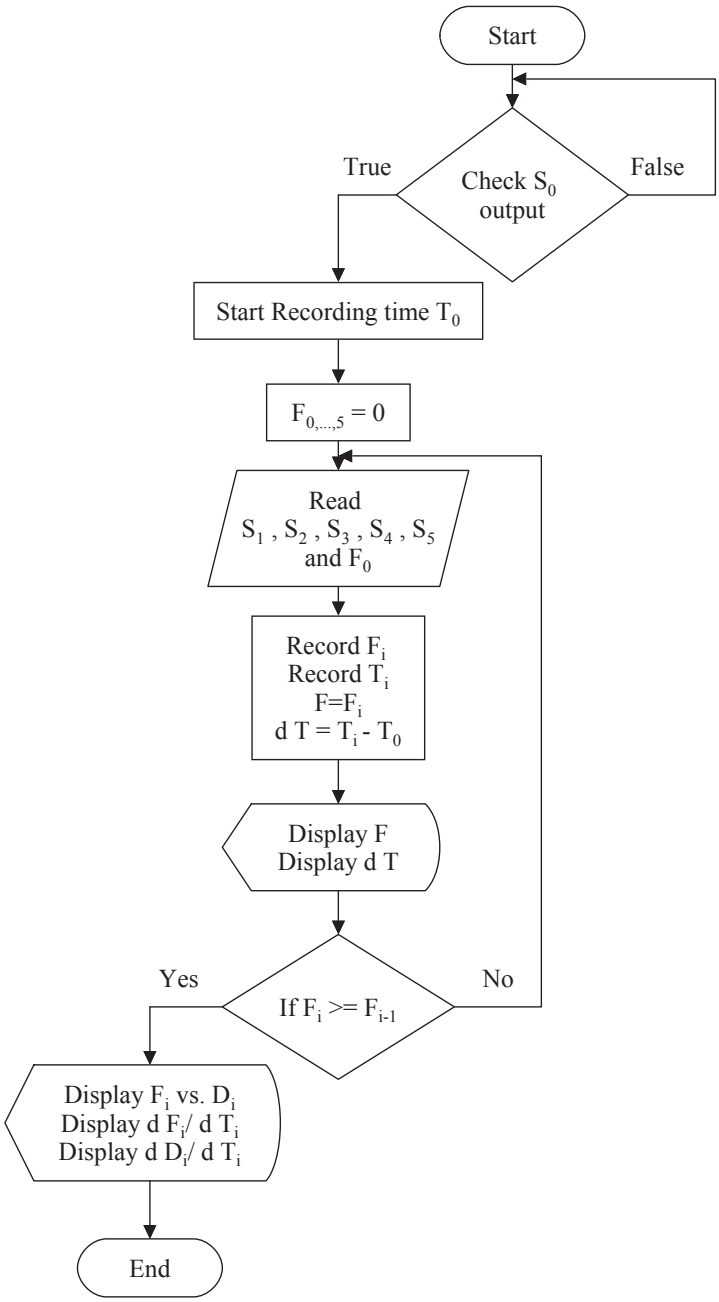

Figure 5.4: The sensing flowchart for the tactile sensor

with the applied force. So, the increase in the output signal has direct relation with the increase in force. In the case of the large force sensor, its output is calibrated; and the output data is converted to the force in the program based on the calibration process, as stated in previous chapters.

The depicted algorithm in Fig. 5.4 is developed in LabView environment as shown in Fig. 5.5.

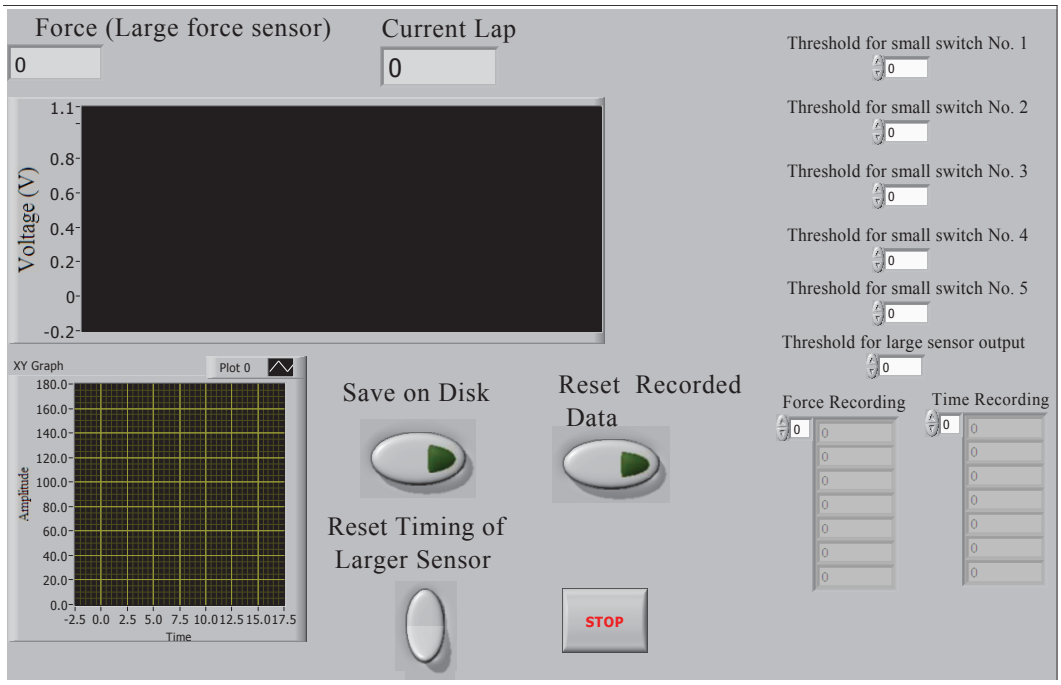

Figure 5.5: The display for array tactile sensor in LabView environment

5.3 Experiments

To test the output of the sensor, three different types of tissue with different softness degrees were selected. The three tissues were diced and cut into cubic shape with the same size. The sensing principle of the array tactile sensor is the same with the tactile sensor in Chapter 3. Therefore, explanation about the sensor characteristic and connecting array tactile sensor to the written code is avoided in this chapter (Please refer to Section 3.1.2 for more details and explanations). The sensor is placed on the upper jaw of the ElectroForce Bose 3200, and the tissue is place on the lower jaw. Constant displacement $5mm$ is applied to the same type of tissue samples progressively. As shown in Fig. 5.6, the tactile sensor penetrates inside the tissue for measuring its properties.

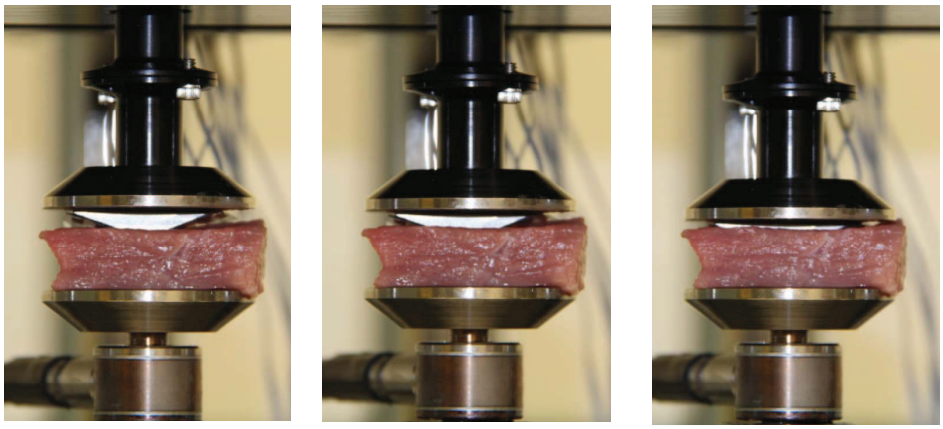

(a) (b) (c)

Figure 5.6: Progressive indentation of the tactile sensor into the tissue

In the experiment, the tissues are selected and diced into cubic shape with the

same size. Then the sensor is pressed on the tissue, as shown in Fig. 5.6, several times each time with a different displacement rate. The average velocity, displacement, and force is measured by the tactile sensor. The results showed that the force-displacement behaviour of tissue changes with different displacement rates. Figure 5.7 shows the measured data for one tissue with different displacement rate. It shows that displacement rate can change the tissue response to force or displacement.

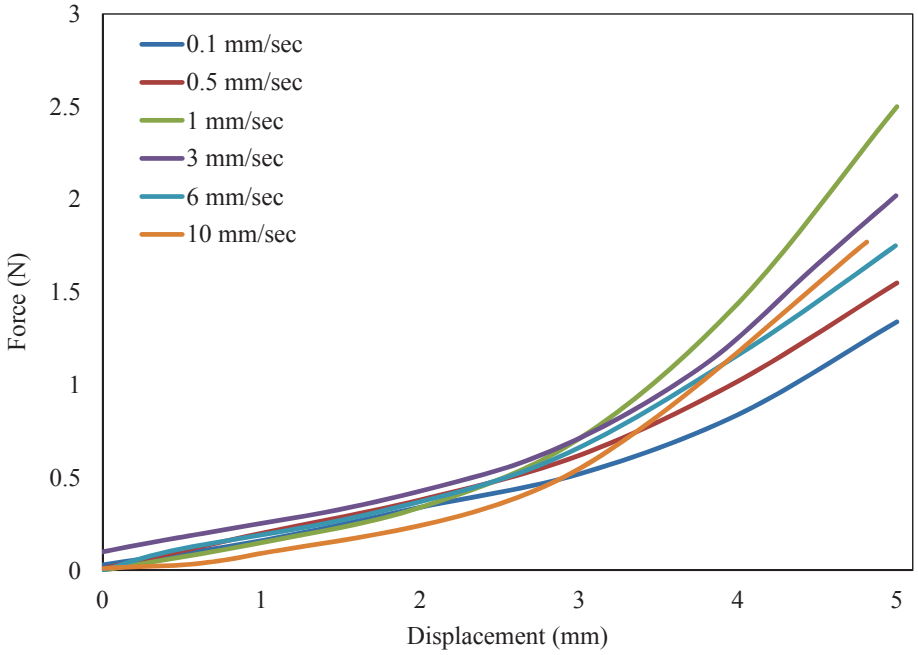

Figure 5.7: Force-displacement response of tissue for different displacement rates

The same type of test with other tissues also resulted in similar tissue response, confirming the different force-displacement behaviour for one type tissue. In a different experiment, the tactile sensor is used to distinguish the softness degree of three different tissues with several indentation rates. First, all of the three tissues were

tested with $1mm/s$ displacement rate, as shown in Fig. 5.8. The results show that tissue 2 is harder than tissue 1; and tissue 1 is harder than tissue 3 for $1mm/s$ displacement rate. Interestingly, the three tissues show very similar behaviour during the first $1mm$ indentation. It is hard to clearly distinguish the difference in the hardness degree between the three tissues; The behaviour of tissue 1 and 2 is similar, even for $2mm$ indentation. By increasing the indentation depth, tissue 2 shows a higher hardness degree. In fact this situation is the same in reality, i.e., one tries to push more with his finger, if it becomes difficult to distinguish between the softness degree of two objects with similar response. In the experiments, the tissues behaviour changes drastically by changing the displacement rate. For example, the behaviour of tissue 1 and 3 varies by changing the displacement rate to $0.5mm/s$. Tissue 1 shows softer property while tissue 3 shows harder property, even harder than tissue 1 with $1mm/s$ displacement rate. However, tissue 3 shows higher hardness with increasing the displacement rate to $3mm/s$. Therefore, it can be said that tissue 2 is generally harder than tissue 1 and 3. However, the hardness difference of tissue 1 and 3 can be decided based on the displacement rate. This shows that displacement rate is a determining factor in distinguishing the hardness degree for materials with similar viscoelastic properties.

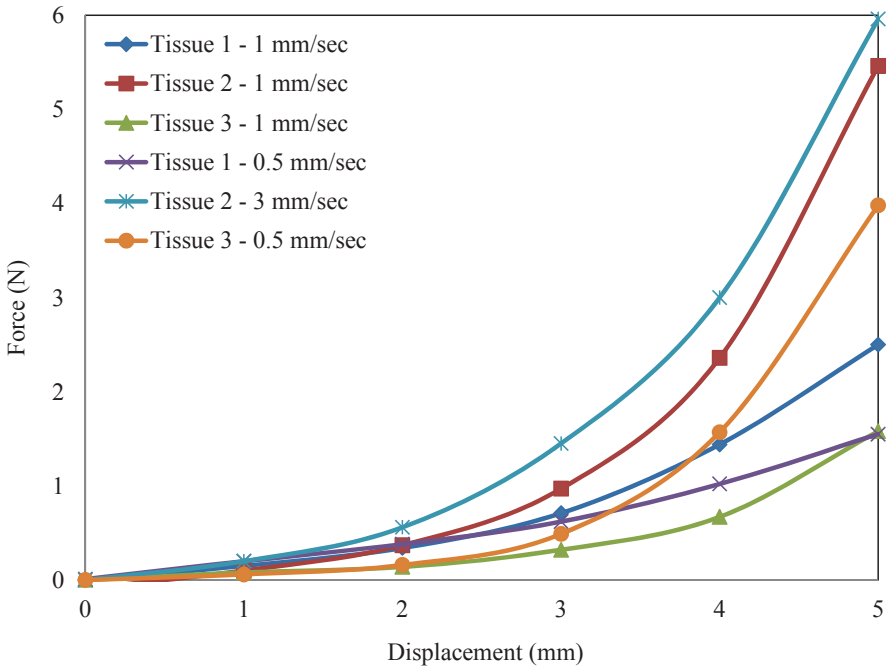

Figure 5.8: Test results of tactile sensor on three tissue with different displacement rate

Chapter 6

3D Graphical Display of Localized Lumps and Arteries

Detection of hard inclusions within soft tissue in MIS, also referred to as laparoscopic surgery, is of great importance, both in clinical and surgical applications. In surgical applications, when any solid matter is being removed, it is important to avoid accidental injury to surrounding tissues and blood vessels since, were this to occur, it could then necessitate the need to resort to open surgery. This chapter describes a new system for localizing small masses during MIS procedures and shows how tactile sensors can now be integrated into a laparoscopic grasper in order to measure the applied pressure that is placed on the tissue [94, 139, 140]. In fact, two matrices of piezoresistive force/pressure sensors, which are described in Chapter 2, are being

used in order to show any embedded lump or arteries inside tissue in 3D. The tactile system, as shown in Figure 6.1, allows surgeons to explore the operation site in a more thorough and exact manner. Section 6.1 describes the major components of the tactile system. The sensor, probe mechanics, and image processing are explained in detail in Sections 6.2 and 6.3. Section 6.4 describes the experiment used to validate the performance of the system in a dry lab setting. Section 6.5 describes the results of the finite element simulations. Section 6.6 discusses the results of simulation and experiments.

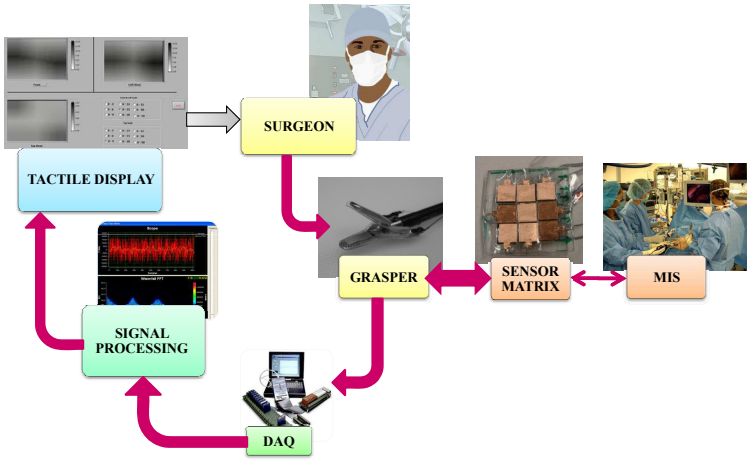

Figure 6.1: Schematic view of the relation between components

6.1 System Design

In this research work, the system we propose to employ uses an MIS grasper that is equipped with two matrices of piezoresistive pressure/force sensors on its jaws, a Data

Acquisition (DAQ) interface, and signal processing algorithms. The miniaturized scale of the piezoresistive sensors can be integrated on the tip of a variety of MIS laparoscopic and robotic graspers. When the surgeon uses a grasper and touches tissue that possibly contains a lump or an artery, the sensor matrices measures the pressure/force applied to the tissue at the grasping areas. Based on these pressure readings, electrical outputs of the sensor matrices are then transferred to the DAQ as a voltage input from which a program will confirm the location and presence of either a lump or artery in a three-dimensional display using LABVIEW software. Therefore, the system is capable of providing the surgeon with a visual display of arteries and lumps, in both dynamic and static modes, during the operating procedure.

6.2 Sensor Elements

In this current research work, piezoresistive force sensors fabricated from Linqstat (a semi-conductive polymer composite from CAPLINQ Corporation) are used to measure the applied force [87]. Semi-conductive polymer composites exhibit a decrease in electrical resistivity when a change in force is applied to their structure [87]. To fabricate the force sensor, a thin ($200\mu m$) layer of Linqstat is sandwiched between two layers of copper electrodes. The electrodes are then covered with two layers of polyester film. Figure 6.2a shows a view of the fabricated force sensor. Figure 6.2b

shows the inside view of the sensor and its electrical model [87]. Although the relationship between the resistance and the applied force is not linear, the conductance of the sensor has a linear relationship with force. Thus, in the calibration setup, the conductance is measured and converted to force according to their linear relationship. After conducting simple calibration tests [89], the relationship between the conductance and applied force to the sensor can be determined.

In this work, 18 different force sensors were used in two 3×3 matrices of force sensors. Calibration was performed on each sensor and all 18 force sensors were calibrated individually in the range of 0 to $20N$. The resolution of each fabricated force sensor is $0.1N$ and the repeatability of the sensor is $\pm 2.5\%$ of full scale with an appropriate static and dynamic response.

After calibration of sensors, the sensor matrix was assembled on a piece of plexiglass to perform experiments. The ElectroForce 3200 BOSE device was used to apply a normal load to the piezoresistive force sensor plane. In order to read the outputs, sensors were connected to a buffer circuit which, in turn, was connected to a DAQ board and finally to a PC. The buffer circuit was used to reduce the loading effect of the tactile sensors on the DAQ amplifiers in order to prevent crosstalk.

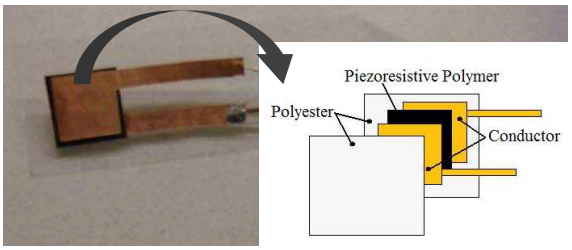

(a)

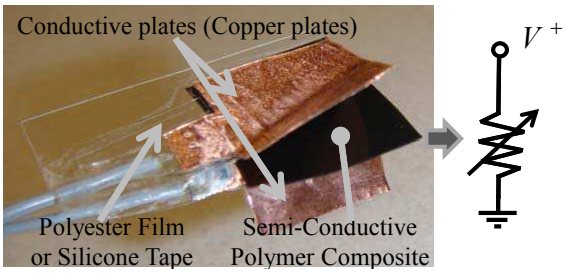

(b)

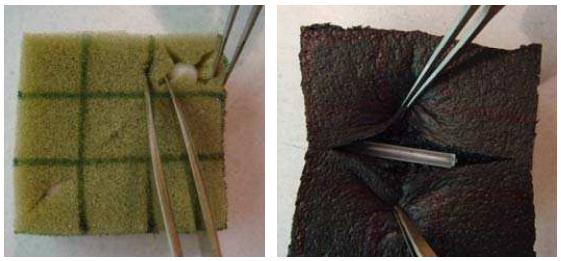

(c)

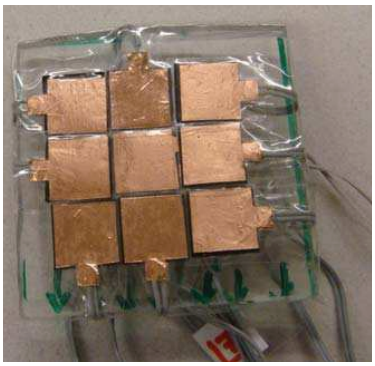

(d)

Figure 6.2: Schematic view of the relation between components (a) View of the fabricated force sensor using Linqstat and its components (b) Schematic view of the current flow geometry (c) Photograph of the elastomers, lump, and artery (d) Photograph of a sensor matrix

6.3 Lump Detection Algorithm

The output from an array of force sensors was fed into the DAQ which contained an algorithm that converted the location of lumps and arteries into a color band display. The color was proportional to the pressure registered by the corresponding sensing element. In [139], the algorithm for a one-dimensional lump detection, presented in [140], was extended for two-dimensional localization of lumps. Two arrays of sensing elements were used on both sides of simulated tissue. In this research work, two elastomeric materials B1 and ICF400 (from PROFOM Company), with different stiffness were used to simulate the behaviour of soft tissue to localize the lumps. A three-dimensional lump detection algorithm, presented in this work, is the extension of the algorithm used for two-dimensional lump detection. In order to understand the three-dimensional lump detection algorithm, the one and two dimensional detection algorithms should be studied in enough details, which is given in Appendix A. For a full discussion of these algorithms, please refer to [139, 140]. As shown in Fig. 6.2c (left), lumps were simulated by hard balls inserted inside elastomers. These balls have a much higher module of elasticity than elastomers. The existence of these hard balls inside elastomers can be detected by finger touch whereas arteries, on the other hand, are simulated by hard plastic tubes implanted inside elastomers as shown in Fig. 6.2c (right).

6.3.1 Lump Localization in Three Dimensions

Figure 6.3 shows the sensor array design for three-dimensional lump detection. Both upper and lower jaws of an endoscopic grasper are equipped with matrices of sensors. Two matrices are used to localize lumps in three dimensions. Each matrix consists of an array of 3×3 force sensing elements. The sensing elements on the upper and lower matrices are called U and L elements. The sensing elements have two indices that show the row and column of the sensing element in the matrix. For instance, $U2, 1$ is the sensing element located on the upper matrix on the second row and first column, and $L1, 3$ is the sensing element located on the lower matrix on the first row and third column. A lump in three dimensions is shown by using front view, left view, and top view. These views are shown in Fig. 6.3a. The algorithm, which is used to show the front view and left view in 3D, is very similar to the algorithm explained in 2D, the main difference is the arrangement of the sensing elements for each view. For the tactile image of the front view, only the column in which a lump is located is important. Figures 6.3aand 6.3b show the idea. In this arrangement, it does not matter if a lump is located on the first, second, or third row. Only the column in which a lump is located would affect the front view image. For example, if a lump is located on $L1, 2$, the image is no different to that of an image of a lump located on $L2, 2$ or $L3, 2$. In fact, for the front view, the output signals of the force sensors of different rows in each column are added together. Figure 5.b shows

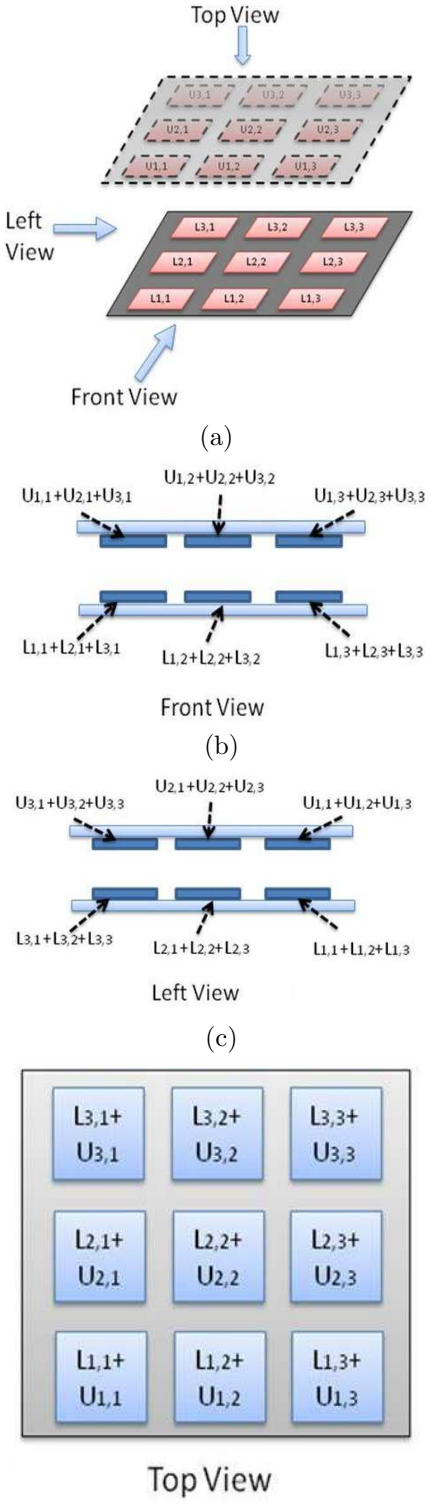

Figure 6.3: (a) Three views of the upper and lower sensor matrices (b) The output signals for the front view (c) The output signals for the left view (d) The output signals for the top view

the arrangement of output signals for the front view of the sensor. There are three outputs for each of the upper and lower matrices. Each output is the summation of three sensing elements located on the same column. For instance, the upper left output is the addition of signals from sensing elements $U1,1+U2,1+U3,1$ and the lower middle output is the addition of signals from $L1,2+L2,2+L3,2$.

Similarly, for the intensity display of the left view, the output signal of the force sensors of different columns in each row are added together, since the column in which a lump is located is not important (Fig. 6.3a). Figure.6.3c shows the output signals of the left view of the sensor. Here, similar to the front view, there are three outputs for each of the upper and lower sensors. Each output is the summation of three sensing elements on the same row. For example, the upper left output is the addition of signals from sensing elements $U3,1+U3,2+U3,3$ and the lower middle output is the addition of signals from $L1,1+L1,2+L1,3$.

For the top view, on the other hand, both row and column of lumps are important. In this case the output signal of the force sensors of upper and lower sensing elements, located on the same row and column, are added together. Figure 6.3d shows the output signals of the top view of the sensor where there are a total of nine outputs. Each output is the addition of two sensing elements on the same row and column. For example, the upper left output is the addition of signals from sensing elements $L3,1+U3,1$ and the lower middle output is the addition of signals from $L1,2+U1,2$.

Since there are nine outputs here, it is not possible to use the two-dimensional algorithm. In fact, an extended version of that algorithm is needed in this case. In the extended version, the 2D algorithm is used twice. First, an intensity display is calculated for the sensing elements of the first and second row. Another display is calculated for the sensing elements of the second and third rows. Finally the two displays are added together and a complete display is provided.

The corresponding matrix of output voltages is in the following form

$$\boldsymbol{V} = \begin{bmatrix} V_{U3,1} + V_{L3,1} & V_{U3,2} + V_{L3,2} & V_{U3,3} + V_{L3,3} \\ V_{U2,1} + V_{L2,1} & V_{U2,2} + V_{L2,2} & V_{U2,3} + V_{L2,3} \\ V_{U1,1} + V_{L1,1} & V_{U1,2} + V_{L1,2} & V_{U1,3} + V_{L1,3} \end{bmatrix} \tag{6.3.1}$$

This 3×3 matrix is divided into two 2×3 matrices as below:

$$\boldsymbol{V_1} = \begin{bmatrix} V_{U3,1} + V_{L3,1} & V_{U3,2} + V_{L3,2} & V_{U3,3} + V_{L3,3} \\ V_{U2,1} + V_{L2,1} & V_{U2,2} + V_{L2,2} & V_{U2,3} + V_{L2,3} \end{bmatrix} \tag{6.3.2}$$

and

$$\boldsymbol{V_2} = \begin{bmatrix} V_{U2,1} + V_{L2,1} & V_{U2,2} + V_{L2,2} & V_{U2,3} + V_{L2,3} \\ V_{U1,1} + V_{L1,1} & V_{U1,2} + V_{L1,2} & V_{U1,3} + V_{L1,3} \end{bmatrix} \tag{6.3.3}$$

$\boldsymbol{H1}$ and $\boldsymbol{H2}$, which are $M \times N$ matrices, can be calculated from $\boldsymbol{V1}$ and $\boldsymbol{V2}$ by using the relationship in eq.(.2.6). Matrix $\boldsymbol{H}$, which is the intensity distribution matrix for $\boldsymbol{V}$, is calculated as

$$\boldsymbol{H} = \begin{bmatrix} \boldsymbol{H_1} \\ \boldsymbol{H_2} \end{bmatrix} \tag{6.3.4}$$

Figure 6.4d shows an artery that is located at the front-right of an elastomers sample. Figures 6.4a, 6.4b, and 6.4c show the intensity displays calculated for the front view,

left view and top view of the sample. The location of the lump can be confirmed by comparing these three views.

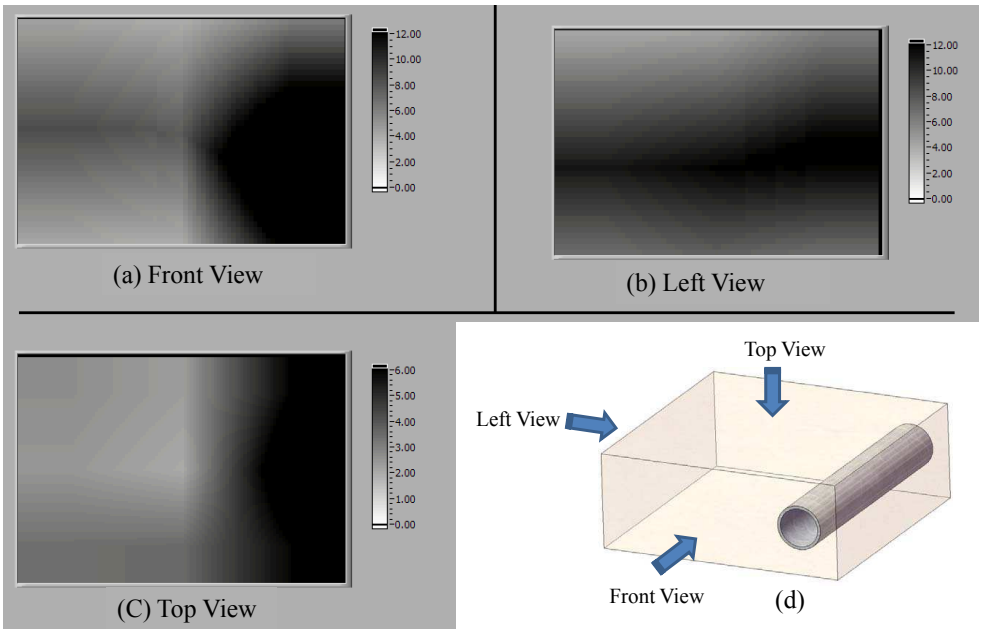

Figure 6.4: A lump located at the front-right of an elastomer sample and its 3D tactile image

6.4 Experiments

An experimental setup was used to generate graphical tactile information. The setup includes an ElectroForce 3200 BOSE device for applying dynamic and statics loads to simulated soft tissue containing artery and cancerous lump. Two elastomers, B1 and ICF400, with different stiffness were selected as the simulated tissue. To behave in a similar way to biological tissues, the elastomers were selected among those materials that undergo large deformation. The elastomers also were modelled

as hyperelastic materials in the FE modeling. The matrices of the force sensor were positioned between the jaws of the BOSE device. The elastomer containing the embedded lump or artery was sandwiched between two matrices of the force sensors. Plastic balls and soft plastic tubes with known Young's modulus were used as lump and artery, as shown in Fig. 6.2c. To change the depth of lumps and artery inside the elastomers, several layers of elastomers were cut into the same dimensions, but with different thicknesses. Lumps or arteries were placed inside one of the layers. A dynamic load was applied by the BOSE device to the jaws, and to the elastomers. The output of the sensors was fed into the buffer circuit, to DAQ (NI PCI 6225), and to the developed algorithm in the LabView software to localize the place of the artery and the lump in three dimensions. A low-pass filter with a cutoff frequency of $40Hz$ was used to remove the $60Hz$ line noise. Another experimental setup was used to acquire the stress-strain curve of the two selected elastomers in a uniaxial compression test by using a BOSE device. The compression test caused a displacement of $5.5mm$ in both samples. The accuracy of the BOSE device in displacement measurement is $0.01mm$, and in force measurement is $0.01N$. The obtained data for the stress-strain were used to model the elastomers as hyperelastic materials in the FEA.

elastomers	C_{10}	C_{01}	C_{11}
B1	-129700	173670	55812
ICF	-8598.8	10284	5143.6

Table 6.1: Constants of the three parameter Mooney-Rivlin model

6.5 FE Modeling

Different FE models were developed to analyze the validity of the output of the 3D graphical display. The soft tissue, the lump, and the artery were all considered as isotropic elastic materials. The Young's modulus of the lump and the artery were considered to be $18KPa$ and $130KPa$ respectively [141–145]. The stress-strain relation of B1 and ICF elastomers were found in compression tests using the BOSE device for modeling the elastomers as incompressible hyperelastic materials. Concepts for nonlinear stress-strain behavior of hyperelastic materials can be found in [114–116]. The values of constants and the method of experiments are already discussed in Chapter 3. The compressive stress-strain curve for the two elastomers and the fitted Mooney-Rivlin models are shown in Fig. 3.8, from which it can be seen that the third order Mooney-Rivlin model fits best to the experimental data for both elastomers.

The Mooney-Rivlin Constants for B1-A and ICF are shown in Table 6.1. The radius of the lump was selected to be $5mm$, while the inside radius of the artery was selected to be $4mm$ with a wall thickness of $0.6mm$ [146]. The tissue was modelled in ANSYS by using 3D, 10 node tetrahedral elements, which is suitable for hyperelastic

materials. Modeling of the embedded lump and the artery inside the tissue was performed in two sections: the lump with the tissue, and the artery with the tissue. The applied load to the tissue was considered in the form of displacement in the modeling due to the same situation in real operations.

The pressure distribution in the upper and the lower surface of the tissue which comes into contact with the sensors was plotted. In addition to the explained model, another model was developed for the artery and the tissue. In this model, blood pressure was considered to exist inside the artery, with and without application of displacement to the tissue. The aim of this modeling was to see if the sensors can also localize the artery only with the existing heart pressure pulse. The blood pressure inside the artery replicated a pulse having a minimum and maximum pressure of 80 and 120$mmHg$. The cross section of the pressure distribution of both lump and artery models is shown in Fig. 6.5.

6.6 Results and Discussion

Different lengths and combinations of arteries and lumps were embedded inside the tissue and tested by the developed 3D display. In the experimental tests, there was no pressure inside the arteries. Instead, arteries were selected from harder materials to have more stiffness compared with tissue. The output of the developed program in LabView in the 3D display is shown in Fig. 6.4a, 6.4b, and 6.4c. Fig. 6.4d shows

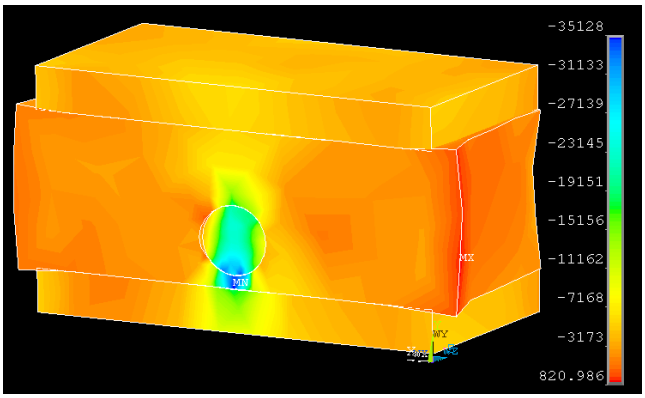

(a)

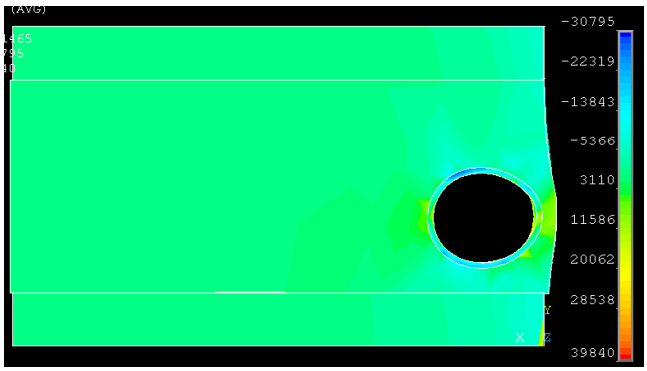

(b)

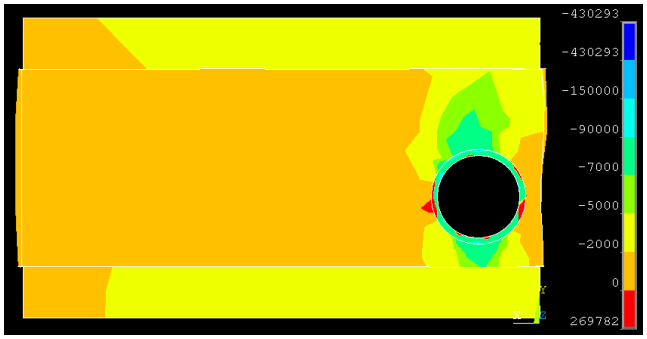

(c)

Figure 6.5: Cross section of the FEM of the embedded lump and artery inside tissue (a) Embedded lump inside the tissue, ICF elastomer, while applying $1mm$ displacement to the upper and the lower jaws (b) The embedded artery inside tissue, B1 elastomer, while having only $12mmHg$ pressures in the artery (c) The embedded artery inside tissue, ICF elastomer, while applying $1mm$ displacement to the upper and the lower jaws, and having $8mmHg$ pressure in the artery

the 3D schematic of the tissue and the embedded artery inside. As can be seen, the display shows the three main engineering views (front, top, and left) of the tissue with the embedded artery. The tissue is placed between the two force sensor matrices. The system is capable of measuring in both dynamic and static modes which makes it suitable for showing these objects while a surgical operation is being performed.

The same configuration of Fig. 6.4d was modelled by FEM using ICF elastomer. The pressure distribution on the upper and the lower surface is shown in Fig. 6.6. In the upper and lower surfaces of the tissue, more pressure is applied to the places with an artery inside. More details about the 2D pressure distribution can be found in [139]. As can be seen from both Figures 6.4 and 6.6, when the location of an artery or a lump becomes closer to the upper or the lower surface of the tissue, the pressure is increased at that surface as opposed to the other. This difference in the upper and the lower pressure map can also be seen from the results of the 3D display which shows that the sensors have enough sensitivity to detect different variations of stiffness in the tissue. The coefficient of friction between the upper/lower surface of the tissue and the grasper was set to 0.6 [121]. Figure 6.7 shows different results for the experiments of embedded lumps and arteries inside tissue. These configurations may not exist in reality; however, they have been tested to verify the ability of the 3D display in localizing different objects inside the tissue. From Fig. 6.7c, it can be seen that the artery completely covers sensors $L1,2$ and $L1,3$, but sensor $L1,1$ is only

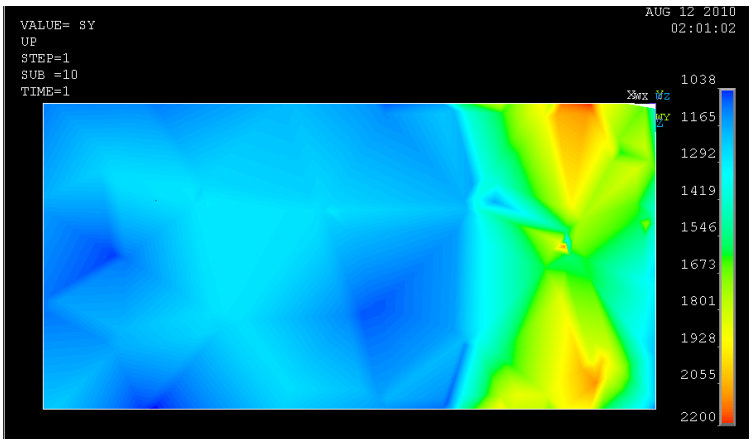

(a)

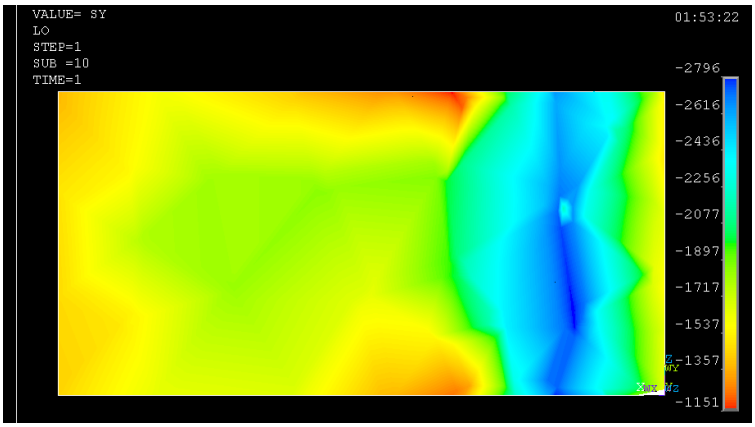

(b)

Figure 6.6: Cross section of the FEM of the embedded lump and artery inside tissue (a) Embedded lump inside the tissue, ICF elastomer, while applying $1mm$ displacement to the upper and the lower jaws (b) The embedded artery inside tissue, B1 elastomer, while having only $12mmHg$ pressures in the artery (c) The embedded artery inside tissue, ICF elastomer, while applying $1mm$ displacement to the upper and the lower jaws, and having $8mmHg$ pressure in the artery

half-covered. Therefore, sensor $L1,1$ shows less force amplitude in comparison with sensors $L1,2$ and $L1,3$ both of which result in the same 3D display. Since surgeons

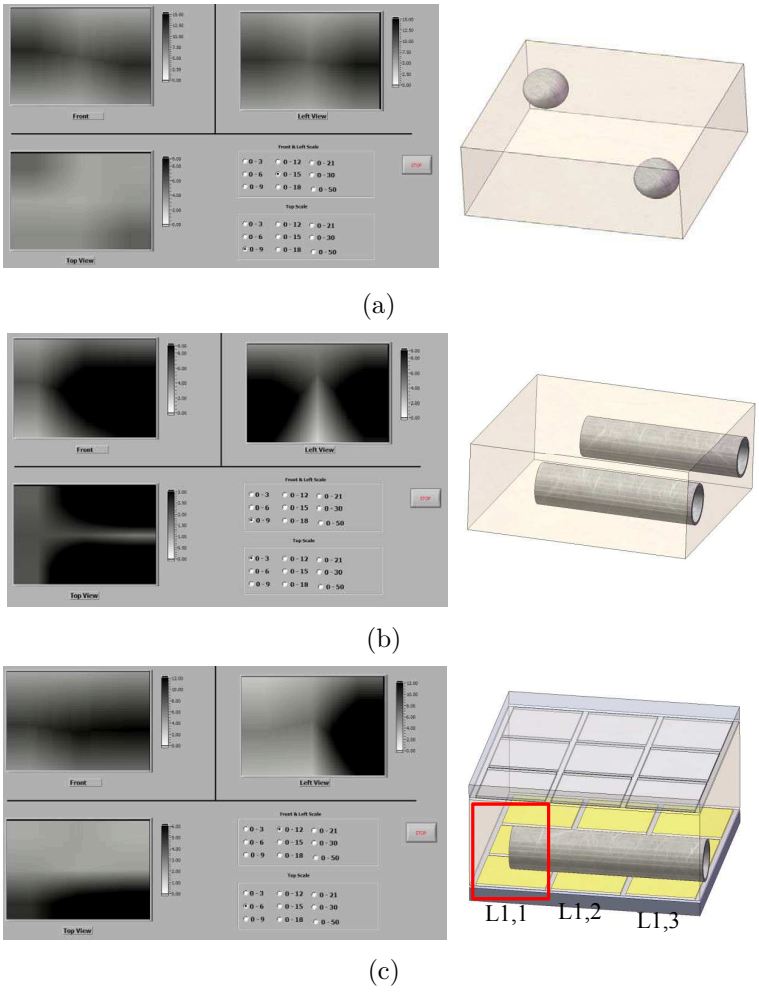

Figure 6.7: Results of the 3D software for different configurations (a) Two embedded lump inside the tissue (b) Two embedded artery inside tissue (c) One embedded artery inside tissue and the position of the upper and the lower sensor matrixes according to the position of the artery

are the end-user of the 3D display technique, the three individual 2D engineering drawings of lumps and arteries can be changed to only one 3D image of the tissue

including lumps or arteries. This conversion to 3D makes it easier for surgeons to visualize the objects inside tissues. Hence, the three individual drawing were sent to CATIA software to recreate one 3D image. Figure 6.8 shows the created 3D image in CATIA. Although the recreated 3D image is not exactly the same as actual configuration of lumps or arteries, but it can show the location of the embedded lumps and arteries. By increasing the number of sensors, the resolution of the created image can be improved and the image can become more close to the actual situation. The future work is to increase the number of sensing elements to increase the accuracy of the created 3D image. In addition, facilitating the view of the 3D image in the LabView software is beneficial, as in this case there is no need to write a code between different software to connect them together which results in lower speed in real-time viewing of the 3D image.

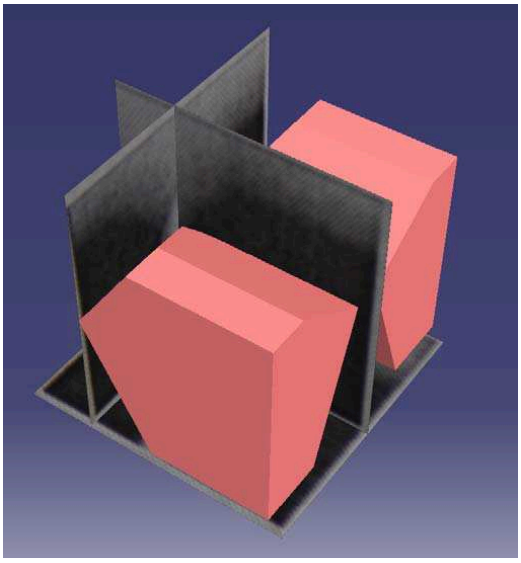

(a)

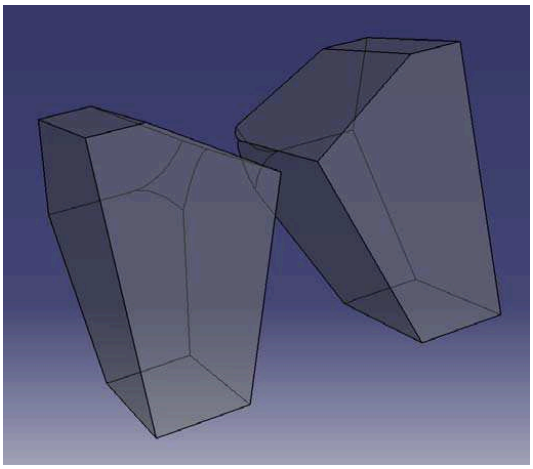

(b)

Figure 6.8: Results of the 3D Image (a) Location inside the tissue (b) Recreation of the two arteries in a 3D image

Chapter 7

summary and conclusions

7.1 Conclusions

In this thesis, a novel formulation was developed for modeling the behaviour of electrical resistivity of semiconductive polymer composites on an applied load. The proposed formulation, in Chapter 2, includes a viscoelastic model that shows the creep behavior of semiconductive polymer composites. Moreover, the contact resistance is also included in the proposed formulation. Although contact resistance is not a large factor at high resistances, it turns out that it has a significant effect in the lower range of resistance. This is very important given the fact that the working range of the sensor needs to be accurate from $0.5N$ to $5N$.

Linqstat as a semiconductive polymer composite was selected to verify the validity

of the proposed formulation by means of experiments. Creep tests were performed on Linqstat samples and the viscoelastic parameters were determined. In addition, by using Linqstat, an accurate force sensor was fabricated; and the results obtained from the formulas corresponded very closely to the actual output readings from the sensors.

By using the principle of the developed force sensor with Linqstat, an innovative tactile sensor was designed, fabricated, simulated, and tested for use in both CBT and MIS in Chapter 3. The experimental tests results of the study confirmed that the tactile sensor successfully characterized seven elastomers. Such elastomers resemble different biological tissues with different degrees of hardness involved in surgical operations. For instance, among those seven materials, the hard ones could be a tumorous lump, an artery, or a ureter surrounded by a background tissue; whereas the soft ones could be the background tissue. As another example, the hard materials could be mitral annulus tissue while the soft ones could be mitral leaflet tissue or left atrial tissue.

The sensor was used to detect the differences in the hardness degree for different elastomers. In order to validate the performance of the sensor, its output was compared to the results of three different techniques as follow: (1) FEA of the interaction between the sensor and elastomers; (2) Hardness measurement of the same elastomers

with a durometer device; and (3) a psychophysical test of relative hardness measurement for the same materials. In the first technique, compression tests were conducted on the elastomers to obtain their stress-strain information. The test data was used to develop a FE model of the materials based on a three-parameter Mooney-Rivlin hyperelastic model. These models were used to simulate the interaction between the sensor and the elastomers. In the second technique, the hardness of the elastomers was tested by a standard durometer device. In the third technique, a group of twenty students from the faculty of engineering at Concordia University were asked to report their tactile perception on the degrees of hardness, relatively, for the same materials. The comparison between the output of the sensor and the results of three techniques validates the design concept and the performance of the sensor.

In the literature, most of the sensors developed for MIS have either complicated designs or incompatible configurations to be used in CBT. However, the present sensor offers various key features that enhance its performance for use in both MIS and CBT applications. Such key features of the sensor are its ability to perform such measurements with the following characteristics: (1) it consists of a flexible design with single solid piece without any moving parts; (2) it performs under both static and dynamic loading conditions; and (3) it can easily be micro-fabricated due to the simple design of the sensor.

The first innovative feature of the sensor eliminates the risk of physical damage

to the sensor before and during the surgical operations. In other words, the single solid piece of the sensor tolerates excessive forces that might be applied to the sensor unintentionally. In the mean time, the circular configuration of the sensor facilitates its integration with the narrow spaces available at the tips of surgical catheters. Furthermore, the external shape of the tactile sensor can be also reconfigured to square shape, without any change in the principle of the sensing mechanism. This flexibility in the shape of the sensor allows it to be fabricated on the jaws of a surgical grasper in MIS. Hence, the developed sensor can be used in both MIS and CBT applications for the palpation of tissues. In addition, the tactile sensor can be fabricated on robotic manipulators and end-effectors for other purposes, e.g. teletouch applications.

The second feature of the sensor helps surgeons to maintain a stable contact between the tips of catheters and tissues. The third feature of the sensor allows the cost-effective batch production of the sensor in a miniaturized scale. As the tactile sensor is composed of a piezoresistive layer and a filler plate, they both can be cut into small pieces by using accurate laser cutting technology; and be assembled by micro-manipulators. Moreover, the piezoresistive-based sensing principle of the sensor provides a low noise signal, which requires a simple signal processing for the hardness measurements.

After development of the tactile sensor, the interaction of the tactile sensor with soft tissues was investigated in Chapter 4. A novel contact model was developed

for the interaction between developed tactile sensor and viscoelastic tissue. Several in-vitro DMA tests were conducted on the tissue to extract the coefficients of the viscoelastic model for the atrial tissue of swine heart. The complex compliance of the atrial tissue was determined with DMA method for harmonic loading conditions, starting from 1 Hz to 36 Hz. Using a genetic algorithm, the 17 constants of the viscoelastic model of the tissue were obtained. The viscoelastic model of the atrial tissue could successfully replicate the response of the tissue under dynamic loading conditions.

The tissue model data were entered in the contact model; the relation between the indentation displacement, the ratio of the radii, time, and the applied force were established. The contact model has several applications, e.g, in selecting the optimum dimensions of the tactile sensor and surgical catheters, and in simulating the real-time tissue interaction with catheters in surgical simulators for training purposes. As the contact model is based on parametric representation, the simulation of the tissue behaviour is much faster and simpler when compared to other modeling techniques such as FEA. In addition, under quasi-static loading conditions, a dynamic load was applied to the tissue and the response of the tissue was simulated in real-time. It was shown that the model can replicate the quasi-static behaviour of the tissue to the applied load as well as the creep effect for a constant load.

The new idea of recording time during touch was also provided in the form of a new

array tactile sensor in Chapter 5. The array tactile sensor was designed, developed, and fabricated for use in MIS. A new algorithm was also developed to run the array sensor. In the array sensor, force, displacement, and displacement rate were also measured during touch. It was shown that the new sensor can differentiate between the hardness degree of soft tissues with viscoelastic behaviour. The change in the force-displacement response of the tissue for different displacement rate application validated the design concept of the new array tactile sensor. These changes in force-displacement value showed that there is a need to measure the displacement rate while conducting touch with the sensor to the tissue.

In the second section of the thesis, the piezoresistive force sensors were used in a matrix form for artery and tumour localization in MIS. In the proposed system, using the piezoresistive force matrix, any lumps or masses within tissue were detected, located, features extracted, and visually displayed. The utilized sensor matrix were associated with a new approach for the graphical display of lumps and inclusions embedded in a soft object. The displayed images are easily recognizable by the surgeon. When an array of these sensors is placed in one jaw of the endoscopic grasper, the location of the lump along the grasper can be detected and displayed. By using sensor matrices in both the upper and lower jaws of the grasper, it is possible to find and graphically represent inclusions in the grasped object in three dimensions. Therefore, using the proposed system, surgeons can detect the presence or absence

of a lump and obtain useful information on its size and location by simply grasping the target organ with the smart endoscopic grasper and view the resulting processed information on a visual display.

7.2 Contributions

This thesis presents some studies and development on the use of tactile sensors and graphical displays in surgical applications. The contribution of the theses can be classified as below:

1. A new approach is proposed for parametric modeling of piezoresistive force sensors based on polymer composite materials. Electrical contact and creep behaviour of Linqstat is modelled and implemented in the parametric model.

2. By development of a novel piezoresistive tactile sensor, a new method is proposed for softness/hardness feedback from surgical catheter.

3. It is shown that the developed miniaturized sensor is capable of hardness measurement under different loads and frequencies.

4. Nonlinear hyper elastic model of several tissues is developed for the sensor performance validation.

5. A viscoelastic model is developed for atrial tissue of porcine heart by using

DMA method and a GA code.

6. The viscoelastic contact between tissue and tactile sensor, or a possible catheter, is developed parametrically.

7. A new generation of array tactile sensors was developed, which measures the displacement rate during the touch for tissues vis viscoelastic behaviour.

8. A novel technique is developed for 3D graphical rendering of tactile information to surgeons. The graphical display is capable of rendering any inclusions inside the tissue such as lumps or artery.

Some of the original contributions are already published as conference papers [89, 90, 94] and journal articles [87, 88, 91, 93].

7.3 Future Works

An array of micro-fabricated version of the proposed tactile sensor is proposed to be integrated into the tip of a catheter. This project is currently under investigation in our laboratory. In real surgical setup, the middle part of the catheter should be reserved for the anchoring system of the mitral valve. Furthermore, the output signal from only one sensor on the tip of a catheter is not enough for localizing and positioning the mitral annulus from its surrounding tissues. Hence, more tactile sensors may be used for comparing their output signals together to localize the hardest

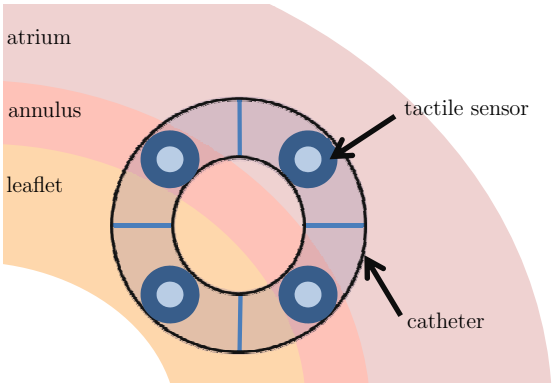

Figure 7.1: Localizing the position of mitral annulus by comparing the output of the tactile sensors on the tip of catheter

tissue, annulus. In the next step, several tactile sensors, at least four, should be fabricated on the extremity of the catheter circumferentially as shown in Fig. 7.1. Then, each of the sensors would have different output signal by establishing a suitable contact between the catheter tip and heart tissue. By graphical rendering of the difference in the relative hardness, the surgeon can localize the position of the mitral annulus. The graphical interface for the sensors is already developed. The future work is to miniaturize the sensors and to integrate them into the extremity of the catheter, followed by clinical tests.

Bibliography

[1] Camarillo, D., Krummel, T., Salisbury, J., et al., 2004. "Robotic technology in surgery: past, present, and future". *The American Journal of Surgery,* ***188***, pp. 2–15.

[2] Bicchi, A., Canepa, G., De Rossi, D., Iacconi, P., and Scillingo, E., 1996. "A sensor-based minimally invasive surgery tool for detecting tissue elastic properties". In IEEE 1996 International Conference on Robotics and Automation Proceedings, Vol. 1, IEEE Press, pp. 884–888.

[3] Dargahi, J., and Najarian, S., 2005. "Advances in tactile sensors design/manufacturing and its impact on robotics applications–a review". *Industrial Robot: An International Journal,* ***32***(3), pp. 268–281.

[4] King, C., Culjat, M., Franco, M., Bisley, J., Carman, G., Dutson, E., and Grundfest, W., 2009. "A multielement tactile feedback system for robot-assisted minimally invasive surgery". *IEEE Transaction on Haptics,* ***2***, pp. 52–56.

[5] Kane, B., Cutkosky, M., and Kovacs, G., 1996. "Cmos-compatible traction stress sensor for use in high-resolution tactile imaging". *Sensors and Actuators A: Physical,* ***54***(1–3), pp. 511–516.

[6] Omata, S., Murayama, Y., and Constantinou, C., 2004. "Real time robotic tactile sensor system for the determination of the physical properties of biomaterials". *Sensors and Actuators A: Physical,* ***112***(2-3), pp. 278–285.

[7] Padala, M., Sacks, M., Liou, S., Balachandran, K., He, Z., and Yoganathan, A., 2010. "Mechanics of the mitral valve strut chordae insertion region". *ASME Journal of Biomechanical Engineering,* ***132***(8), pp. 081004–0810013.

[8] Azar, T., Rajagopalan, S., Cecere, R., Kovecses, J., and Angeles, J., 2008. "A concept for a novel procedure for mitral valve repair by percutaneous annuloplasty". In ASME 3rd Frontiers in Biomedical Devices Conference & Exhibition, Vol. 2008, pp. 33–34.

[9] Cecere, R., and Azar, T., 2010. Instrument including a movement sensor and method of using same, Dec. 17. US Patent App. 12/926,915.

[10] Fundaro, P., Tartara, P., Villa, E., Fratto, P., Campisi, S., and Vitali, E., 2007. "Mitral valve repair: Is there still a place for suture annuloplasty?". *Asian Cardiovascular & Thoracic Annals,* ***15***(4), pp. 351–358.

[11] Misra, S., Ramesh, K., and Okamura, A., 2008. "Modeling of tool-tissue interactions for computer-based surgical simulation: a literature review". *Presence: Teleoperators and Virtual Environments,* ***17***(5), pp. 463–491.

[12] Fearing, R., Moy, G., and Tan, E., 1997. "Some basic issues in teletaction". In 1997 IEEE International Conference on Robotics and Automation Proceedings, Vol. 4, IEEE, pp. 3093–3099.

[13] Eklund, A., Bergh, A., and Lindahl, O., 1999. "A catheter tactile sensor for measuring hardness of soft tissue: measurement in a silicone model and in anin vitro human prostate model". *Medical and Biological Engineering and Computing,* ***37***(5), pp. 618–624.

[14] Miyaji, K., Furuse, A., Nakajima, J., Kohno, T., Ohtsuka, T., Yagyu, K., Oka, T., and Omata, S., 1997. "The stiffness of lymph nodes containing lung carcinoma metastases". *Cancer,* ***80***(10), pp. 1920–1925.

[15] Wolffenbuttel, M., and Regtien, P., 1991. "Polysilicon bridges for the realization of tactile sensors". *Sensors and Actuators A: Physical,* ***26***(1-3), pp. 257–264.

[16] Hu, N., Karube, Y., Yan, C., Masuda, Z., and Fukunaga, H., 2008. "Tunneling effect in a polymer/carbon nanotube nanocomposite strain sensor". *Acta Materialia,* ***56***(13), pp. 2929–2936.

[17] Knite, M., Teteris, V., Kiploka, A., and Kaupuzs, J., 2004. "Polyisoprene-carbon black nanocomposites as tensile strain and pressure sensor materials". *Sensors and Actuators A: Physical,* ***110***(1–3), pp. 142–149.

[18] Qu, S., and Wong, S., 2007. "Piezoresistive behavior of polymer reinforced by expanded graphite". *Composites science and technology,* ***67***(2), pp. 231–237.

[19] Wang, L., Ding, T., and Wang, P., 2008. "Effects of compression cycles and precompression pressure on the repeatability of piezoresistivity for carbon black-filled silicone rubber composite". *Journal of Polymer Science Part B: Polymer Physics,* ***46***(11), pp. 1050–1061.

[20] Mahmoud, W., El-Lawindy, A., El Eraki, M., and Hassan, H., 2007. "Butadiene acrylonitrile rubber loaded fast extrusion furnace black as a compressive strain and pressure sensors". *Sensors and Actuators A: Physical,* ***136***(1), pp. 229–233.

[21] Luheng, W., Tianhuai, D., and Peng, W., 2007. "Effects of conductive phase content on critical pressure of carbon black filled silicone rubber composite". *Sensors and Actuators A: Physical,* ***135***(2), pp. 587–592.

[22] Melchiorri, C., 2000. "Slip detection and control using tactile and force sensors". *IEEE/ASME Transactions on Mechatronics,* ***5***(3), pp. 235–243.

[23] Vanello, N., Hartwig, V., Tesconi, M., Ricciardi, E., Tognetti, A., Zupone, G., Gassert, R., Chapuis, D., Sgambelluri, N., Scilingo, E., et al., 2008. "Sensing glove for brain studies: Design and assessment of its compatibility for fmri with a robust test". *IEEE/ASME Transactions on Mechatronics,* ***13***(3), pp. 345–354.

[24] Kawasaki, H., Komatsu, T., and Uchiyama, K., 2002. "Dexterous anthropomorphic robot hand with distributed tactile sensor: Gifu hand ii". *IEEE/ASME Transactions on Mechatronics,* ***7***(3), pp. 296–303.

[25] Lin, L., and Huang, H., 1996. "Integrating fuzzy control of the dexterous national taiwan university (ntu) hand". *IEEE/ASME Transactions on Mechatronics,* ***1***(3), pp. 216–229.

[26] Nilsson, M., 2000. "Tactile sensors and other distributed sensors with minimal wiring complexity". *IEEE/ASME Transactions on Mechatronics,* ***5***(3), pp. 253–257.

[27] Tan, H., Slivovsky, L., and Pentland, A., 2001. "A sensing chair using pressure distribution sensors". *IEEE/ASME Transactions on Mechatronics,* ***6***(3), pp. 261–268.

[28] Lee, W., Son, J., Kang, N., Park, I., and Park, Y., 2009. "Finite-element analysis of deformation behaviors in random-whisker-reinforced composite". *Scripta Materialia,* ***61***(6), pp. 580–583.

[29] Ruschau, G., Yoshikawa, S., and Newnham, R., 1992. "Resistivities of conductive composites". *Journal of applied physics,* ***72***(3), pp. 953–959.

[30] Luheng, W., Tianhuai, D., and Peng, W., 2009. "Influence of carbon black concentration on piezoresistivity for carbon-black-filled silicone rubber composite". *Carbon,* ***47***(14), pp. 3151–3157.

[31] Xie, Z., Yum, Y., and Lee, C., 2007. "Simulation of electrical resistivity of carbon black filled rubber under elongation". *Journal of Macromolecular Science, Part B,* ***46***(3), pp. 561–567.

[32] Hall, R., Desmoulin, G., and Milner, T., 2008. "A technique for conditioning and calibrating force-sensing resistors for repeatable and reliable measurement of compressive force". *Journal of biomechanics,* ***41***(16), pp. 3492–3495.

[33] Zhang, X., Pan, Y., Zheng, Q., and Yi, X., 2000. "Time dependence of piezoresistance for the conductor-filled polymer composites". *Journal of Polymer Science Part B: Polymer Physics,* ***38***(21), pp. 2739–2749.

[34] Gillinov, A., and Liddicoat, J., 2006. "Percutaneous mitral valve repair". *Seminars in Thoracic and Cardiovascular Surgery,* ***18***(2), pp. 115–121.

[35] King, C., Culjat, M., Franco, M., Lewis, C., Dutson, E., Grundfest, W., and Bisley, J., 2009. "Tactile feedback induces reduced grasping force in robot-assisted surgery". *IEEE Transactions on Haptics,* ***2***(2), pp. 103–110.

[36] Puangmali, P., Althoefer, K., Seneviratne, L., Murphy, D., and Dasgupta, P., 2008. "State-of-the-art in force and tactile sensing for minimally invasive surgery". *IEEE Sensors Journal,* ***8***(4), pp. 371–381.

[37] Yokoyama, K., Nakagawa, H., Shah, D., Lambert, H., Leo, G., Aeby, N., Ikeda, A., Pitha, J., Sharma, T., Lazzara, R., et al., 2008. "Novel contact force sensor incorporated in irrigated radiofrequency ablation catheter predicts lesion size and incidence of steam pop and thrombus". *Circulation: Arrhythmia and Electrophysiology,* ***1***(5), p. 354.

[38] Yip, M., Yuen, S., and Howe, R., 2010. "A robust uniaxial force sensor for minimally invasive surgery". *IEEE Transactions on Biomedical Engineering,* ***57***(5), pp. 1008–1011.

[39] Polygerinos, P., Zbyszewski, D., Schaeffter, T., Razavi, R., Seneviratne, L., and Althoefer, K., 2010. "Mri-compatible fiber-optic force sensors for catheterization procedures". *IEEE Sensors Journal,* ***10***(10), pp. 1598–1608.

[40] Yuen, S., Yip, M., Vasilyev, N., Perrin, D., del Nido, P., and Howe, R., 2009. "Robotic force stabilization for beating heart intracardiac surgery". *Medical Image Computing and Computer-Assisted Intervention–MICCAI 2009*, pp. 26–33.

[41] Franco, M., King, C., Culjat, M., Lewis, C., Bisley, J., Holmes, E., Grundfest, W., and Dutson, E., 2009. "An integrated pneumatic tactile feedback actuator array for robotic surgery". *The International Journal of Medical Robotics and Computer Assisted Surgery,* ***5***(1), pp. 13–19.

[42] Yen, P., Chen, D., Yeh, K., and Chu, P., 2008. "Lateral exploration strategy for differentiating the stiffness ratio of an inclusion in soft tissue". *Medical engineering & physics,* ***30***(8), pp. 1013–1019.

[43] McCreery, G., Trejos, A., Naish, M., Patel, R., and Malthaner, R., 2008. "Feasibility of locating tumours in lung via kinaesthetic feedback". *The International Journal of Medical Robotics and Computer Assisted Surgery,* ***4***(1), pp. 58–68.

[44] Trejos, A., Jayender, J., Perri, M., Naish, M., Patel, R., and Malthaner, R., 2009. "Robot-assisted tactile sensing for minimally invasive tumor localization". *The International Journal of Robotics Research,* ***28***(9), p. 1118.

[45] Perri, M., Trejos, A., Naish, M., Patel, R., and Malthaner, R., 2010. "New tactile sensing system for minimally invasive surgical tumour localization". *The International Journal of Medical Robotics and Computer Assisted Surgery,* ***6***(2), pp. 211–220.

[46] Sokhanvar, S., Packirisamy, M., and Dargahi, J., 2007. "A multifunctional pvdf-based tactile sensor for minimally invasive surgery". *Smart Materials and Structures,* ***16***, p. 989.

[47] Sokhanvar, S., Packirisamy, M., and Dargahi, J., 2009. "Mems endoscopic tactile sensor: toward in-situ and in-vivo tissue softness characterization". *IEEE Sensors Journal,* ***9***(12), pp. 1679–1687.

[48] Schostek, S., Schurr, M., and Buess, G., 2009. "Review on aspects of artificial tactile feedback in laparoscopic surgery". *Medical engineering & physics,* ***31***(8), pp. 887–898.

[49] Jernigan, S., Buckner, G., Eischen, J., and Cormier, D., 2007. "Finite element modeling of the left atrium to facilitate the design of an endoscopic atrial retractor". *ASME Journal of Biomechanical Engineering,* ***129***(6), pp. 825–837.

[50] Greenwood, J., 2010. "Contact between an axisymmetric indenter and a viscoelastic half-space". *International Journal of Mechanical Sciences,* ***52***(6), pp. 829–835.

[51] Yamamoto, T., Vagvolgyi, B., Balaji, K., Whitcomb, L., and Okamura, A., 2009. "Tissue property estimation and graphical display for teleoperated robot-assisted surgery". In Proceedings of the 2009 IEEE international conference on Robotics and Automation, ICRA'09, IEEE Press, pp. 3117–3123.

[52] Mahvash, M., and Okamura, A. M., 2006. "Friction compensation for a force-feedback telerobotic system". In Proceedings of the 2006 IEEE international conference on Robotics and Automation, ICRA'06, IEEE Press, pp. 3268–3273.

[53] Doehring, T., Freed, A., Carew, E., and Vesely, I., 2005. "Fractional order viscoelasticity of the aortic valve cusp: An alternative to quasilinear viscoelasticity". *ASME Journal of Biomechanical Engineering,* ***127***(4), pp. 700–708.

[54] Kerdok, A., Ottensmeyer, M., and Howe, R., 2006. "Effects of perfusion on the viscoelastic characteristics of liver". *Journal of Biomechanics,* ***39***(12), pp. 2221–2231.

[55] Basafa, E., and Farahmand, F., 2010. "Real-time simulation of the nonlinear visco-elastic deformations of soft tissues". *International Journal of Computer Assisted Radiology and Surgery,* ***Online***, pp. 1–11.

[56] Berglund, J., Nerem, R., and Sambanis, A., 2005. "Viscoelastic testing methodologies for tissue engineered blood vessels". *ASME Journal of Biomechanical Engineering,* ***127***(7), pp. 1176–1184.

[57] Groth, K., and Granata, K., 2008. "The viscoelastic standard nonlinear solid model: Predicting the response of the lumbar intervertebral disk to low-frequency vibrations". *ASME Journal of Biomechanical Engineering,* ***130***(3), pp. 031005–031011.

[58] Nedel, L., and Thalmann, D., 1998. "Real time muscle deformations using mass-spring systems". In Proceedings of the Computer Graphics International 1998, CGI '98, IEEE Computer Society, pp. 156–166.

[59] Brown, J., 2004. "Real-time soft tissue and suture simulation". PhD thesis, Computer Science Department, Stanford, CA,. AAI3111693.

[60] Un, K., and Spilker, R., 2006. "A penetration-based finite element method for hyperelastic 3d biphasic tissues in contact. part ii: Finite element simulations". *ASME Journal of Biomechanical Engineering,* ***128***(6), pp. 934–942.

[61] Saupin, G., Duriez, C., and Cotin, S., 2008. "Contact model for haptic medical simulations". In Proceedings of the 4th International Symposium on Biomedical Simulation, ISBMS '08, Springer-Verlag, pp. 157–165.

[62] DiMaio, S., and Salcudean, S., 2005. "Interactive simulation of needle insertion models". *IEEE Transactions on Biomedical Engineering,* ***52***(7), pp. 1167–1179.

[63] Mendoza, C., and Laugier, C., 2003. "Simulating soft tissue cutting using finite element models". In Proceedings of 2003 IEEE International Conference on Robotics and Automation, Vol. 1 of *ICRA'03*, IEEE Press, pp. 1109–1114.

[64] Yang, T., and Spilker, R., 2007. "A lagrange multiplier mixed finite element formulation for three-dimensional contact of biphasic tissues". *ASME Journal of Biomechanical Engineering,* ***129***(3), pp. 457–471.

[65] Hirota, G., Fisher, S., and State, A., 2003. "An improved finite-element contact model for anatomical simulations". *The Visual Computer,* ***19***, pp. 291–309.

[66] Eberhardt, A., Lewis, J., and Keer, L., 1991. "Normal contact of elastic spheres with two elastic layers as a model of joint articulation". *ASME Journal of Biomechanical Engineering,* ***13***, pp. 410–417.

[67] Ateshian, G., Lai, W., Zhu, W., and Mow, V., 1994. "An asymptotic solution for the contact of two biphasic cartilage layers". *Journal of Biomechanics,* ***27***(11), pp. 1347–1360.

[68] Argatov, I., and Mishuris, G., 2011. "Elliptical contact of thin biphasic cartilage layers: Exact solution for monotonic loading". *Journal of Biomechanics,* ***44***, pp. 759–761.

[69] Giannakopoulos, A., 2006. "Elastic and viscoelastic indentation of flat surfaces by pyramid indentors". *Journal of the Mechanics and Physics of Solids,* ***54***(7), pp. 1305–1332.

[70] Vandamme, M., and Ulm, F., 2006. "Viscoelastic solutions for conical indentation". *International Journal of Solids and Structures,* ***43***(10), pp. 3142–3165.

[71] Barber, J., 1976. "Indentation of the semi-infinite elastic solid by a concave rigid punch". *Journal of Elasticity,* ***6***, pp. 149–159.

[72] Haider, M., and Guilak, F., 2000. "An axisymmetric boundary integral model for incompressible linear viscoelasticity: Application to the micropipette aspiration contact problem". *ASME Journal of Biomechanical Engineering,* ***122***(3), pp. 236–244.

[73] Romano, J., Hsiao, K., Niemeyer, G., Chitta, S., and Kuchenbecker, K., 2011. "Human-inspired robotic grasp control with tactile sensing". *IEEE Transactions on Robotics*(99), pp. 1–13.

[74] Ataollahi, A., Polygerinos, P., Puangmali, P., Seneviratne, L., and Althoefer, K., 2010. "Tactile sensor array using prismatic-tip optical fibers for dexterous robotic hands". In 2010 IEEE/RSJ International Conference on Intelligent Robots and Systems (IROS), IEEE, pp. 910–915.

[75] Dahiya, R., Cattin, D., Adami, A., Collini, C., Barboni, L., Valle, M., Lorenzelli, L., Oboe, R., Metta, G., and Brunetti, F., 2011. "Towards tactile sensing system on chip for robotic applications". *Sensors Journal, IEEE,* ***11***(12), dec., pp. 3216–3226.

[76] Aoyagi, S., Matsuda, T., Kong, T.-W., Ishimaru, T., Suzuki, M., and Inoue, K., 2011. "Proposal and development of arrayed sole sensor for legged robot and contact force detection using neural networks". *IEEE Sensors Journal,* ***11***(9), sept., pp. 2048–2056.

[77] Dahiya, R., Metta, G., Valle, M., and Sandini, G., 2010. "Tactile sensing—from humans to humanoids". *Robotics, IEEE Transactions on,* ***26***(1), feb., pp. 1–20.

[78] Tiwana, M. I., Redmond, S. J., and Lovell, N. H., 2012. "A review of tactile sensing technologies with applications in biomedical engineering". *Sensors and Actuators A: Physical,* ***Accepted Manuscript***(0), pp. –.

[79] Kuebler, B., Gruber, R., Joppek, C., Port, J., Passig, G., Nagel, J., and Hirzinger, G., 2009. "Tactile feedback for artery detection in minimally invasive robotic surgery–preliminary results of a new approach". In World Congress on Medical Physics and Biomedical Engineering, September 7-12, 2009, Munich, Germany, Springer, pp. 299–302.

[80] Miller, A., Peine, W., Son, J., and Hammoud, Z., 2007. "Tactile imaging system for localizing lung nodules during video assisted thoracoscopic surgery". In 2007 IEEE International Conference on Robotics and Automation, IEEE Press, pp. 2996–3001.

[81] Plunkett, M., Peterson, M., Landreneau, R., Ferson, P., and Posner, M., 1992. "Peripheral pulmonary nodules: preoperative percutaneous needle localization with ct guidance.". *Radiology,* ***185***(1), p. 274.

[82] Kawahara, T., Toya, C., Tanaka, N., Kaneko, M., Miyata, Y., Okajima, M., and Asahara, T., 2006. "Non-contact impedance imager with phase differentiator". In The First IEEE/RAS-EMBS International Conference on Biomedical Robotics and Biomechatronics, BioRob 2006, IEEE, pp. 232–237.

[83] Peine, W., 1999. "Remote palpation instruments for minimally invasive surgery". PhD thesis, Division of Engineering and Applied Sciences, Harvard University.

[84] Dargahi, J., and Najarian, S., 2004. "Theoretical and experimental analysis of a piezoelectric tactile sensor for use in endoscopic surgery". *Sensor Review,* ***24***(1), pp. 74–83.

[85] Dargahi, J., Kahrizi, M., Rao, N., and Sokhanvar, S., 2006. "Design and microfabrication of a hybrid piezoelectric-capacitive tactile sensor". *Sensor Review,* ***26***(3), pp. 186–192.

[86] Takashima, K., Yoshinaka, K., Okazaki, T., and Ikeuchi, K., 2005. "An endoscopic tactile sensor for low invasive surgery". *Sensors and Actuators A: Physical,* ***119***(2), pp. 372–383.

[87] Kalantari, M., Dargahi, J., Kovecses, J., Mardasi, M., and Nouri, S., 2011. "A new approach for modeling piezoresistive force sensors based on semiconductive polymer composites". *IEEE/ASME Transactions on Mechatronics,* ***17***(03), pp. 572–581.

[88] Kalantari, M., Ramezanifard, M., Ahmadi, R., Dargahi, J., and Kövecses, J., 2011. "A piezoresistive tactile sensor for relative tissue characterization during catheter-based cardiac surgery". *International Journal of Medical Robotics and Computer Assisted Surgery,* ***7***(4), pp. 431–440.

[89] Kalantari, M., Ramezanifard, M., Ahmadi, R., Dargahi, J., and Kövecses, J., 2010. "Design, fabrication, and testing of a piezoresistive hardness sensor in minimally invasive surgery". In Proceedings of IEEE Haptics Symposium, Boston, USA, March 2010, pp. 431–437.

[90] Kalantari, M., Shen, J. J., Dargahi, J., Kovecses, J., and Zadeh, M., 2011. "Localization of annulus with a tactile sensor". In 2011 IEEE 37th Annual Northeast Bioengineering Conference (NEBEC), pp. 1–2.

[91] Shen, J., Kalantari, M., Kövecses, J., Angeles, J., and Dargahi, J., 2011. "Viscoelastic modelling of the contact interaction between a tactile sensor and atrial tissue". *IEEE Transactions on Biomedical Engineering,* ***59***(6), pp. 1727–1738.

[92] Shen, J., Kalantari, M., Kövecses, J., Angeles, J., and Dargahi, J., 2011. "Measuring the properties of heart tissue with dynamic mechanical analysis method". In Proceedings of the 2011 CCToMM Symposium on Mechanisms, Machines, and Mechatronics (2011 CCToMM M3), Montral, Qubec, Canada.

[93] Kalantari, M., Ramezanifard, M., Dargahi, J., and Kovecses, J., 2011. "3d graphical rendering of localized lumps and arteries for robotic assisted mis". *Journal of Medical Devices,* ***5***(2), p. 021002.

[94] Kalantari, M., Ramezanifard, M., Ahmadi, R., Kövecses, J., and Dargahi, J., 2010. "2d lump/artery detection by using piezoresistive force sensors". In ASME's 2010 5th Frontiers in Biomedical Devices Conference & Exhibition, ASME Press.

[95] Ohe, K., and Naito, Y., 1971. "Piezoresistance effect of graphite-papostor". *Japanese Journal of Applied Physics,* ***10***(7), pp. 868–872.

[96] Simmons, J., 1963. "Generalized formula for the electric tunnel effect between similar electrodes separated by a thin insulating film". *Journal of Applied Physics,* ***34***(6), pp. 1793–1803.

[97] Zhang, X., Pan, Y., Zheng, Q., and Yi, X., 2001. "Piezoresistance of conductor filled insulator composites". *Polymer international,* ***50***(2), pp. 229–236.

[98] Wu, S., 1985. "Phase structure and adhesion in polymer blends: a criterion for rubber toughening". *Polymer,* ***26***(12), pp. 1855–1863.

[99] Holm, R., 1967. *Electric Contacts: Theory and Applications*. Springer Verlag, Berlin.

[100] Constable, J., 2006. "Analysis of the constriction resistance in an acf bond". *IEEE Transactions on Components and Packaging Technologies,* ***29***(3), pp. 494–501.

[101] Jackson, R., Malucci, R., Angadi, S., and Polchow, J., 2009. "A simplified model of multiscale electrical contact resistance and comparison to existing closed form models". In Proceedings of the 55th IEEE Holm Conference on Electrical Contacts, IEEE Press, pp. 28–35.

[102] Coutu, R., Reid, J., Cortez, R., Strawser, R., and Kladitis, P., 2006. "Microswitches with sputtered au, aupd, au-on-aupt, and auptcu alloy electric contacts". *IEEE Transactions on Components and Packaging Technologies,* ***29***(2), pp. 341–349.

[103] Brinson, H., and Brinson, L., 2008. *Polymer Engineering Science and Viscoelasticity: an Introduction*. Springer-Verlag, New York.

[104] Govindarajan, S., Langrana, N., and Weng, G., 1996. "An experimental and theoretical study of creep of a graphite/epoxy woven composite". *Polymer composites,* ***17***(3), pp. 353–361.

[105] Abd-El Salam, M., 2007. "Stress-strain and creep characteristics of haf black-loaded nbr/epdm rubber blends". *Egyptian Journal of Solids,* ***30***(2).

[106] Ranade, A., Nayak, K., Fairbrother, D., and D'Souza, N., 2005. "Maleated and non-maleated polyethylene-montmorillonite layered silicate blown films: creep, dispersion and crystallinity". *Polymer,* ***46***(18), pp. 7323–7333.

[107] Wang, Y., and Weng, G., 1992. "The influence of inclusion shape on the overall viscoelastic behavior of composites". *Journal of applied mechanics,* ***59***(3), pp. 510–518.

[108] Galwey, A., and Craig, D., 2006. "C thermogravimetric analysis: Basic principles". *Thermal Analysis of Pharmaceuticals*, p. 139.

[109] Hamed, A., Tse, Z., Young, I., Davies, B., and Lampérth, M., 2009. "Applying tactile sensing with piezoelectric materials for minimally invasive surgery

and magnetic-resonance-guided interventions". *Proceedings of the Institution of Mechanical Engineers, Part H: Journal of Engineering in Medicine,* ***223***(1), pp. 99–110.

[110] Hamed, A., Tse, Z., Young, I., and Lamperth, M., 2008. "Mr compatible tactile sensing and noise analysis in a 1.5 tesla mr system". *Medical Imaging and Augmented Reality*, pp. 220–230.

[111] Thiagalingam, A., Davila, A., Foley, L., Guerrero, J., Lambert, H., Leo, G., Ruskin, J., and Reddy, V., 2010. "Importance of catheter contact force during irrigated radiofrequency ablation: Evaluation in a porcine ex vivo model using a force-sensing catheter". *Journal of Cardiovascular Electrophysiology,* ***21***(7), pp. 806–811.

[112] Eick, O., 2003. "Factors influencing lesion formation during radiofrequency catheter ablation". *Indian Pacing and Electrophysiology Journal,* ***3***(3), pp. 117–128.

[113] Bishop, R., 2007. *Mechatronic Systems, Sensors, and Actuators: Fundamentals and Modeling*, 2nd ed. CRC.

[114] Ogden, R., 1984. *Non-linear elastic deformations*. General Publishing Company, Toronto.

[115] Mase, G. T., and Mase, G. E., 1999. *Continuum Mechanics for Engineers, Second Edition*. CRC Press, New York.

[116] Freed, A. D., 1995. "Natural strain". *Journal of Engineering Materials and Technology,* ***117***(4), pp. 379–385.

[117] Mooney, M., 1940. "A theory of large elastic deformation". *Journal of Applied Physics,* ***11***(9), Sep, pp. 582–592.

[118] Belytschko, T., Liu, W., and Moran, B., 2000. *Nonlinear Finite Elements for Continua and Structures*, Vol. 36. Wiley, Chichester.

[119] Prager, W., 2004. *Introduction to Mechanics of Continua*. Dover Pubns, New York.

[120] ANSYS, ed., 2009. *Element Reference*. ANSYS.

[121] Heijnsdijk, E., de Visser, H., Dankelman, J., and Gouma, D., 2004. "Slip and damage properties of jaws of laparoscopic graspers". *Surgical Endoscopy,* ***18***, pp. 974–979.

[122] Rodriguez, E., Nifong, L., Chu, M., Wood, W., Vos, P., and Chitwood, W., 2008. "Robotic mitral valve repair for anterior leaflet and bileaflet prolapse". *The Annals of thoracic surgery,* ***85***(2), pp. 438–444.

[123] Collins, W., 1959. "On the solution of some axisymmetric boundary value problems by means of integral equations, ii: further problems for a circular disc and a spherical cap". *Mathematika,* ***6***(02), pp. 120–133.

[124] Barber, J., 2010. *Elasticity*. Springer-Verlag, New York.

[125] Green, A., and Zerna, W., 1954. *Theoretical Elasticity*. Oxford University Press, Devon.

[126] Vinti, J., Der, G., and Bonavito, N., 1998. *Orbital and Celestial Mechanics*. Aiaa, Danvers.

[127] Sernelius, B., 2001. *Surface Modes in Physics*. Wiley-VCH Verlag GmbH, Berlin.

[128] Gladwell, G., and Gupta, O., 1979. "On the approximate solution of elastic contact problems for a circular annulus". *Journal of Elasticity,* ***9***, pp. 335–348.

[129] Gladwell, G., 1980. *Contact Problems in the Classical Theory of Elasticity*. Springer, Alphen aan den Rijn.

[130] Ottosen, N., and Ristinmaa, M., 2005. *The Mechanics of Constitutive Modeling*. Elsevier, London.

[131] Park, S., and Schapery, R., 1999. "Methods of interconversion between linear viscoelastic material functions. part i–a numerical method based on prony series". *International Journal of Solids and Structures,* ***36***(11), pp. 1653–1675.

[132] Kahn, C., Wang, X., and Rahouadj, R., 2010. "Nonlinear model for viscoelastic behavior of achilles tendon". *ASME Journal of Biomechanical Engineering,* ***132***(11), p. 111002.

[133] Valtorta, D., and Mazza, E., 2005. "Dynamic measurement of soft tissue viscoelastic properties with a torsional resonator device". *Medical Image Analysis,* ***9***(5), pp. 481–490.

[134] Holland, J., 1975. *Adaptation in Natural and Artificial Systems*. The University of Michigan Press, Ann Arbor, Cambridge, MA, USA.

[135] Kohandel, M., Sivaloganathan, S., and Tenti, G., 2008. "Estimation of the quasi-linear viscoelastic parameters using a genetic algorithm". *Mathematical and Computer Modelling,* ***47***(3–4), pp. 266–270.

[136] Christensen, R., 2003. *Theory of Viscoelasticity*. Dover Publications, New York.

[137] Miller, K., and Chinzei, K., 1997. "Constitutive modelling of brain tissue: Experiment and theory". *Journal of Biomechanics,* ***30***(11–12), pp. 1115–1121.

[138] Yuen, S., Vasilyev, N., del Nido, P., and Howe, R. D., 2010. "Robotic tissue tracking for beating heart mitral valve surgery". *Medical Image Analysis*.

[139] Ramezanifard, M., Sokhanvar, S., Dargahi, J., Xie, W., and Packirisamy, M., 2008. "Graphical reproduction of tactile information of embedded lumps for mis applications". *International Symposium on Haptic Interfaces for Virtual Environment and Teleoperator Systems,* ***0***, pp. 247–252.

[140] Sokhanvar, S., Ramezanifard, M., Dargahi, J., and Packirisamy, M., 2007. "Graphical rendering of localized lumps for mis applications". *Journal of Medical Devices,* ***1***(3), pp. 217–224.

[141] Baldewsing, R., de Korte, C., Schaar, J., Mastik, F., and van der Steen, A., 2004. "Finite element modeling and intravascular ultrasound elastography of vulnerable plaques: parameter variation". *Ultrasonics,* ***42***(1–9), pp. 723–729.

[142] Chandran, K., 1992. *Cardiovascular biomechanics*. University Press.

[143] Mehrizi, A., Najarian, S., Moini, M., and Ghomshe, F., 2008. "Tactile distinction of an artery and a tumor in a soft tissue by finite element method". *American Journal of Applied Sciences,* ***5***(2), pp. 83–88.

[144] Samani, A., and Plewes, D., 2007. "An inverse problem solution for measuring the elastic modulus of intact ex vivo breast tissue tumours". *Physics in Medicine and Biology,* ***52***, p. 1247.

[145] Najarian, S., Dargahi, J., and Mehrizi, A., 2009. *Artificial tactile sensing in biomedical engineering*. McGraw-Hill Professional.

[146] de Groot, E., Hovingh, G., Wiegman, A., Duriez, P., Smit, A., Fruchart, J., and Kastelein, J., 2004. "Measurement of arterial wall thickness as a surrogate marker for atherosclerosis". *Circulation,* ***109***(23_suppl_1), pp. III–33.

Appendix A

.1 Lump Localization in One Dimension

To detect and localize inclusions within a soft material, an array of n force sensors is used as shown in Fig. 2a. Initially, to represent the location of the lump graphically, an image with vertical parallel bands corresponding to the sensing elements is considered as shown in Fig. 2b. The intensity of each band is considered to be proportional to the output of the corresponding sensing element.

The voltage distribution along the sensor array can be considered as a vector $\boldsymbol{V}_{1\times n}$ that is related to the intensity vector $\boldsymbol{I}_{1\times n}$ by

$$\begin{cases} I_i = (V_i/\alpha)(K-1), & V_i \leq \alpha \\ I_i = K-1, & V_i > \alpha \end{cases} \quad i = 1, \ldots, n \tag{.1.1}$$

where α is the normalizing factor that determines the working range (very soft, soft, medium, etc.), and K is the number of gray scales that are used in construction of the graphical image (here $K = 256$). It can be seen from eq.(.1.1) that for a given α, when $V_i \leq \alpha$, the scaling factor α maps the input voltage domain into interval $[0, 1]$.

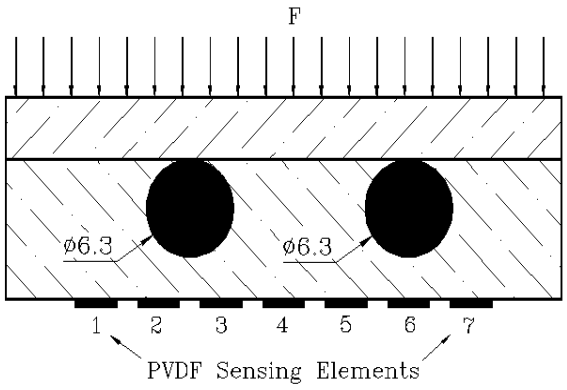

(a)

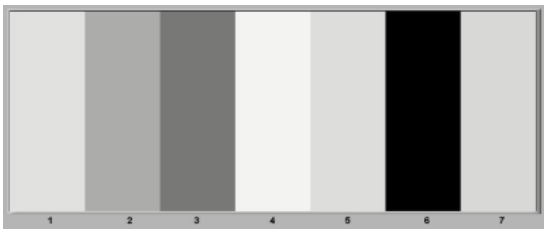

(b)

(c)

Figure 2: Locating the lump in one direction and its graphical rendering

Using the $(K-1)$ factor, this value would then be mapped into the corresponding gray level, between 0 and 255. Once $V_i > \alpha$, all the values of V_i would be mapped to the maximum intensity (i.e, $I_i = 255$). For instance, Fig. 2b shows the graphical display when two lumps are detected in the grasped tissue. However, due to the limited number of sensing elements, the quality of image shown in Fig. 2b was not satisfactory. Therefore, by using an interpolation technique, the quality of the image as shown in Fig. 2c was enhanced. Prior to this, the number of elements had to be increased from n to any desired number N. To do this, $N-n$ extra elements were required. Therefore, $(N-n)/(n-1)$ elements were inserted between each two original elements. The resulting vector $\boldsymbol{G}_{1\times N}$, is in the following form

$$\boldsymbol{G} = \underbrace{\{G_1\, G_2 \ldots G_{N-1}\, G_N\}}_{\text{N elements}} \tag{.1.2}$$

in which

$$G_1 = V_1, \quad G_{\frac{N+n-2}{n-1}} = V_2, \quad G_{\frac{2N+n-3}{n-1}} = V_3, \ldots, \quad G_N = V_n \tag{.1.3}$$

The intensity values assigned to the inserted elements were calculated using the linear interpolation relationship expressed in

$$\begin{aligned} G_i = V_j + \left\{ i - 1 - (j-1)(\frac{N+n-2}{n-1}) \right\} \frac{V_{(j+1)} - V_j}{(N-1)/(n-1)}, \\ 1 + (j-1)\frac{N-1}{n} < i < 1 + j\left(\frac{N-1}{n}\right) \end{aligned} \tag{.1.4}$$

where $j(1 \le j \le n)$ and $i(1 \le i \le N)$ are indices associated with the original vector $\boldsymbol{V}$ and the augmented vector $\boldsymbol{G}$, respectively. The numerical example for $N = 60$, is

illustrated in Fig. 2c.

.2 Lump Localization in Two Dimensions

For localizing nodules in two dimensions, two sensor arrays are required; one array is placed on the top of the object, the other on the bottom. Figure 3a shows how a lump is localized on the horizontal (x-axis) and vertical (y-axis) directions. This figure demonstrates an object that contains a lump, aligned with sensing elements $U2$ and $L2$, where U and L refer to the upper and lower sensing arrays, respectively. The distance of the lump from the upper and lower sensing elements are shown by a and b, respectively. Figure 3b shows the tactile image that was built using a one dimensional algorithm as explained in Appendix Section 1. This graph consists of two rows of color bands, which correspond to the sensor arrays, one on the top and the other at the bottom. Consequently, this graph can be considered as a matrix with 2 rows (color bands) and n (here $n = 7$) columns (sensors), i.e. $2 \times n$ cells. The corresponding matrix, in which each element represents voltage amplitude, can be given in the following form

$$\boldsymbol{V} = \begin{bmatrix} V_{U1} & V_{U2} & \dots & V_{Un} \\ V_{L1} & V_{L2} & \dots & V_{Ln} \end{bmatrix} \tag{.2.1}$$

As can be seen, Fig. 3b cannot clearly provide any relevant information about the location of the lump so, in order to show its precise location, the dimensions

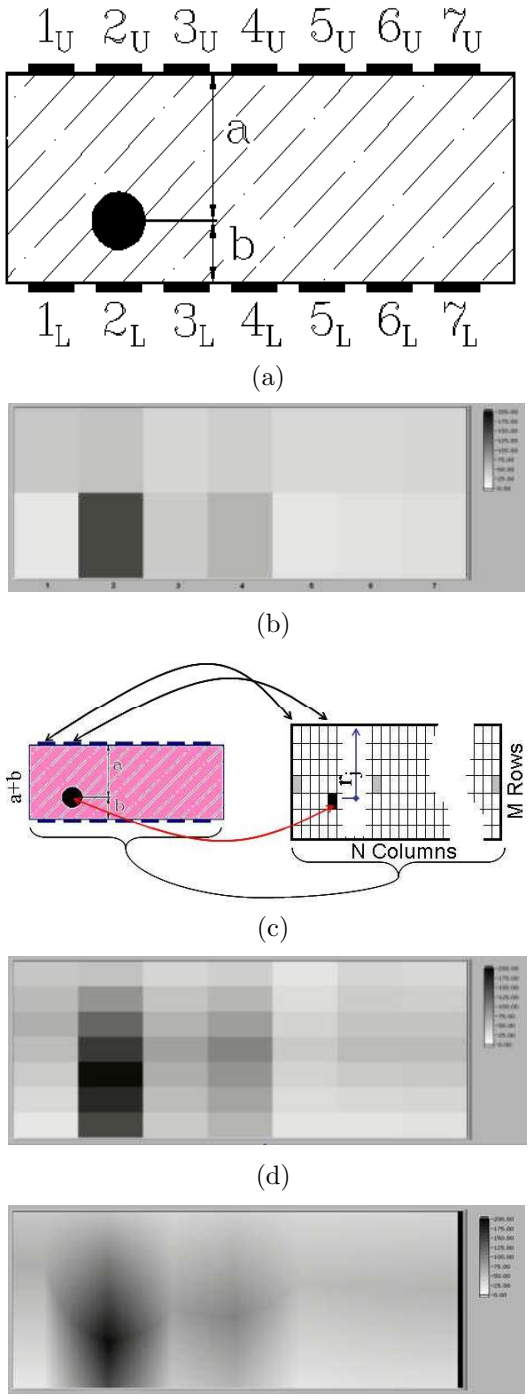

Figure 3: Two-dimensional graphical rendering of the characterized lump (a) A lump located in a soft material with the upper and lower sensor arrays (b) 2D intensity graph associated with the sensor array outputs (c) The relationship between grasped object and intensity matrix (d) A 7×7 matrix showing the location of the lump (e) A 60×100 matrix providing better information on location and size of the lump

of the matrix (and consequently the number of matrix elements) were increased. It should be noted here that the graphical enhancement in the x-direction was explained in Appendix Section 1, so only the row operations (y-direction) are emphasized in this section. To start, and using the technique explained in Section .1, the number of columns was increased to N. Next, the number of rows was increased to M by inserting $(M-2)$ rows of zeros between the first and second rows of matrix $\boldsymbol{V}$ which led to a matrix of size $M \times N$. The resulting matrix $\boldsymbol{G_0}$ can then be shown as

$$\boldsymbol{G_0} = \underbrace{\left\{\begin{matrix} G_{U1} & G_{U2} & \cdots & G_{U(N-1)} & G_{UN} \\ 0 & 0 & \cdots & 0 & 0 \\ \vdots & \vdots & & \vdots & \vdots \\ 0 & 0 & \cdots & 0 & 0 \\ G_{L1} & G_{L2} & \cdots & G_{L(N-1)} & G_{LN} \end{matrix}\right.}_{\text{N Columns}} \text{M Rows} \tag{.2.2}$$

For the graphical representation of a lump, two parameters had to be determined, the location of the centre of lump in each column and its corresponding intensity value. In order to designate the vertical location of the center of lump in each column, a relationship between the thickness of the tissue and the rows of matrix $\boldsymbol{G_0}$ was used. If a lump is located in the tissue at a distance a from the upper sensor array, it will be mapped into row r, where r can be found from relationship:

$$\frac{r}{M} = \frac{a}{a+b} = \frac{G_U}{G_L + G_U} \tag{.2.3}$$

in which $a+b$, that is equal to the tissue thickness, was considered to be proportional

to the number of rows M. Regardless of the existence of a lump, the above equation was applied to all columns (see Fig. 3c). If a lump exists in a column, then a and b are the distances of the center of the lump from the upper and lower sensor arrays, respectively. For the columns with no lump, the associated sensor outputs are equal and $G_L = G_U$, thus $r = M/2$. These cells are shown in Fig. 3c with gray color which can be interpreted as meaning that the algorithm assigns a non-zero value to the middle row of the columns with no lump. Although this value is not significant it can, nonetheless, be considered as a shortcoming of the algorithm. In order to determine the intensity values of these locations in each column, the following relation was used

$$G_{rj} = G_{Uj} + G_{Lj} \tag{.2.4}$$

where index G_{rj} specifies the intensity value of the cell located in row r and column j, showing the center of the lump in that column. The result of this operation is matrix $[\boldsymbol{G_1}]_{n\times m}$, in which the centers of detected lumps are specified

$$\boldsymbol{G_1} = \begin{bmatrix} G_{U1} & G_{U2} & \cdots & G_{UN} \\ 0 & 0 & \cdots & 0 \\ \vdots & \vdots & & \vdots \\ 0 & 0 & \cdots & 0 \\ G_{r_1 1} & G_{r_2 2} & \cdots & G_{r_N N} \\ 0 & 0 & \cdots & 0 \\ \vdots & \vdots & & \vdots \\ 0 & 0 & \cdots & 0 \\ G_{L1} & G_{L2} & \cdots & G_{LN} \end{bmatrix} \tag{.2.5}$$

It should be noted that in the case of multiple lumps, the center of each lump will be mapped to a row that corresponds to the lump's original depth in the tissue so, therefore, different $G_{r_N N}$ members are not necessarily in the same row.

In the next step, a row interpolation procedure was implemented in which, for each column, three values were known: G_{Ui}, G_{ri}, and G_{Li}. Therefore, using these values, and through a linear interpolation, new intensity distribution was assigned to all zeros. The final intensity matrix $\boldsymbol{H}$ can be represented as

$$\boldsymbol{H} = \begin{bmatrix} H_{11} & H_{12} & \cdots & H_{1N} \\ H_{21} & H_{22} & \cdots & H_{2N} \\ \vdots & \vdots & & \vdots \\ H_{(M-1)1} & H_{(M-1)2} & \cdots & H_{(M-1)N} \\ H_{M1} & H_{M2} & \cdots & H_{MN} \end{bmatrix} \tag{.2.6}$$

where the intensity of each cell are calculated from following relationship

$$\begin{cases} H_{ij} = G_{Uj} + (i-1)\frac{G_{r_j j} - G_{Uj}}{r_j - 1}, & 1 \le i \le r_j, \quad 1 \le j \le N \\ H_{ij} = G_{r_j j} + (i-r_j)\frac{G_{Lj} - G_{r_j j}}{M - r_j}, & r_j \le i \le M, \quad 1 \le j \le N \end{cases} \tag{.2.7}$$

Figure 3d shows the position of a lump and its approximate size after implementing the mentioned algorithm when $M = N = 7$. Evidently, increasing the number of cells in both directions will enhance the quality of image. Figure 3e, for instance, is the constructed graphical image based on the same sensor's output and enhancement of associated matrix to $M = 60$ and $N = 100$.